

UNIVERSIDADE ESTADUAL PAULISTA
"JÚLIO DE MESQUITA FILHO"
CAMPUS DE GUARATINGUETÁ

DAN WEN

A hydrodynamical study of particle correlations and collective flow in relativistic heavy ion collisions

Guaratinguetá
2019

DAN WEN

A hydrodynamical study of particle correlations and collective flow in relativistic heavy ion collisions

Tese apresentada à Faculdade de Engenharia do Campus de Guaratinguetá, Universidade Estadual Paulista, como parte dos requisitos para a obtenção do Título de Doutor em FÍSICA na área de DOUTOR EM FÍSICA .

Orientador: Prof. Dr. Wei-Liang Qian

Coorientador: Prof. Dr. Kai Lin

Guaratinguetá

2019

Wen, Dan
W467h A Hydrodynamical study of particle correlations and collective flow in relativistic heavy ion collisions / Dan Wen – Guaratinguetá, 2019
100 f. : il.
Bibliografia: f. 87-94

Tese (doutorado) – Universidade Estadual Paulista, Faculdade de Engenharia de Guaratinguetá, 2019.
Orientador: Prof. Dr. Wei-Liang Qian
Coorientador: Prof. Dr. Kai Lin

1. Hidrodinâmica. 2. Partículas (Física nuclear). 3. Flutuação (Física).
I. Título.

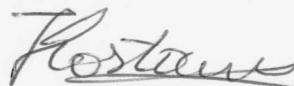
CDU 532.5(043)

DAN WEN

ESTA TESE FOI JULGADA ADEQUADA PARA A OBTENÇÃO DO TÍTULO DE
“DOUTORA EM FÍSICA”

PROGRAMA: FÍSICA

APROVADA EM SUA FORMA FINAL PELO PROGRAMA DE PÓS-GRADUAÇÃO

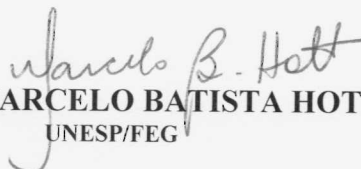


Prof. Dr. Konstatin Georgiev Kostov
Coordenador

BANCA EXAMINADORA:



Prof. Dr. WEILIANG QIAN
Orientador / EEL/USP



Prof. Dr. MARCELO BATISTA HOTT
UNESP/FEG



Prof. Dr. ELIAS LEITE MENDONÇA
UNESP/FEG

participou por video conferência

Prof. Dr. MARCELO GARNEIRO MUNHOZ
USP/Instituto de Física

participou por video conferência

Prof. Dr. ALAN BARROS DE OLIVEIRA
UFOP/MG

Setembro de 2019

DADOS CURRICULARES

DAN WEN

NASCIMENTO 11.01.1988 - Jianyang / Sichuan / China

FILIAÇÃO Xue Wen
YunQing Ma

2007 / 2011 Bachelor of Physics
Department of Physics
China West Normal University

2011 / 2014 Master in Theoretical Physics
Department of Physics
China West Normal University

2015 / 2019 Doctor in Theoretical Physics
Faculdade de Engenharia do Campus de
Guaratinguetá
Universidade Estadual Paulista Júlio de
Mesquita Filho

ACKNOWLEDGMENT

Throughout the writing of this thesis I have received a great deal of support and assistance.

Firstly, I would like to express my heartfelt gratitude to my advisor Prof. Wei-Liang Qian for his continuous supports during my Ph.D study and related research, for his patience, motivation, and immense knowledge. I admire his persistence in quality, his focus on details and his rigorous academic attitude. His spirit of continuous studying has always inspired me. He made me deeply aware of the importance of independent learning. Most of all, during the doctoral study, he let me know that I can do a lot of things that I once thought I couldn't do, which will benefit my whole life.

Besides my advisor, I would like to thank Prof. Yojiro Hama and Prof. Takeshi Kodama for their high-level guidance and insightful comments which incited me to widen my research from various perspectives.

I would like to thank my co-advisor Prof. Kai Lin. Whenever I encounter difficulties, he always gives a helping hand unselfishly. Whenever I am confused, he guides me from a high perspective. Without his guidance, I could not go so far and meet these excellent professors, then I can't broaden my knowledge. He has always been a model for me to learn.

I would like to thank Prof. Konstantin Georgiev Kostov, Prof. Ernesto Vieira Neto, Prof. Julio Marny Hoff da Silva and Prof. Elias Leite Mendonça for their patiently and detailed derivations in the classes which help me so much to study the courses.

I would like to thank the rest of my thesis committee: Prof. Marcelo Batista Hott, Prof. Marcelo Gameiro Munhoz, Prof. Alan Barros de Oliveira, Prof. Saulo Henrique Pereira, Prof. Danuce Marcele Dudek.

My sincere thanks also goes to the server administrators of GridUnesp, and in particular, Angelo Santos, who provided me great help. Without their supports, it would not be possible to finish my work in time.

I would like to thank my classmates and friends for their continued encouragement and help.

I want to express my gratitudes to Brazil for the opportunity to pursue my academic career as a Ph.D. candidate, special thanks go to funding agencies Capes, CNPq, and FAPESP.

Last but not the least, I would like to thank my family for supporting me throughout my studying and residing abroad. Thanks to my mother YunQing Ma and father Xue Wen, who taught me to be

diligent and grateful, to be a righteous person. Thanks to my grandparents KaiHua Shi, HuiZhong Wen, and my sisters, their supports and encouragements have replenished me with more energy to face difficulties. Although I am studying thousands of miles away, their love has never been far away from me, and they have always be my backing.

O presente trabalho foi realizado com apoio da Coordenação de Aperfeiçoamento de Pessoal de Nível Superior- Brasil (CAPES) - código de financiamento 001. processo nº 2018/17746-9, Fundação de Amparo à Pesquisa do Estado de São Paulo (FAPESP). As opiniões, hipóteses e conclusões ou recomendações expressas neste material são de responsabilidade do(s) autor(es) e não necessariamente refletem a visão da FAPESP

This study was financed in part by the Coordenação de Aperfeiçoamento de Pessoal de Nível Superior- Brasil (CAPES) - Finance Code 001. grant #2018/17746-9, São Paulo Research Foundation (FAPESP). The opinions, hypotheses and conclusions or recommendations expressed in this material are the responsibility of the author (s) and do not necessarily reflect the vision of FAPESP.

*“The secret of success is constancy to purpose.”
(Benjamin Disraeli)*

RESUMO

O sucesso da descrição hidrodinâmica das colisões de íons pesados relativísticos desempenha um papel vital para entender as propriedades da matéria QCD. A essência da evolução hidrodinâmica, em geral, foi atribuída à resposta dinâmica às condições iniciais flutuantes. Em particular, as características observadas nas correlações de duas partículas, referidas como “cume” e “ombro”, mostraram ser reproduzidas com sucesso por simulações hidrodinâmicas com condições iniciais flutuantes evento a evento, mas não por condições iniciais médias. Posteriormente, leva ao entendimento atual, através de extensos estudos de análise hidrodinâmica/transporte baseada em eventos por eventos, que as correlações de duas partículas para o momento transversal inferior podem ser interpretadas principalmente em termos de harmônicos de fluxo v_n . Notavelmente, o fluxo triangular, v_3 , é atribuído principalmente à aparência da estrutura do “ombro” no lado externo da partícula acionadora. Além disso, entende-se que esses coeficientes harmônicos estão intimamente associados aos correspondentes ε_n , as anisotropias da distribuição inicial de energia. No entanto, a linearidade entre v_n e ε_n se torna menos evidente para harmônicos maiores que $n = 2$. Isso sugere que as próprias flutuações de evento a evento carregam informações importantes, além da linearidade observada. Se alguém se restringe apenas à análise das relações/correlações médias de eventos entre v_n e ε_n , então alguns sinais hidrodinâmicos genuínos das flutuações locais em cada evento individual podem ser desbotados ou ocultos por trás de algumas correlações muito complicadas entre os harmônicos. Portanto, esperamos explorar de um ângulo alternativo que possa explicar de maneira simples a origem física do padrão de fluxo anisotrópico.

Nesta tese, estudamos as correlações de duas partículas em relação a um modelo de tubo periférico, entre os outros. De nossa perspectiva, as principais características das correlações de duas partículas observadas são atribuídas às flutuações de multiplicidade e à distribuição de uma partícula perturbada localmente. A última é associada à resposta hidrodinâmica às flutuações geométricas nas condições iniciais. Investigamos as propriedades das condições iniciais e do fluxo coletivo em relação ao modelo proposto. É mostrado que os dados experimentais podem ser reproduzidos por simulações hidrodinâmicas usando condições iniciais adequadamente construídas. Além disso, em vez de calibração numérica, extraímos os parâmetros do modelo de acordo com suas respectivas interpretações físicas e mostramos que os valores numéricos obtidos estão de fato qualitativamente de acordo com os dados observados.

Além disso, como a hidrodinâmica é conhecida por suas características altamente não lineares, vários estudos foram realizados para explorar esse aspecto. Em particular, muitos esforços foram dedicados à relação entre excentricidades iniciais do estado e anisotropias do estado final. No contexto da descrição hidrodinâmica evento a evento, analisamos as implicações para dois modelos caracterizados por condições iniciais distintas. A densidade de energia inicial do primeiro modelo adota uma distribuição do tipo Gaussiana, enquanto as do segundo modelo são características de tubos periféricos de alta energia. Calibramos as condições iniciais de ambos os modelos para que suas excentricidades iniciais sejam praticamente idênticas. As distribuições escalonadas de probabilidade do fluxo coletivo e as correlações entre os coeficientes harmônicos e excentricidades do fluxo são investigadas. Além disso, os cálculos são realizados para correlações de partículas em relação aos cumulantes simétricos,

coeficientes de resposta não lineares. Embora as correlações resultantes de duas partículas possuam formas aparentemente semelhantes, os cálculos numéricos indicam uma diferença substancial entre os dois modelos. Para ser específico, a diferença reside em observáveis mais detalhados, como o coeficiente de correlação de Pearson entre harmônicos de ordem superior. Discutimos vários aspectos essenciais relativos à linearidade e não linearidade entre excentricidades iniciais e anisotropias no estado final. Implicações adicionais são abordadas.

PALAVRAS-CHAVE: modelo hidrodinâmico, correlação de partículas, harmônicas de fluxo.

ABSTRACT

The success of the hydrodynamic description of relativistic heavy-ion collisions plays a vital part in our ongoing endeavor to understand the properties of QCD matter. The essence of hydrodynamical evolution, generally, has been attributed to the dynamic response to fluctuating initial conditions. For instance, the observed features in two-particle correlations referred to as “ridge” and “shoulders”, were shown to be successfully reproduced by hydrodynamical simulations with event-by-event fluctuating initial conditions but not by averaged initial conditions. Subsequently, it leads to the current understanding through extensive studies of event-by-event based hydrodynamic/transport analysis. In other words, the two-particle correlations for the lower transverse momenta can be mostly interpreted in terms of flow harmonics v_n . In particular, the triangular flow, v_3 , is mostly attributed to for the appearance of the “shoulder” structure on the away side of the trigger particle. Moreover, it is understood that the flow harmonics are closely associated with the corresponding ε_n , the anisotropies of the initial energy distribution. However, numerical calculations have demonstrated that the linearity between v_n and ε_n become less evident for harmonics higher than $n = 2$. This suggests that the event-by-event fluctuations themselves carry essential information besides the observed linearity. To be specific, if one restricts himself only to the analysis of the event-averaged relations/correlations among v_n and ε_n , then some genuine hydrodynamic signals from the local fluctuations in each individual event might be washed out, or hidden behind some very complicated correlations among the harmonics. Therefore, we hope to explore from an alternative angle, which may explain in a simple way the physical origin of the anisotropic flow pattern.

In this thesis, we study the collective flow, particle correlations, and nonlinear response in terms of, among others, a peripheral tube model. From our perspective, the main characteristics of the observed two-particle correlations are attributed to the multiplicity fluctuations and the locally disturbed one-particle distribution. The latter is associated with the hydrodynamic response to the geometric fluctuations in the initial conditions. Also, we investigate the properties of the initial conditions and collective flow concerning the proposed model. It is shown that the experimental data can be reproduced by hydrodynamical simulations using appropriately constructed initial conditions. Besides, instead of numerical calibration, we extract the model parameters according to their respective physical interpretations and show that the obtained numerical values are indeed qualitatively in agreement with the observed data.

Moreover, as hydrodynamics is known for its high nonlinearity, various studies have been carried out to explore this aspect. In particular, many efforts have been devoted to the relationship between initial state eccentricities and final state anisotropies. In the context of event-by-event hydrodynamic description, we analyze two different models characterized by distinct initial conditions. The initial energy density of the first model adopts a Gaussian-type distribution, while those of the second model are features by high energy peripheral tubes. We calibrate the initial conditions of both models so that their initial eccentricities are mostly identical. The scaled probability distributions of collective flow and the correlations between flow harmonic and eccentricity coefficients are investigated. Besides, the calculations are carried out for particle correlations regarding the symmetric cumulant, nonlinear response coefficients. Although the resultant two-particle correlations possess seemingly

similar shapes, numerical calculations indicate a substantial difference between the two models. To be specific, the difference resides in more detailed observables such as the Pearson correlation coefficient between higher-order harmonics. We discuss several essential aspects concerning the linearity and nonlinearity between initial eccentricities and final state anisotropies. Further implications are addressed.

KEYWORDS: hydrodynamical model, particle correlation, flow harmonics.

LIST OF FIGURES

Fig. 1	High energy nucleus-nucleus collisions (MCLERRAN, 2008).	27
Fig. 2	The space-time evolution of nucleus-nucleus collisions (BJORKEN, 1983). . .	28
Fig. 3	(Color online) The charged particle pseudorapidity distributions for different centrality in $\sqrt{s_{NN}} = 200$ GeV Au+Au collisions, the scatters are PHOBOS data (BACK et al., 2003), and the solid lines are the corresponding SPHERIO simulation results.	34
Fig. 4	(Color online) Charged hadron transverse momentum distributions for different centrality in Au+Au collisions at $\sqrt{s_{NN}} = 200$ GeV, the scatters are PHOBOS data (BACK et al., 2004), and the solid lines are corresponding SPHERIO simulation results.	35
Fig. 5	(Color online) Left: directed flow. Right: elliptic flow. (VOLOSHIN; POSKANZER; SNELLINGS, 2010)	41
Fig. 6	(Color online) Left: the background energy distribution obtained by averaging over many NeXuS events. Right: one random event with a high energy peripheral tube sits on top of the background. The parametrization of the IC is discussed in the text.	54
Fig. 7	(Color online) The temporal evolution of the IC consisting of one peripheral tube placed on top of an elliptic smoothed background energy distribution. The parameters for the IC used in calculation are discussed in section III.	55
Fig. 8	(Color online) The influence of fluctuation of multiplicity on two-particle correlations in one tube model. The results are calculated by using cumulant method. Where the red line is for background Eq.(10) with fluctuation which controlled by a Gaussian function G centered at 0 and standard deviation $\sigma = 0.18$, the green line is for background Eq.(9) without fluctuation. The momentum intervals are $0.4 < p_T^A < 1$ GeV and $2 < p_T^T < 3$ GeV.	56
Fig. 9	(Color online) The di-hadron correlations obtained in SPHERIO simulations, comparing with PHENIX data. Where the red line is calculated by using cumulant method and green line is calculated by using ZYAM method. Left: di-hadron correlations for the momentum intervals $0.4 < p_T^A < 1$ GeV and $2 < p_T^T < 3$ GeV; Right: di-hadron correlations for the momentum intervals $1 < p_T^A < 2$ GeV and $2 < p_T^T < 3$ GeV.	57

Fig. 10	(Color online) The calculated two-particle correlations by using one-tube IC for 20% – 40% centrality window in comparison with the corresponding data by PHENIX Collaboration (ADARE et al., 2008), and those obtained by using the extracted parameters in Table 1 and Eqs.(16) and (17). The SPheRIO results from using cumulant method are shown in red solid curves, the data are shown in solid squares, and those obtained by the estimated parameters are shown by the blue dashed curves. Left: the results for the momentum intervals $0.4 < p_T^A < 1$ GeV and $2 < p_T^T < 3$ GeV. Right: those for the momentum intervals $1 < p_T^A < 2$ GeV and $2 < p_T^T < 3$ GeV.	58
Fig. 11	(Color online) Two-particle correlations for IC with different number of tubes. The results are calculated by using cumulant method in the momentum intervals $0.4 < p_T^A < 1$ GeV and $2 < p_T^T < 3$ GeV.	59
Fig. 12	(Color online) The relative angle distributions calculated by using IC with different number of tubes, where each curve is obtained by using 3000 events. . .	60
Fig. 13	(Color online) The relative angle distributions between Ψ_2 and Ψ_3 in tube model. Left column: the results evaluated by using different numbers of IC with three high energy tubes; Right column: the relative angle distribution (filled black circles) evaluated by the ratio of foreground (red empty circles) to the background (blue empty squares) signals.	62
Fig. 14	(Color online) The relation between model parameters C_n and eccentricity ε_n . Scatters are the results of Eq.(16), determined by a series of random values of C_2, C_3, C_4, C_5 in set 4, and θ_n uniform distributed in $-\frac{\pi}{n} < \theta_n < \frac{\pi}{n}$ for ($n = 2, 3, 4, 5$). Solid lines are the results of Eq.(17).	69
Fig. 15	Left column: the scatter plots of flow harmonics v_n vs. eccentricities ε_n for the peripheral tube model; Middle column: the scatter plots of flow harmonics v_n vs. eccentricities ε_n for the anisotropic Gaussian model with parameter set 1; Right column: the scatter plots of flow harmonics v_n vs. eccentricities ε_n for the anisotropic Gaussian model with parameter set 2.	70
Fig. 16	Left column: the scatter plots of flow harmonics v_n vs. eccentricities ε_n for the anisotropic Gaussian model with parameter set 3; Middle column: the scatter plots of flow harmonics v_n vs. eccentricities ε_n for the anisotropic Gaussian model with parameter set 4; Right column: the scatter plots of flow harmonics v_n vs. eccentricities ε_n for the anisotropic Gaussian model with parameter set 5.	71
Fig. 17	(Color online) A comparison of the calculated di-hadron correlations for $0.4 < p_{associated} < 1$ and $2 < p_{trigger} < 3$ for different IC: the peripheral tube model and the anisotropic Gaussian model with parameter sets 1, 2, 3, 4, 5, comparing with PHENIX data.	72

Fig. 18	(Color online) Left column: the probability density distributions of the EbyE ε_n in anisotropic Gaussian model and peripheral tube model; Right column: the probability density distributions of the EbyE v_n in anisotropic Gaussian model and peripheral tube model	73
Fig. 19	(Color online) The averaged EPOS IC for $\sqrt{s_{NN}} = 2.76$ TeV Pb+Pb collisions at 20% – 25% centrality.	74
Fig. 20	(Color online) The di-hadron correlations for different value of peripheral tube model parameters, and $0.4 < p_{associated} < 1$ and $2 < p_{trigger} < 3$. Left column are results for different maximum energy of tubes at a given radial position, at the top of the right column are results for different radial positions of tubes at a given maximum energy, at the bottom of the right column is the results for $A_{tube} = 30$ and $r_0 = 1.3$ comparing with EPOS+SPheRIO results which has been translated.	75
Fig. 21	(Color online) The calculated temporal evolution of two random events of the peripheral tube model with three tubes (left column) and of anisotropic Gaussian model (right column).	77
Fig. 22	(Color online) The calculated scatter plots of flow harmonics v_n vs. eccentricities ε_n obtained by the peripheral tube model (left column) and anisotropic Gaussian model (right column). In both cases, a total of 2000 events have been used to draw the plot.	78
Fig. 23	(Color online) Left: the probability density distribution of the event-by-event ε_n in the peripheral tube model and anisotropic Gaussian model; Right: The probability density distributions of the resultant flow harmonics v_n in the two models.	80
Fig. 24	p_T dependence of v_3 in anisotropic Gaussian model and peripheral tube model.	81
Fig. 25	(Color online) The normalized probability density distribution of the event-by-event ε_n and v_n in the peripheral tube model (left column) and anisotropic Gaussian model (right column).	82
Fig. 26	(Color online) A comparison of the di-hadron correlations for $0.4 < p_{associated} < 1$ and $2 < p_{trigger} < 3$ for anisotropic Gaussian model and peripheral tube model.	83

LIST OF TABLES

Table 1 – The calculated background as well as overall elliptic flow coefficients for corresponding transverse momentum intervals of trigger and associated particles. The calculations are carried out by using IC as described in the text.	56
Table 2 – The model parameters of the peripheral tube model in the present study	76
Table 3 – The model parameters of the anisotropic Gaussian model in the present study . . .	76
Table 4 – The calculated average v_n for 2.76 TeV Pb+Pb collisions at 20% – 25% centrality .	79
Table 5 – The calculated nonlinear response coefficients for 2.76 TeV Pb+Pb collisions for the 20%-25% centrality class.	84
Table 6 – The calculated symmetric cumulants for 2.76 TeV Pb+Pb collisions in 20% – 25% centrality class.	84
Table 7 – The mixed harmonics for 2.76 TeV Pb+Pb collisions in 20% – 25% centrality class.	84
Table 8 – The PHENIX data (AFANASIEV et al., 2009), $v_2\{2\}$ as a function of p_T in centrality 20% – 60%.	99

CONTENTS

1	INTRODUCTION	19
2	RELATIVISTIC HEAVY ION COLLISIONS	23
2.1	Kinematic variables	23
2.1.1	Four coordinates, four velocity and four momentum	23
2.1.2	Rapidity and pseudorapidity	25
2.2	Hydrodynamical model of nucleus-nucleus collisions	26
2.2.1	High energy nucleus-nucleus collisions	27
2.2.2	The application of hydrodynamic model	28
2.2.2.1	Smoothed particle hydrodynamics	30
2.2.2.2	SPheRIO code	33
3	COLLECTIVE FLOW	37
3.1	Eccentricity	39
3.2	Flow harmonics	40
3.3	Event plane method	41
3.4	Nonlinear hydrodynamic response	43
3.5	two-particle correlations	46
4	ON THE PERIPHERAL TUBE DESCRIPTION OF THE TWO-PARTICLE CORRELATIONS IN NUCLEAR COLLISIONS	49
4.1	The analytical peripheral tube model for two-particle correlations	50
4.2	Parameters and hydrodynamic simulation results of one-tube model	53
4.3	Parameters extracted from simulation results	57
4.4	Discussion on multi-tube model	58
5	ANISOTROPIC GAUSSIAN MODEL AND PERIPHERAL TUBE MODEL	63
5.1	Brief description of models	64
5.1.1	Peripheral tube model	64
5.1.2	Anisotropic Gaussian model	65
5.2	Simulations for 2.76 Tev Pb+Pb collisions at 20% – 25% centrality by using Peripheral Tube Model and Anisotropic Gaussian model	74
5.2.1	Parameterization of models	74
5.2.2	Numerical results	76
6	CONCLUSION	85
	BIBLIOGRAPHY	87

APPENDIX A – BOXMULLER METHOD	95
APPENDIX B – SIMPSON’S RULE	97
APPENDIX C – THE PHENIX DATA	99

1 INTRODUCTION

According to the Standard Model of particle physics (MARTIN; SHAW, 2017), quarks and gluons are the elementary degrees of freedom of the strong interaction. Quarks carry color charge and interact with each other via the exchange of gluons. The gluons are massless particles whose properties are determined by the local gauge symmetry. Because of the color confinement, color charged particles such as quarks and gluons cannot exist as free particles. Instead, they are strongly bound to one another, forming color-neutral composite particles, known as hadrons. From Quantum Chromodynamics (QCD), the fundamental theory of the strong interaction, the asymptotic freedom can be derived. The latter indicates that interaction between particles becomes weaker at shorter distances. That is to say, with increasing temperature or increasing baryon density, a phase transition shall occur so that ordinary hadrons become deconfined.

Subsequently, the quarks and gluons become the proper degrees of freedom, and their motions are no longer confined to the bound states, the hadrons. In this context, relativistic heavy-ion collisions become the most promising approach to compress and heat up the nuclear matter in the laboratory. The relevant experiments create the environment with extreme conditions, where the properties of the so-called quark-gluon plasma can be investigated.

The hydrodynamic description (HAMA; KODAMA; SOCOLOWSKI JR., 2005) of high energy nuclear collisions can be briefly summarized as follows. As two Lorentz contracted nuclei collide, a large amount of energy is deposited into a small region of space for an exceptionally short duration of time. Subsequently, a hot and dense matter is formed in such extreme conditions (CHEUK-YIN, 1994). The latter is assumed to be in local thermal equilibrium with immensely high temperature and energy density, which follow by a hydrodynamic expansion. The temporal evolution is essentially dictated by the conservation equations of energy-momentum and relevant conserved charges. As the expansion proceeds, the temperature and density gradually decrease until the hadronization occurs. Afterward, the characteristics of the system become more of a collection of free particles rather than a fluid.

SPheRIO, *a.k.a.* Smoothed Particle hydrodynamic evolution of Relativistic heavy IOn collisions, is a numerical implementation to simulate the hydrodynamic evolution (HAMA; KODAMA; JR., 2005). The code is based on the Smoothed Particle Hydrodynamic (SPH) algorithm (Monaghan, 1992; AGUIAR et al., 2001; MOTA; CHEN; QIAN, 2017). The method parametrizes the continuous density distribution of an extensive physical quantity in terms of the sum of base functions with finite support. At the beginning of the hydrodynamic evolution, one requires the initial conditions (IC). The IC consist of detailed space distributions of the energy-momentum tensor, baryon-number, strangeness, and charge densities, at a given initial time $\tau \sim 1fm$ (HAMA; KODAMA; SOCOLOWSKI JR., 2005). By combining the equation of state, the SPheRIO code can be used to solve the hydrodynamic equations. By the end of system evolution, the decoupling prescriptions will specify where and when the freeze-out happens where the hadron emission takes place. The final state hadrons can be observed in the experiment. Thus one can compare the simulation results with

experimental ones.

It is widely recognized that the hydrodynamic approach provides a good description of heavy-ion collisions (KOLB; HEINZ, 2003; HUOVINEN, 2003; HIRANO; TSUDA, 2002; CASTILHO et al., 2017; CASTILHO et al., 2018). It gives many satisfactory results, such as the reproduction of the rapidity and transverse momentum spectra, particle correlations, and collective flow. In particular, the collective flow was first observed in RHIC experiments, where the outgoing particles exhibit an almond-shaped distribution. Such collective phenomena (VOLOSHIN; POSKANZER; SNELLINGS, 2010; MCDONALD et al., 2017; NACHMAN; MANGANO, 2018) are regarded as an essential signal of the formation of quark-gluon plasma (QGP). As a matter of fact, the hydrodynamic calculations were shown to be consistent with the experimental measurements of collectivity in terms of the final state hadron distributions. Such observations confirmed the speculation that the evolution of the collision system is mostly dominated by collective motion, while thermalization is attained to a high degree. Therefore, the momentum distribution of nuclear matter produced in non-central collisions is elliptic mainly, as the interactions between the constituents transform the initial geometrical fluctuations in real space into anisotropy of final hadrons in momentum space. This has been interpreted as the hydrodynamic response of the collisional system to the initial anisotropic geometry.

The anisotropic flow can be systematically quantified by using the Fourier expansion coefficients of the particle azimuthal distribution (VOLOSHIN; ZHANG, 1996), where the second coefficient v_2 is referred to as elliptic flow. The expansion coefficients v_n can be calculated by using the event plane method, or particle correlations, among others. For the event plane method, an approximation is introduced since the reaction plane cannot be directly measured in experiments. Therefore, it is estimated by using the azimuthal angles of the outgoing particles (POSKANZER; VOLOSHIN, 1998; JIA; COLLABORATION, 2013). Furthermore, people have developed the two-particle correlation method (WANG et al., 1991; TRZUPEK, 2011; COLLABORATION), 2016) to study anisotropic flow, which does not explicitly depend on the reaction plane. However, an inevitable problem for the two-particle correlation is that in addition to the flow correlation, there is a non-negligible contribution from the non-flow correlation (DINH; BORGHINI; OLLITRAULT, 2000; BORGHINI; OLLITRAULT; DINH, 2000). The non-flow correlation may be caused by (DANIELEWICZ et al., 1988; ADLER et al., 2002) resonance decays, (mini)jets, strings, quantum statistics effects, final state interactions such as Coulomb effects, momentum conservation, etc. Therefore, an accurate flow analysis needs to take into account the effects of non-flow, and different methods have been developed to eliminate the non-flow correlations (ACKERMANN et al., 2001; POSKANZER; VOLOSHIN, 1998; DANIELEWICZ et al., 1988; DINH; BORGHINI; OLLITRAULT, 2000; BORGHINI; OLLITRAULT; DINH, 2000; AGGARWAL et al., 1997; RANIWALA; RANIWALA; VIYOGI, 2000). One of the most effective methods is regarding cumulant expansions of multi-particle associations (BORGHINI; DINH; OLLITRAULT, 2001). This method is shown to be more efficient to eliminate the effect of non-flow at a higher order, and the interference of the detector can also be taken into account appropriately. Besides, some other methods have also been proposed, such as Lee-Yang zeroes method (BHALERAO; BORGHINI; OLLITRAULT, 2003), Q-cumulant (BILANDZIC; SNELLINGS; VOLOSHIN, 2011), among others (BILANDZIC et al., 2014), etc. All these different methods enriched and deepened our

understanding concerning collective flow from different aspects.

Differential elliptic flow is a topic which has been studied extensively for Au-Au collisions at RHIC (BACK et al., 2002; BACK et al., 2005a; BACK et al., 2005b; ADAMS et al., 2005a; ADCOX et al., 2005). These studies involve the pseudorapidity, centrality, transverse momentum, and energy dependence of elliptic flow v_2 . Theoretically speaking, elliptic flow is considered to be a response to the almond shape of the overlap region in non-central collisions, which should not be significant in central collisions. However, a sizable elliptic flow was observed in most central Cu-Cu collision (ALVER et al., 2007), which is, in turn, interpreted as caused by the fluctuations of the initial geometry. Actually, the event-by-event fluctuations of IC was first pointed out by Kodama et al (AGUIAR et al., 2002; JR. et al., 2004; ANDRADE et al., 2006). Subsequently, much attention is paid to the importance of the fluctuations in the initial conditions (TAKAHASHI et al., 2009). More recently, it was pointed out that such fluctuations are also the reason for the generation of triangular flow v_3 (ALVER; ROLAND, 2010) and other higher harmonics. Therefore, hydrodynamic with event-by-event fluctuating initial conditions is essential for the exact determination of collective flow observables and study higher flow harmonics. The higher order flow harmonics have been measured at RHIC (ADARE et al., 2011; SORENSEN, 2011) and LHC (AAMODT et al., 2011; AAMODT et al., 2012). In particular, the event-by-event distributions of flow harmonics also can be analyzed by the experimental collaborations (JIA, 2013; MOHAPATRA, 2013; AAD et al., 2013). Subsequent hydrodynamic simulations demonstrate that event-by-event hydrodynamics also works reasonably well in this case. The model not only describes the average of flow harmonics but also the event-by-event distribution of flow harmonics (GALE et al., 2013a), as well as event-plane correlations (BHALERAO; OLLI-TRAUULT; PAL, 2013; TEANEY; YAN, 2014). What is more, the observed structures of two-particle correlations, referred to as “ridge” and “shoulders”, were also successfully reproduced by hydrodynamical simulations with event-by-event fluctuating IC but not by averaged IC (TAKAHASHI et al., 2009). The event-by-event fluctuating initial conditions are now widely employed as a standard in hydrodynamic simulations of heavy-ion collisions.

Concerning the mapping between initial state geometry and final state flow, many efforts have been devoted. The participant eccentricity $\varepsilon_{\text{part}}$ was investigated regarding the initial geometry in Ref.(ALVER et al., 2007), and it points out that $\varepsilon_{\text{part}}$ is responsible for elliptic flow. After “ridge” and “shoulder” are observed, the study of IC decomposition is extended to the third-order Fourier coefficient (ALVER; ROLAND, 2010). Lately, Teaney and Yan introduced a cumulant expansion to parameterize IC in relativistic heavy-ion collisions (TEANEY; YAN, 2011). Moreover, it can be shown (GALE; JEON; SCHENKE, 2013) that the distributions of initial eccentricities provide already an excellent approximation of the measured v_n distributions when scaled by their mean value. The linear nature for second order coefficient and nonlinear nature for higher order coefficients have been studied in (NIEMI et al., 2012; TEANEY; YAN, 2012; GALE et al., 2013a; FU, 2015; QIAN et al., 2014). Additionally, the patterns of the fluctuations of the initial geometry and nonlinear effects in the final state have been studied by measurements of event-plane correlations in ATLAS experiment at the LHC (AAD et al., 2014).

In general, the hydrodynamic model with event-by-event fluctuating initial conditions has been

very successful in describing heavy-ion collisions at RHIC and LHC. It successfully reproduced the particle spectra, anisotropic flow, particle correlations, correlations of event planes and the distributions of flow harmonics, etc. However, there are still unknown issues, and uncertainties remain, such as the physics behind the observed structures of two-particle correlation and the mapping between initial geometry and final flow harmonics.

Even though the distinctive features of two-particle correlations have been reproduced in the hydrodynamic approach, how the structures are generated is still not thoroughly understood. In this context, the peripheral tube model (ANDRADE et al., 2010b; QIAN et al., 2013) is proposed to investigate the origin of these structures in the two-particle correlations. The model views the fluctuations in the IC as consisting of independent high energy tubes close to the surface of the system. These fluctuations sit on top of the background, elliptical energy density distribution, which is smooth and obtained from averaging many different events. This simple model is intuitive and transparent regarding its physical content. Subsequently, one might devise the desired IC, and employ a hydrodynamic code to investigate whether the outcome capture the essence of the existing experimental data (ANDRADE et al., 2010a; HAMA et al., 2009; ANDRADE et al., 2011a; HAMA et al., 2010; CASTILHO et al., 2017; CASTILHO et al., 2018). This thesis is dedicated to a hydrodynamical study of particle correlations and collective flow, primarily based on the peripheral tube model. We study the analytic results of two-particle correlations and nonlinear hydrodynamic response to the initial geometry in this work, which is different from previous investigations of this model.

The present thesis is organized as follows. Chapter 2 gives an overview of heavy-ion collisions. We first review the definitions of some useful kinematic variables. Then, a brief description of nucleus-nucleus collisions in terms of the hydrodynamical model is given. Subsequently, we examine the implementations of the hydrodynamic model, inclusively the Smoothed Particle Hydrodynamics. The SPheRIO code is presented and discussed. Chapter 3 is dedicated to topics such as collective flow, eccentricity, and particle correlations. The associated analysis methods are also discussed. Chapter 4 presents the results on the peripheral tube description of the two-particle correlations in nuclear collisions. Chapter 5 presents the results on the study of nonlinearity in terms of an anisotropic Gaussian model and peripheral tube model. Chapter 6 gives the concluding remarks.

2 RELATIVISTIC HEAVY ION COLLISIONS

In modern particle physics (MARTIN; SHAW, 2017), the Standard Model is considered as the theory to describe the three out of four known of fundamental interactions. Accordingly, the basic constituents of matter are the quarks, leptons, together with photons, gluons, W and Z bosons, and Higgs boson plays the roles as the “force carriers” which mediate the interactions between them. Although most of the particles that we can directly observe are hadrons in the quark bound states, it is understood that the free quarks and gluons can exist in specific extreme environments, known as QGP. For instance, the Big Bang theory (SINGH; BANG, 2005; WEINBERG, 1977) predicts that in a fraction of a second after the beginning, the Universe was primarily made up of free quarks and gluons. Relativistic Heavy-Ion Collisions, on the other hand, have been proposed to produce such a state of matter and among others, aimed to explore the properties of QCD matter. The Relativistic Heavy Ion Collider (RHIC) and the Large Hadron Collider (LHC) were established for the creation of such extreme conditions in the laboratory which mimics the beginning of the Universe. To be specific, at particle accelerators such as RHIC and LHC, two high-energy particle beams traveling in opposite directions are accelerated to nearly the speed of light before the collision takes place. When ionized particles collide at such high speeds, extremely high temperature and high-density environment is created, where the QGP is formed. As the collision area cools off, thousands of particles are formed. The measurements of these final state particles provide valuable clues about what is happening within the collision zone, inclusively the thermal properties of the QGP. The endeavor of the experimentalists associated with RHIC and LHC pave the way for our deepened understanding of the fundamental building block of our Universe.

In order to theoretically analyze the relativistic heavy-ion collisions, one needs to choose some convenient variables. In this chapter, we will first review the kinematic variables frequently used in literature, then briefly describe the processes taken place at RHIC and LHC. Also, the hydrodynamic model for relativistic heavy-ion collisions as well as its numerical algorithm is presented and discussed.

2.1 KINEMATIC VARIABLES

In the relativistic heavy ion collisions, ions collide with each other at relativistic speeds, and special relativity deals with such high speed movement. Therefore, it is necessary to learn about how to describe a movement in relativistic mechanics. And then, the variables frequently used in relativistic heavy ion collisions are introduced in terms of the basic variables in special relativity.

2.1.1 Four coordinates, four velocity and four momentum

In special relativity (HOBSON; EFSTATHIOU; LASENBY, 2006), “time” and “space” are no longer absolute as in classical dynamics, but is considered as relative four-dimensional space-time. Thus, the position of an event in space-time is labeled by four coordinates (ct, x, y, x) , which can be

denoted by a contravariant vector as follow

$$x^\mu = (x^0, x^1, x^2, x^3) = (t, x, y, z), \quad (1)$$

here we use the natural units $c = \hbar = 1$. The covariant vector is

$$x_\mu = (x_0, x_1, x_2, x_3) = g_{\mu\nu}x^\mu = (t, -x, -y, -z), \quad (2)$$

where $g_{\mu\nu}$ is the space-time metric tensor with the following form

$$g_{\mu\nu} = \begin{pmatrix} 1 & 0 & 0 & 0 \\ 0 & -1 & 0 & 0 \\ 0 & 0 & -1 & 0 \\ 0 & 0 & 0 & -1 \end{pmatrix}. \quad (3)$$

We may choose different reference frames to describe an event, so the same event may have different four coordinates in different reference frames. But it does not matter, principle of relativity states that the laws of physics take the same form in all reference frames. To understand the relation of coordinates in different reference frames, we assume a particle has coordinates (t, x, y, z) in cartesian inertial frame S , and (t', x', y', z') in cartesian inertial frame S' . This two different reference frames S and S' is moving away from each other with velocity v in the x -direction. On the basis of the constancy of the velocity of light and principle of relativity, we can derive the Lorentz transformation

$$\begin{aligned} t' &= \gamma(t - \beta x), \\ x' &= \gamma(x - \beta t), \\ y' &= y, \\ z' &= z, \end{aligned} \quad (4)$$

where $\beta = v/c = v$ and $\gamma = (1 - \beta^2)^{-1/2}$.

According to the definition of the four-velocity

$$u^\mu = \frac{dx^\mu}{d\tau} = (c, u^x, u^y, u^z), \quad (5)$$

we can derive the corresponding Lorentz transformations

$$\begin{aligned} u^{x'} &= \frac{u^x - v}{1 - u^x v}, \\ u^{y'} &= \frac{u^y}{\gamma(1 - u^x v)}, \\ u^{z'} &= \frac{u^z}{\gamma(1 - u^x v)}, \end{aligned} \quad (6)$$

The four-momentum is defined in terms of four-velocity

$$p^\mu = m u^\mu = (E, p^x, p^y, p^z), \quad (7)$$

and the Lorentz transformations are

$$\begin{aligned}
 p^{x'} &= \gamma(p^x - \beta E), \\
 p^{y'} &= p^y, \\
 p^{z'} &= p^z, \\
 E' &= \gamma(E - \beta p^x),
 \end{aligned} \tag{8}$$

These kinematic variables and the Lorentz transformations are widely used in special relativity, but we hope to use some convenient variables which have simple properties under a Lorentz transformation in high-energy reaction processes.

2.1.2 Rapidity and pseudorapidity

In high energy nucleus-nucleus collisions, we choose longitudinal direction as the spatial z -axis which is equal to the direction of the beam particle, and the transverse plane orthogonal to the longitudinal direction. A useful rapidity variable y is induced to describe the longitudinal movement (CHEUK-YIN, 1994), it is defined by using the components of the four-momentum,

$$y = \frac{1}{2} \ln\left(\frac{p_0 + p_z}{p_0 - p_z}\right). \tag{9}$$

The advantage of using rapidity is that it has a simple Lorentz transformation. For example, the rapidity of a particle in a laboratory frame F is y , and in a boosted Lorentz frame F' is y' . Frame F' moves away from F with a velocity β in the z -direction. According to the definition of rapidity Eq.(9) and the Lorentz transformation of four-momentum Eq.(8), we can obtain

$$\begin{aligned}
 y' &= \frac{1}{2} \ln\left(\frac{p'_0 + p'_z}{p'_0 - p'_z}\right) \\
 &= \frac{1}{2} \ln\left(\frac{\gamma(1 - \beta)(p_0 + p_z)}{\gamma(1 + \beta)(p_0 - p_z)}\right) \\
 &= y + \frac{1}{2} \ln\left(\frac{1 - \beta}{1 + \beta}\right) \\
 &= y - \frac{1}{2} \ln\left(\frac{1 + \beta}{1 - \beta}\right),
 \end{aligned} \tag{10}$$

we find that the Lorentz transformation of the rapidity of the particle in this two frame is to add a constant.

The four-velocity is normalized $u^\mu u_\mu = 1$, then the square of four-momentum $p^\mu p_\mu = p_0^2 - p_x^2 - p_y^2 - p_z^2 = m^2$. By defining the transverse mass of the particle

$$m_T^2 = m^2 + p_T^2 = p_0^2 - p_z^2, \tag{11}$$

where m is the rest mass of the particle and transverse momentum $p_T^2 = p_x^2 + p_y^2$. It is easy to express

the energy p_0 and longitudinal momentum p_z of particle in terms of rapidity

$$p_0 = m_T \cosh(y), \quad (12)$$

$$p_z = m_T \sinh(y). \quad (13)$$

Therefore, as long as we measure the energy and longitudinal momentum, we can obtain the rapidity of a particle.

Rapidity variable has its advantage of simple Lorentz transformation, hence it is convenient to describe the dynamics of relativistic particles. However, in many experiments, what we can directly measure is the angle θ of the detected particle relative to the beam axis.

$$\theta = \arccos\left(\frac{p_z}{|\mathbf{p}|}\right), \quad (14)$$

where $|\mathbf{p}| = \sqrt{p_x^2 + p_y^2 + p_z^2} = \sqrt{p_T^2 + p_z^2}$ is the 3-momentum of particle. Considering the realistic measurements, it will be convenient to introduce the pseudorapidity variable which is defined in terms of θ

$$\begin{aligned} \eta &= -\ln[\tan(\theta/2)] \\ &= \frac{1}{2} \ln\left(\frac{|\mathbf{p}| + p_z}{|\mathbf{p}| - p_z}\right). \end{aligned} \quad (15)$$

Then we can use pseudorapidity to express the momentum

$$|\mathbf{p}| = p_T \cosh(\eta), \quad (16)$$

$$p_z = p_T \sinh(\eta). \quad (17)$$

When the momentum is large enough to ignore the mass of the particle, then $|\mathbf{p}| \approx p_0$, we find the pseudorapidity variable Eq.(15) approximately equal to rapidity variable Eq.(9). In experiments, we can integrate out the pseudorapidity distribution $dN/d\eta$ of particles from the measurements.

2.2 HYDRODYNAMICAL MODEL OF NUCLEUS-NUCLEUS COLLISIONS

As an emerging field, the high energy nucleus-nucleus collisions physics has developed into an interdisciplinary related to nuclear physics, particle physics, statistical physics, relativistic fluid dynamics and astrophysics. It aims to create a extremely high-temperature and high-density environment like the early stage of Big Bang where the quark-gluon plasma may be produced (CHEUK-YIN, 1994), then we can explore the deconfinement QGP and its properties. However, due to the confinement of quarks, the existence of QGP is a very short duration of time, it is impossible to observe QGP directly. Therefore, some models are employed to solve this trouble. In our work, we adopt the hydrodynamic model. In this section, we will review the evolution of high energy nucleus-nucleus collisions and the application of hydrodynamic model.

2.2.1 High energy nucleus-nucleus collisions

Fig. 1 is a simple schematic diagram for the collision of two nuclei in the center-of-mass system (MCLERRAN, 2008). At first, two nuclei collide with a velocity close to the speed of light, due to the Lorentz contraction, they look like two thin disks. Once the collisions take place, the colliding nucleons will lose large amount of their energies in the inelastic processes. If the energy of each nucleon in the center-of-mass system is high enough, the baryons can still have enough momentum to move away from the region of collision after collision. Then the energy lost by the colliding baryons is deposited in a small collision region of space, this high energy density environment leads to a new matter formation, which is considered to be QGP.

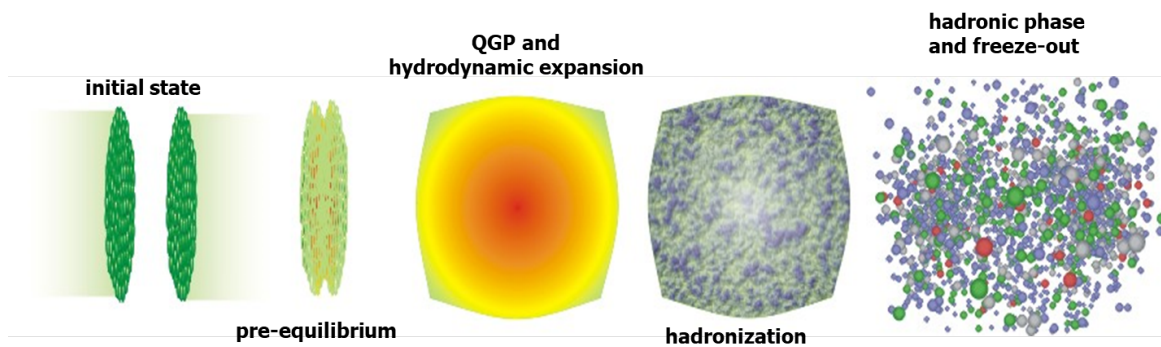


Fig. 1 – High energy nucleus-nucleus collisions (MCLERRAN, 2008).

According to Bjorken's suggestion (BJORKEN, 1983) of the space-time evolution of a nucleus-nucleus collision, the QGP will be in local equilibrium very soon after its formation, then it will undergo a hydrodynamic evolution, as show in Fig. 2.

As the system expands, the temperature decreases to a critical value, which will lead the quark to be confined into the hadron again. Then the system continues to expand because of the interactions between produced hadrons. With the temperature dropping to chemical freeze-out temperature, the inelastic collisions stop, the species of particle no longer change. Subsequently, when the temperature drops to thermal freeze-out temperature, the elastic collisions stop, the multiplicity and spectrum is determined. At last, the particles stop to interact with each other as the fluid becomes cooler and cooler and more rarefied, hadron emission takes place. What we observe in the final state are free particles.

Many interesting phenomena of the final state particles observed in the experiment provide strong evidence for the existence of QGP. For example, the enhancement of strange particle yields is supposed to should occur in the QGP phase (KOCH; MÜLLER; RAFELSKI, 1986) is observed in RHIC experiment (ABELEV et al., 2007; CHEN et al., 2008; AGAKISHIEV et al., 2012), as well as the J/Ψ suppression (MATSUI; SATZ, 1986; KAKADE; PATRA; THAKUR, 2014), Jet quenching (WANG; GYULASSY, 1992; ADAMS et al., 2003), photons and dileptons (ALAM; RAHA; SINHA, 1996) are also considered to be the important signals of QGP.

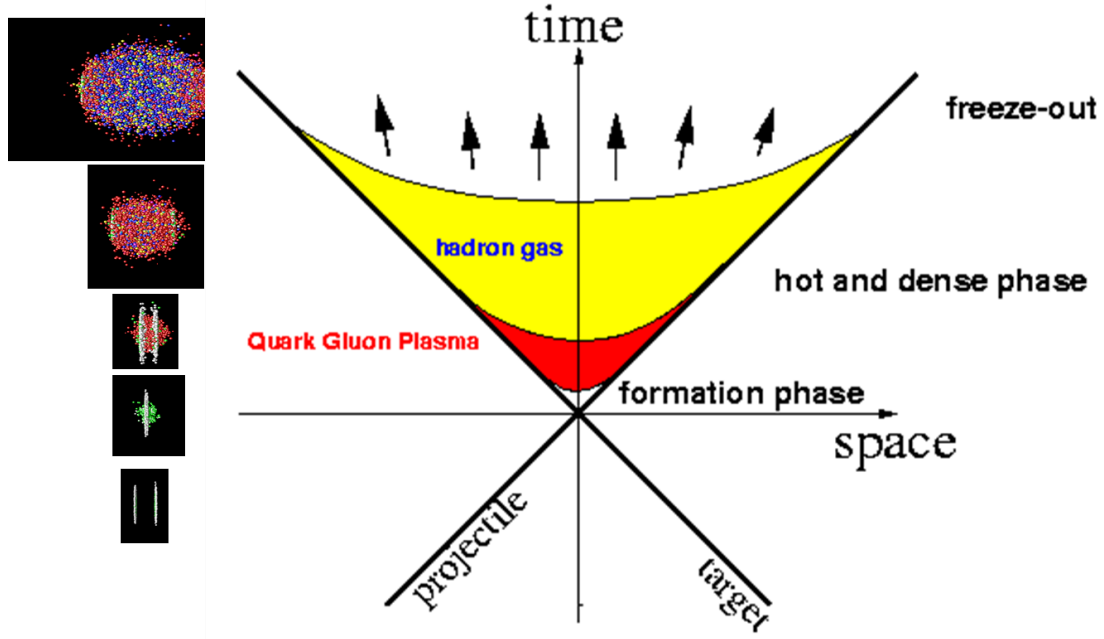


Fig. 2 – The space-time evolution of nucleus-nucleus collisions (BJORKEN, 1983).

2.2.2 The application of hydrodynamic model

Since the evolution of QGP finishes in a very short duration of time, we could hardly observe it directly in experiments, so we employ hydrodynamic model to analyze its properties. As mentioned above, the prerequisite for using the hydrodynamic model is that the QGP reaches the local thermal equilibrium, in which the state can be characterized by initial conditions in terms of distribution of four-velocity and thermodynamical quantities. In addition, the relations between thermodynamical quantities are called equations of state (EOS) which is determined by the properties of QGP. With the initial conditions and equations of state, the QGP follows a hydrodynamical expansion which is controlled by $(4 + i)$ conservation equations,

$$\partial_{\mu} T^{\mu\nu} = 0, \quad (18)$$

$$\partial_{\mu} n_i^{\mu} = 0, \quad (19)$$

where n_i^{μ} are conserved charges like baryon, strangeness and so on. The energy-momentum is

$$T^{\mu\nu} = (\epsilon + p)u^{\mu}u^{\nu} - pg^{\mu\nu}, \quad (20)$$

where ϵ is the energy density, p is the pressure, u^{μ} is the four-velocity of the fluid.

The main task in hydrodynamic model is to solve these partial differential equations. Moreover, because of their highly nonlinear properties, it is really very hard to find an exact analytic resolution. There are some famous analytical solutions, such as Khalatnikov's one-dimensional analytical solution to Landau's initial conditions (KHALATNIKOV, 1954), the boost-invariant solution which is used to estimate the initial energy densities in ultrarelativistic nucleus-nucleus collisions (HWA, 1974; CHIU; WANG, 1975; CHIU; SUDARSHAN; WANG, 1975), and a more general one-dimensional

scale invariant solution proposed by T. Csörgő et al (CSÖRGŐ et al., 2003; CSÖRGŐ et al., 2004), which includes a class of transverse flows.

However, these simple analytical solutions obtained in some ideal conditions (like a symmetric or one-dimensional configuration) have their limitation in realistic situations. Therefore, we turn to a numerical method which can deal with any kind of geometry, even if the solution is not so precise. Because what we want to observe is the general flow behavior which characterizes the dynamics of the system at a given equation of state, initial conditions and the decoupling procedure. To solve the hydrodynamical equations of motion, it is better to start from the variational formulation.

Firstly, we review the derivation of the equation of motion from the Lagrangian in the condition of constraint. According to Ref.(HAMA; KODAMA; SOCOLOWSKI JR., 2005), the dynamics of relativistic fluid is described by action

$$I = \int d^4x \{-\epsilon\}, \quad (21)$$

where $\epsilon = \epsilon(n, s)$ is the proper energy density, n, s are the proper baryon density and entropy density respectively. Considering constraints, that are the conservation laws and normalization of four-velocity

$$\begin{aligned} \partial_\mu(nu^\mu) &= 0, \\ \partial_\mu(su^\mu) &= 0, \\ u^\mu u_\mu &= 1. \end{aligned} \quad (22)$$

We can write variational formulation with Lagrangian multipliers

$$\delta \int d^4x [-\epsilon + \lambda \partial_\mu(nu^\mu) + \xi \partial_\mu(su^\mu) - \frac{1}{2}w(u^\mu u_\mu - 1)] = 0, \quad (23)$$

where λ, ξ and w are Lagrangian multipliers and arbitrary functions of x . The effective Lagrangian can be obtained from Eq.(23)

$$\mathcal{L}_{eff}(n, s, u^\mu, \lambda, \xi, w) = -\epsilon - nu^\mu \partial_\mu \lambda - su^\mu \partial_\mu \xi - \frac{1}{2}w(u^\mu u_\mu - 1) \quad (24)$$

By variations on n, s, u^μ respectively, we obtained the equations of motion

$$-u - u^\mu \partial_\mu \lambda = 0, \quad (25)$$

$$-T - u^\mu \partial_\mu \xi = 0, \quad (26)$$

$$-n \partial_\mu \lambda - s \partial_\mu \xi - w u_\mu = 0. \quad (27)$$

Combining with the constraints in Eq.(22) and following the Gibbs-Duhem relation

$$dp = sdT + ndu, \quad (28)$$

the equations of motion (25,26,27) can be written to the standard form of the relativistic hydrodynamic equation (18,20).

This derivation involves the constraints, and it will be more complicated for more constraints. But if we can parametrize n , s , u^μ in terms of a certain number of time dependent parameters $\vec{a}(t) = \{a_i(t), i = 1, \dots, N\}$

$$n = n(\mathbf{r}, \vec{a}(t), \frac{d\vec{a}(t)}{dt}), \quad (29)$$

$$s = s(\mathbf{r}, \vec{a}(t), \frac{d\vec{a}(t)}{dt}), \quad (30)$$

$$u^\mu = u^\mu(\mathbf{r}, \vec{a}(t), \frac{d\vec{a}(t)}{dt}), \quad (31)$$

$$(32)$$

the constraints are automatically satisfied, then the constraint terms in effective Lagrangian can be omitted. Therefore, we can write the effective Lagrangian in a simple form,

$$\mathcal{L}_{eff}(\vec{a}(t), \frac{d\vec{a}(t)}{dt}) = - \int d\mathbf{r} \epsilon(n, s). \quad (33)$$

Now we can obtain the equations of motion in the form of Euler-Lagrange equations, they are equations for the variables $a_i(t)$. It will be convenient to solve the equations of motion in such a simple form with few parameters. In this case, smoothed particle hydrodynamics is one of the most suitable numerical methods to solve the continuity equation.

2.2.2.1 Smoothed particle hydrodynamics

Since numerical simulation transforms problem with continuous variable into discrete form, it has become a very important tool for analyzing complex problems with the development of computer capabilities. To apply the numerical simulations to physical problems, we have the following procedure,

- Simplification and extraction of important physics from physical phenomena;
- Building mathematical model by using governing equations;
- Determine the computational frame by domain discretization with a finite number of particles;
- Specifying the numerical algorithms with initial and boundary conditions, numerical discretization of the system of partial differential equations;
- Coding and implementation, including the computational accuracy, speed and storage etc.;
- Numerical simulation.

The governing equations for fluid dynamic are the conservation equations, and we will adopt smoothed particle hydrodynamics algorithm to do numerical discretization, then translating the unsolvable partial differential equations to ordinary differential equations.

Smoothed particle hydrodynamics is a meshfree particle method based on Lagrangian formulation, it was first applied to solve astrophysical problems (LUCY, 1977; GINGOLD; MONAGHAN, 1977). The basic idea of SPH (LIU; LIU, 2010) is to describe the state of the system by a set of particles, each particle carries mass, velocity and other physical properties and moves according to the governing equations. Therefore, it can deal well with a large deformation experienced by the material. In this aspect, since the relativistic nuclear collisions involve a extremely compressed and high-temperature hadronic matter which expands into a very large space region, hence the SPH method is the best one to the studies of relativistic heavy ion collisions.

To obtain the SPH formulation of governing equations, there are two basically steps. One is the kernel approximation, from which field functions are approximated by integral representation method. The other one is particle approximation, replacing integrations with summations at the neighboring particles in a local domain so-called support domain.

In the kernel approximation step, one introduces the smoothing kernel function W for the approximation of a field function. Supposing a physical extensive quantity A with the corresponding density distribution $a(\mathbf{r}, t)$

$$a(\mathbf{r}, t) = \int a(\mathbf{r}', t) \delta(\mathbf{r} - \mathbf{r}') d^3 \mathbf{r}', \quad (34)$$

where Dirac δ -function is given by

$$\delta(\mathbf{r} - \mathbf{r}') = \begin{cases} 1, & \mathbf{r} = \mathbf{r}' \\ 0, & \mathbf{r} \neq \mathbf{r}'. \end{cases} \quad (35)$$

Replacing the Dirac δ -function by the smoothing function W with a finite spatial dimension h which is called smoothing length. The density $a(\mathbf{r}, t)$ is transformed to $\tilde{a}(\mathbf{r}, t)$

$$\tilde{a}(\mathbf{r}, t) = \int a(\mathbf{r}', t) W(\mathbf{r} - \mathbf{r}'; h) d^3 \mathbf{r}', \quad (36)$$

the smoothing function W satisfy the following conditions, W is normalized

$$\int W(\mathbf{r} - \mathbf{r}'; h) d^3 \mathbf{r}' = 1, \quad (37)$$

and with compact support

$$W(\mathbf{r} - \mathbf{r}'; h) \rightarrow 0, \quad \text{for } |\mathbf{r} - \mathbf{r}'| > h, \quad (38)$$

it also has Delta function property

$$\lim_{h \rightarrow 0} W(\mathbf{r} - \mathbf{r}'; h) = \delta(\mathbf{r} - \mathbf{r}'). \quad (39)$$

The second step, we introduce particle approximation to convert continuous integral representa-

tion to discretized forms of summation over finite number of particles in the support domain.

$$\tilde{a}(\mathbf{r}, t) \rightarrow a_{SPH}(\mathbf{r}, t) = \sum_i^N A_i W(\mathbf{r} - \mathbf{r}_i; h), \quad (40)$$

this is SPH representation of densities, where the continuous density is described by sum of finite number of unit distributions, $\{\mathbf{r}_i, i = 1, \dots, N\}$ is the position fixed on i th particle, the weight A_i represents the quantity of A carried by the i th SPH particle. From the normalization of the kernel W in Eq.(37), it is easy to obtain the total value of the quantity A of the system,

$$\int a_{SPH}(\mathbf{r}, t) d^3\mathbf{r} = \sum_i^N A_i. \quad (41)$$

In above, we obtained the discrete SPH representation of continuous densities of a physical extensive quantity by using two steps. Now we can take advantage of it to the analysis of relativistic heavy ion collisions, to transform the partial differential equations related to energy-momentum, entropy and baryon number into time-dependent ordinary differential equations.

First, we discretize the density of conserved quantities with smooth particles. In the space-fixed frame, the density of entropy and energy can be expressed as

$$s^*(\mathbf{r}, t) = \sum_i^N \nu_i W(\mathbf{r} - \mathbf{r}_i(t)), \quad (42)$$

$$\epsilon^*(\mathbf{r}, t) = \sum_i^N E_i W(\mathbf{r} - \mathbf{r}_i(t)), \quad (43)$$

where ν_i, E_i are the entropy and energy attached to the i th particle, and the total entropy and energy are

$$\int d^3\mathbf{r} s^*(\mathbf{r}, t) = \sum_i^N \nu_i, \quad (44)$$

$$\int d^3\mathbf{r} \epsilon^*(\mathbf{r}, t) = \sum_i^N E_i. \quad (45)$$

Then we choose entropy as the reference density, and the energy for the unit reference quantity s^* at the position $\mathbf{r} = \mathbf{r}_i(t)$ is

$$E_i = \left(\frac{\epsilon^*}{s^*} \right)_i \nu_i. \quad (46)$$

At the same time, we should take into account the relativistic effects in RHIC in order to find out the inherent characteristics of physical processes. The proper densities of entropy and baryon number can be related with these space-fixed frame quantities by a Lorentz factor

$$s = \gamma^{-1} s^*, \quad \epsilon = \gamma^{-1} \epsilon^*. \quad (47)$$

Therefore, according to Eqs.(43,46,47), we can write the effective Lagrangian Eq.(33) in SPH representation

$$\begin{aligned}\mathcal{L}_{eff}(\{\mathbf{r}, \dot{\mathbf{r}}\}) &= - \int d^3\mathbf{r} \sum_i \gamma^{-1} E_i W(\mathbf{r} - \mathbf{r}_i(t)) = - \sum_i \left(\frac{E}{\gamma} \right)_i \\ &= - \int d^3\mathbf{r} \sum_i \gamma^{-1} \left(\frac{\epsilon^*}{s^*} \right)_i \nu_i W(\mathbf{r} - \mathbf{r}_i(t)) = - \sum_i \nu_i (\epsilon/s^*)_i.\end{aligned}\quad (48)$$

According to variational principle, we can derive the equation of motion as follow

$$\frac{d}{dt} \left(\frac{p_i + \epsilon_i}{s_i} \nu_i \gamma_i \mathbf{v}_i \right) + \sum_j \nu_i \nu_j \left[\frac{p_i}{s_i^{*2}} + \frac{p_j}{s_j^{*2}} \right] \nabla_i W(\mathbf{r}_i - \mathbf{r}_j; h) = 0. \quad (49)$$

To solve the numerical discretized equations, we resort to SPheRIO code.

2.2.2.2 SPheRIO code

In the above, we learned how the SPH method parameterizes the material flow based on discrete Lagrangian coordinates (called SPH particles). Taking the entropy representation of the SPH model, and by using the variational principle to derive the equation of motion, the SPH degree of freedom is determined. The main advantage of this method is that it can handle any type of geometry and violent dynamics. For example, as long as the size of the SPH particles is appropriately selected, the shock wave phenomenon can be handled without numerical difficulty.

As a numerical implementation of SPH method, SPheRIO code is an ideal hydrodynamic code using the Smoothed Particle Dynamics algorithm (Monaghan, 1992; AGUIAR et al., 2001; MOTA; CHEN; QIAN, 2017). In the assumptions that the hot and dense matter created in high-energy collision reaches a local equilibrium, the SPheRIO code is employed to do hydrodynamical simulations for relativistic high-energy collisions (HAMA; KODAMA; JR., 2005; TAKAHASHI et al., 2009; ANDRADE et al., 2010a; ANDRADE et al., 2012; QIAN et al., 2007b; QIAN et al., 2007a; DUDEK et al., 2014; CASTILHO et al., 2018). We use the ICs represented by the distribution of fluid velocities, energy-momentum tensor, baryon-number, strangeness, etc. for a given time parameter as input of SPheRIO code. The initial conditions can be generate by using some event generator in simulations, for example, HIJING (GYULASSY; RISCHKE; ZHANG, 1997), VNI (SCHLEI; STROTTMAN, 1999), URASiMA (NONAKA; HONDA; MUROYA, 2000), NeXuS (DRESCHER et al., 2002a). At the same time, the equation of state describing the thermodynamic relationship is also needed, it can reduce the degree of freedom of the hydrodynamic equation of motion.

As the system expands and cools, it proceed to the decoupling stage of the hydrodynamic model, the constituent particles will eventually stop interacting with each other and be emitted as free particles. Thus, at the end of hydrodynamic evolution, we need the decoupling prescriptions in SPheRIO code to specify where and when the freeze-out happens. There are three different freeze-out scenarios, namely, thermal freeze-out, thermal and chemical freeze-out, and a continuous emission (CE).

In general, we can investigate the properties of the QGP through IC, EOS, Decoupling Criteria with the help of SPheRIO. Many works show that SPheRIO can reproduce the results of the experi-

ment in many aspects. For example, Fig. 3 and Fig. 4 are SPheRIO simulation results in comparison to experimental data. NeXuS provides initial conditions of Au+Au collisions at $\sqrt{s_{NN}} = 200$ GeV, which is specified in terms of number density, energy density and baryon density, then SPheRIO is used to simulate the hydrodynamical evolution in each NeXuS event. Then we obtain the pseudorapidity distribution and transverse momentum distributions of charged particle at different centrality, as shown in Fig. 3 and Fig. 4. We can find that SPheRIO almost reproduces the pseudorapidity and transverse momentum distributions observed in experiments. In addition, SPheRIO also provides a good description of particle correlations and collective flow. We will briefly introduce the collective flow in next chapter.

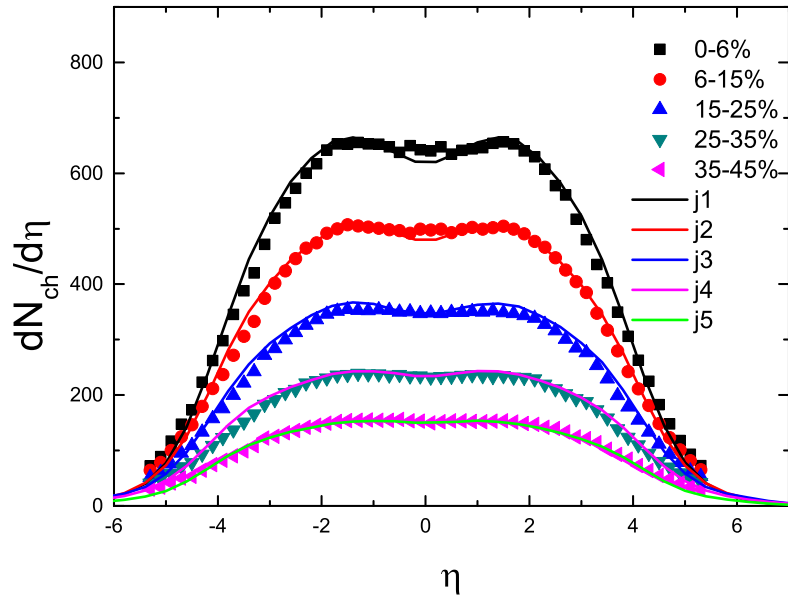


Fig. 3 – (Color online) The charged particle pseudorapidity distributions for different centrality in $\sqrt{s_{NN}} = 200$ GeV Au+Au collisions, the scatters are PHOBOS data (BACK et al., 2003), and the solid lines are the corresponding SPheRIO simulation results.

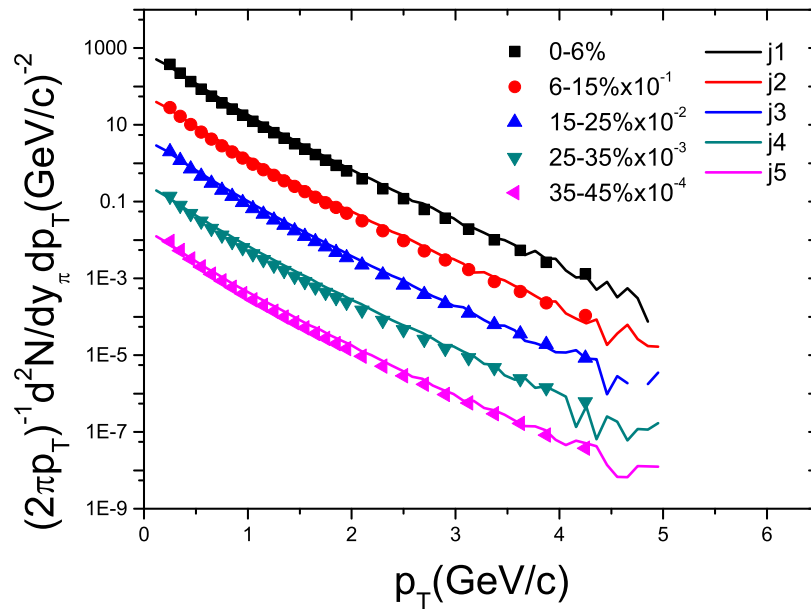


Fig. 4 – (Color online) Charged hadron transverse momentum distributions for different centrality in Au+Au collisions at $\sqrt{s_{NN}} = 200$ GeV, the scatters are PHOBOS data (BACK et al., 2004), and the solid lines are corresponding SPhErio simulation results.

3 COLLECTIVE FLOW

As we mentioned in 2.2, the space-time evolution of a nucleus-nucleus collisions undergo the formation of QGP, hydrodynamic evolution, hadronization. It implies that the nature of the final state hadron is closely related to the initial QGP and its evolution, so we can study the strongly interacting QGP by analyzing the behavior of final state hadrons. Therefore, a large amount of experimental measurements and theoretical analysis are devoted to study the relation between final state hadrons and the initial hot and dense matter. Subsequently, some collective behavior was observed, this so called collective flow is known as the response to the properties of collision system in the early stages (DANIELEWICZ; ODYNIC, 1985; WELKE et al., 1988; WANG et al., 1991).

Taking into account the different directions of the collective movement, the collective flow is classified into longitudinal flow and transverse flow. Longitudinal flow is the collective motion of a large number of particles in the direction of the initial beam, and transverse flow is the collective motion of a large number of particles in the transverse plane which orthogonal to the beam. Furthermore, transverse flow includes radial flow arose in central collisions and anisotropic flow arose in non-central collisions (OLLITRAULT, 1998), they reflect the different physical scenarios. Since anisotropic flow is sensitive to the interaction between the constituent materials very early in the system evolution, it can provide us informations about the stage where the QGP may be the main player, such as the degree of thermalization of the produced matter, equation of state and so on. What's more, the large momentum anisotropy of particle emission in the transverse plane is observed in experiments (BARRETTE et al., 1994; BARRETTE et al., 1997; ALT et al., 2003). Therefore, as the most direct observation in the experiment, the anisotropic collective flow has attracted a lot of attention.

Anisotropic collective flow is the observed anisotropies of the azimuthal distribution in the momentum space. In non-central heavy-ion collisions (VOLOSHIN; POSKANZER; SNELLINGS, 2010), the two collision nuclei create an elliptical overlap region in transverse plane ($x - y$ plane) in which an anisotropic pressure gradient is formed. With the expansion of the system driven by the pressure gradient, the anisotropy of the initial coordinate space is transformed to the anisotropy of the momentum space. To quantify the anisotropy flow, it is customary to expand the single particle azimuthal distribution in a Fourier series, the harmonic coefficients are used for a quantitative characterization of the event anisotropy. The second order coefficient, referred to as elliptic flow, is closely related to the initial geometry.

Furthermore, we often understand the two-particle correlations in terms of flow harmonics. As we know, the “ridge” and “shoulders” structures of two-particle correlations are observed, which are thought to be mainly dominated by two distinct contributions, that are elliptic flow and triangular flow (ADARE et al., 2008; BHALERAO; LUZUM; OLLITRAULT, 2011). The elliptic flow term related to anisotropic hydrodynamic expansion of the medium from an anisotropic initial state, and the triangular flow term related to event-by-event fluctuating IC. Thereby, the two-particle correlation can provide us more informations about the particle interactions at early stage.

Many efforts have been devoted to the relationship between initial state eccentricities and final

state anisotropies (TEANEY; YAN, 2011; TEANEY; YAN, 2012; GARDIM et al., 2012; NIEMI et al., 2012; QIAN et al., 2014; GARDIM et al., 2015; FU, 2015). A quantitative notion on the decomposition of the anisotropic IC was first proposed in Ref. (TEANEY; YAN, 2011; TEANEY; YAN, 2012). The key idea of the study is that anisotropy of the IC can be decomposed in terms of a cumulant expansion, where the resulting expansion coefficients correspond to the “connected” part of the eccentricity at a given order. Therefore, a higher-order cumulant, by definition, has the contributions from the “disconnected” combinations of the lower orders ones subtracted. Moreover, flow harmonics are understood as the hydrodynamic response to IC fluctuations classified in terms of cumulants, while the lowest cumulants are assumed to have dominant effects. In literature, for a given flow harmonic order, the contribution proportional to the cumulant of the same azimuthal order is attributed as much to the linear response. While those proportional to the combinations of lower-order cumulants, which give rise to the same azimuthal order, are referred to as the nonlinear response. In practice, it is noted that the response strength from different cumulant combinations is different. Therefore, the “best estimator” is manually taken to minimize the deviation from the perfect correlation (GARDIM et al., 2012; GARDIM et al., 2015). To be more specific, the mapping between IC and flow harmonics resides in the correlation between an optimized linear combination of a given set of cumulant products and the corresponding flow harmonics. By numerical studies, such a mapping or correlation is understood to be mostly established, particularly for the most central collisions. These works have incited further efforts concerning this train of thought (NIEMI et al., 2012; FU, 2015).

Another direction of approach is associated with flow analysis, and particularly concerning the higher harmonics and particle correlations. Symmetric cumulant was proposed in Ref. (BILANDZIC et al., 2014) as a distinct observable tailored for the correlations between flow harmonics. In particular, the symmetric cumulant does not depend on any particular event plane, neither on the correlation between them. Moreover, it vanishes if the fluctuations of different flow harmonics are independent. In this context, it is an excellent observable which is exclusively dedicated to exploring the correlations between the flow harmonics and their fluctuations. As a comparison, event plane correlations can be studied by using the method proposed in Ref. (BHALERAO; OLLITRAULT; PAL, 2013). In fact, most of the above observables can be formally expressed in terms of the moments of flow, as discussed in Ref. (BHALERAO; OLLITRAULT; PAL, 2015). Here, the definitions of other quantities are derived through that of the complex anisotropic flow coefficient of n th harmonics V_n , namely, the Fourier coefficient of one particle distribution. By evaluating the Pearson correlation coefficients between moments and other appropriately chosen quantities, one obtains the desired flow fluctuations, symmetric cumulant, and event plane correlations.

More recently, the nonlinear response regarding ratios of mixed higher-order harmonic moments has been investigated by several authors. Numerical studies are carried out in terms of transport as well as hydrodynamic models while the results are compared against the data (BHALERAO; OLLITRAULT; PAL, 2015; YAN; OLLITRAULT, 2015; YAN; PAL; OLLITRAULT, 2016). The ratio of the event average of the products of anisotropic flow coefficient, subsequently, give rise to various observables such as $v_n \{ \Psi_m \}$, event planes correlation measured by CMS and ATLAS Collaborations.

Furthermore, according to the spirit of IC Fourier decomposition, the flow harmonics are divided into linear and nonlinear parts. The analyzes are entirely based on flow harmonics, not directly related to IC eccentricities. The linear response is attributed to IC fluctuations while the nonlinear part is to the mean geometric eccentricity. To separate the linear and nonlinear decompositions, in particular, the linear responses are assumed to be uncorrelated to the nonlinear ones. The latter can be, again, expressed in terms of the ratios of the event average of the products of anisotropic flow coefficients. Hydrodynamic simulations show that the corresponding results are comparable to the data.

In following, there are some quantitative description of initial geometry and anisotropic flow. We briefly review the method used to calculate the eccentricity, flow harmonics, nonlinear response coefficients, as well as two-particle correlations.

3.1 ECCENTRICITY

The earliest quantitative description of spatial anisotropy was referred to as eccentricity (SORGE, 1999), defined by

$$\varepsilon = \frac{\langle y^2 - x^2 \rangle}{\langle y^2 + x^2 \rangle}, \quad (1)$$

where the average is calculated with some weight, we can choose nuclear profile density (participant nucleons), entropy or energy densities, or something else (e.g. number of binary collisions) as the weight.

And then the participant eccentricity (ALVER et al., 2007; ALVER; ROLAND, 2010) is introduced by

$$\varepsilon_2 = \frac{\sqrt{(\sigma_y^2 - \sigma_x^2)^2 + 4(\sigma_{xy})^2}}{\sigma_y^2 + \sigma_x^2} \quad (2)$$

with

$$\sigma_x^2 = \langle x^2 \rangle - \langle x \rangle^2, \quad (3)$$

$$\sigma_y^2 = \langle y^2 \rangle - \langle y \rangle^2, \quad (4)$$

$$\sigma_{xy}^2 = \langle xy \rangle - \langle x \rangle \langle y \rangle, \quad (5)$$

where x and y denote the position of the participant nucleon in transverse plane.

After the third-order Fourier coefficient was discussed in Ref (ALVER; ROLAND, 2010), Teaney and Yan generalized the concept to higher order, and introduced a cumulant expansion to parameterize possible initial conditions (TEANEY; YAN, 2011; TEANEY; YAN, 2012). In general, the eccentricity defined by the transverse position (r, ϕ) of the participating nucleons in their center of mass is given

by

$$\begin{aligned}
\varepsilon_{n,n} e^{in\Phi_{n,n}} = \varepsilon_n e^{in\Phi_n} &= -\frac{\langle r^n e^{in\phi} \rangle}{\langle r^n \rangle} \\
&= -\frac{\int r dr d\phi r^n e^{in\phi} \rho(r, \phi)}{\int r dr d\phi r^n \rho(r, \phi)}, \\
\varepsilon_1 e^{i\Phi_1} &= -\frac{\langle r^3 e^{i\phi} \rangle}{\langle r^3 \rangle}.
\end{aligned} \tag{6}$$

Considering

$$\begin{aligned}
\varepsilon_n e^{in\Phi_n} \cdot \varepsilon_n e^{-in\Phi_n} &= \left(-\frac{\langle r^n e^{in\phi} \rangle}{\langle r^n \rangle}\right) \cdot \left(-\frac{\langle r^n e^{-in\phi} \rangle}{\langle r^n \rangle}\right) \\
&= \frac{\langle r^n \cos(n\phi) + ir^n \sin(n\phi) \rangle \langle r^n \cos(n\phi) - ir^n \sin(n\phi) \rangle}{\langle r^n \rangle^2} \\
&= \frac{\langle r^n \cos(n\phi) \rangle^2 + \langle r^n \sin(n\phi) \rangle^2}{\langle r^n \rangle^2},
\end{aligned} \tag{7}$$

thus Eq.6 is equivalent to

$$\varepsilon_n = \frac{\sqrt{\langle r^n \cos(n\phi) \rangle^2 + \langle r^n \sin(n\phi) \rangle^2}}{\langle r^n \rangle}, \tag{8}$$

$$\varepsilon_1 = \frac{\sqrt{\langle r^3 \cos(\phi) \rangle^2 + \langle r^3 \sin(\phi) \rangle^2}}{\langle r^3 \rangle}, \tag{9}$$

with eccentricity plane

$$\Phi_n = \frac{1}{n} \arctan \left(\frac{\langle r^n \sin(n\phi) \rangle}{\langle r^n \cos(n\phi) \rangle} \right) + \frac{\pi}{n}, \quad (n > 1) \tag{10}$$

$$\Phi_1 = \arctan \left(\frac{\langle r^3 \sin(\phi) \rangle}{\langle r^3 \cos(\phi) \rangle} \right) + \pi, \tag{11}$$

where the weight average $\langle \dots \rangle = \int \dots \rho(r, \phi) r dr d\phi / \int \rho(r, \phi) r dr d\phi$ takes the density $\rho(r, \phi)$ as weight.

Then, one can analyze the anisotropic collective flow for a given eccentricity described by the cumulant expansion of initial condition. And the anisotropic collective flow is quantified by Fourier expansion coefficients of the particle azimuthal distribution as in following section.

3.2 FLOW HARMONICS

The particle azimuthal distribution with respect to the reaction plane always can be expanded into Fourier series (VOLOSHIN; ZHANG, 1996),

$$\frac{dN}{d\phi} \propto 1 + 2 \sum_{n=1}^{\infty} v_n \cos[n(\phi - \Psi_{RP})]. \tag{12}$$

By using the orthogonality properties of trigonometric functions, one can obtain the coefficients

$$v_n = \langle \cos[n(\phi_i - \Psi_{RP})] \rangle, \quad (13)$$

where ϕ_i is the azimuthal angles of the produced particles in momentum space, Ψ_{RP} is the n th reaction plane defined by the impact parameter and the beam direction. “ $\langle \dots \rangle$ ” represents the average over all particles in all events, since the flow harmonic v_n is symmetrical with respect to its own reaction plane, the sine term is canceled out.

Therefore, anisotropic collective flow is quantified by harmonics of flow, which is measured with respect to their own reaction plane. The first coefficient v_1 is referred to as directed flow, the second coefficient v_2 is referred to as elliptic flow, the third coefficient v_3 is referred to as triangular flow, etc.

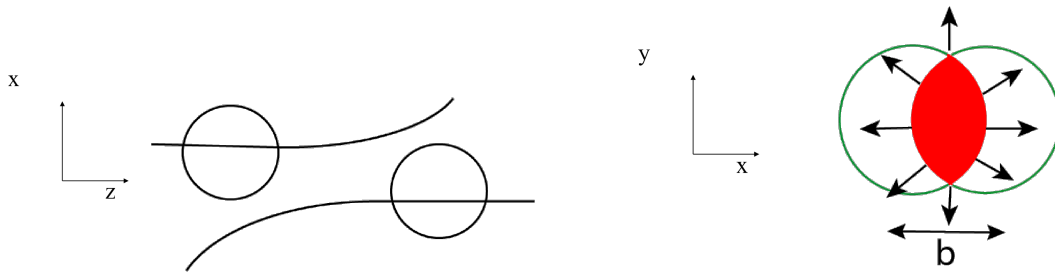


Fig. 5 – (Color online) Left: directed flow. Right: elliptic flow. (VOLOSHIN; POSKANZER; SNELLINGS, 2010)

In RHIC and LHC experiments (AAMODT et al., 2012; AAD et al., 2012; ADARE et al., 2011; AAD et al., 2013), people have observed the non-zero v_n for $n \leq 6$. About the measurements of v_n , we have to be aware of that, what we directly measured in the experiment is the azimuthal angles of the produced particles, rather than reaction plane angle. To evaluate the flow harmonic v_n in realistic situations, some experimental methods are developed, for instance, event plane method (BARRETTE et al., 1997; POSKANZER; VOLOSHIN, 1998), two and many particle correlations (WANG et al., 1991), q-distributions (ADLER et al., 2002), Lee-Yang Zeros (ABELEV et al., 2008; BHALERAO; BORGHINI; OLLITRAULT, 2003), Bessel and Fourier transforms (VOLOSHIN, 2006). Our study on anisotropic flow is based on event plane method, so we will give a brief introduction on it in next section.

3.3 EVENT PLANE METHOD

Although we can't directly measure the azimuth angle of the reaction plane, we can estimate it by particle azimuth distribution, and the estimated reaction plane is called event plane. According to Ref.(POSKANZER; VOLOSHIN, 1998), the event plane angle Ψ_n is the azimuthal angle of flow

vector \mathbf{Q}_n , the event flow vector \mathbf{Q}_n in the transverse plane is defined by

$$Q_{n,x} = \sum_i w_i \cos(n\phi_i) = \mathbf{Q}_n \cos(n\Psi_n), \quad (14)$$

$$Q_{n,y} = \sum_i w_i \sin(n\phi_i) = \mathbf{Q}_n \sin(n\Psi_n), \quad (15)$$

where ϕ_i and w_i are the measured azimuthal angle and weight for particle i , and the sums go over the i particles used in the event plane determination. Therefore, the observed event plane angle Ψ_n for n th harmonic of the anisotropic flow is given by

$$\Psi_n = \frac{1}{n} \arctan \left[\frac{Q_{n,y}}{Q_{n,x}} \right] = \frac{1}{n} \arctan \left[\frac{\sum_i w_i \sin(n\phi_i)}{\sum_i w_i \cos(n\phi_i)} \right], \quad (16)$$

with the range $0 \leq \Psi_n \leq 2\pi/n$.

Then, the observed v_n can be evaluated by using event plane,

$$v_n^{obs} = \langle \cos[n(\phi_i - \Psi_n)] \rangle. \quad (17)$$

However, the number of detected particles used to estimating event plane is finite, the event plane is not exactly equal to reaction plane. To obtain the accurate harmonic v_n , we need to find the relation between v_n^{obs} and v_n , we have following analysis

$$\begin{aligned} v_n^{obs} &= \langle \cos[n(\phi_i - \Psi_{RP}) + n(\Psi_{RP} - \Psi_n)] \rangle \\ &= \langle \cos[n(\phi_i - \Psi_{RP})] \cos[n(\Psi_{RP} - \Psi_n)] \rangle \\ &\quad - \langle \sin[n(\phi_i - \Psi_{RP})] \sin[n(\Psi_{RP} - \Psi_n)] \rangle \\ &= \langle \cos[n(\phi_i - \Psi_{RP})] \rangle \langle \cos[n(\Psi_{RP} - \Psi_n)] \rangle, \end{aligned} \quad (18)$$

where the sine term vanished because of the symmetry. Thus, we can get the harmonic v_n by a correction,

$$v_n = \frac{v_n^{obs}}{\mathcal{R}_n}, \quad (19)$$

where the event plane resolution is

$$\mathcal{R}_n = \langle \cos[n(\Psi_{RP} - \Psi_n)] \rangle, \quad (20)$$

and we can estimate the event plane resolution from the correlation of the planes of independent sub-events,

$$\mathcal{R}_n = \sqrt{\langle \cos[n(\Psi_n^A - \Psi_n^B)] \rangle}, \quad (21)$$

on account of following derivation

$$\begin{aligned}
\langle \cos[n(\Psi_n^A - \Psi_n^B)] \rangle &= \langle \cos[n(\Psi_n^A - \Psi_{RP}) - n(\Psi_n^B - \Psi_{RP})] \rangle \\
&= \langle \cos[n(\Psi_n^A - \Psi_{RP})] \cos[n(\Psi_n^B - \Psi_{RP})] \rangle \\
&+ \langle \sin[n(\Psi_n^A - \Psi_{RP})] \sin[n(\Psi_n^B - \Psi_{RP})] \rangle \\
&= \langle \cos[n(\Psi_n^A - \Psi_{RP})] \rangle \langle \cos[n(\Psi_n^B - \Psi_{RP})] \rangle \\
&= \mathcal{R}_n^2.
\end{aligned} \tag{22}$$

Simply put, in event plane method, we estimated the event plane angle by using azimuthal angle of outgoing particles. Then, we evaluate the Fourier expansion coefficients of the particle azimuthal distribution respect to the event plane. At last, the coefficients v_n is calculated by dividing the observed v_n^{obs} by the event plane resolution, which is estimated from the correlation between two sub-events.

3.4 NONLINEAR HYDRODYNAMIC RESPONSE

A series of work shows that there is a linear relation between v_2 and participant eccentricity ε_2 (ALVER; ROLAND, 2010; ALVER et al., 2010; PETERSEN et al., 2010; TEANEY; YAN, 2011; QIN et al., 2010; QIAN et al., 2014). But the linear relation between v_n and ε_n breaks down for $n > 2$, since the high-order harmonics involves the nonlinear hydrodynamic response.

In Ref.(YAN; OLLITRAULT, 2015; YAN; PAL; OLLITRAULT, 2016), a set of nonlinear response coefficients χ_n is proposed to study higher order harmonic flow. The single-particle distribution can be expressed in a complex form,

$$P(\phi) = \frac{1}{2\pi} \sum_{n=-\infty}^{+\infty} V_n e^{-in\phi}. \tag{23}$$

Then the complex anisotropic flow coefficient of n th harmonics V_n is

$$V_n = v_n e^{in\Psi_n}, \tag{24}$$

where $|V_n| = v_n$ can be calculated by using Eq.(13).

The higher order flow harmonics v_n can be measured with respect to their own event-plane, and

plane constructed by lower order flow harmonics,

$$\begin{aligned}
v_n\{\Psi_m\} &= \left\langle \int_0^{2\pi} d\phi P(\phi) \cos[n(\phi - \Psi_m)] \right\rangle, \\
&= \left\langle \int_0^{2\pi} d\phi \frac{1}{2\pi} \sum_{k=-\infty}^{+\infty} v_k e^{-ik(\phi - \Psi_k)} \cos[n(\phi - \Psi_m)] \right\rangle, \\
&= 2 \left\langle \int_0^{2\pi} d\phi \frac{1}{2\pi} v_n [\cos[n(\phi - \Psi_n)] - i \sin[n(\phi - \Psi_n)]] \cos[n(\phi - \Psi_m)] \right\rangle, \\
&= \frac{1}{\pi} \left\langle \int_0^{2\pi} d\phi v_n [\cos^2(n\phi) \cos(n\Psi_m) \cos(n\Psi_n) + \sin^2(n\phi) \sin(n\Psi_m) \sin(n\Psi_n)] \right\rangle \\
&\quad - i \frac{1}{\pi} \left\langle \int_0^{2\pi} d\phi v_n [\sin^2(n\phi) \sin(n\Psi_m) \cos(n\Psi_n) - \cos^2(n\phi) \cos(n\Psi_m) \sin(n\Psi_n)] \right\rangle, \\
&= \langle v_n \cos[n(\Psi_m - \Psi_n)] \rangle - i \langle v_n \sin[n(\Psi_m - \Psi_n)] \rangle, \\
&= \langle v_n \cos[n(\Psi_m - \Psi_n)] \rangle, \tag{25}
\end{aligned}$$

therefore

$$\begin{aligned}
v_4\{\Psi_2\} &= \frac{\text{Re}\langle V_4(V_2^*)^2 \rangle}{\sqrt{\langle |V_2|^4 \rangle}} = \langle v_4 \cos[4(\Psi_2 - \Psi_4)] \rangle, \\
v_6\{\Psi_2\} &= \frac{\text{Re}\langle V_6(V_2^*)^3 \rangle}{\sqrt{\langle |V_2|^6 \rangle}} = \langle v_6 \cos[6(\Psi_2 - \Psi_6)] \rangle, \\
v_6\{\Psi_3\} &= \frac{\text{Re}\langle V_6(V_3^*)^2 \rangle}{\sqrt{\langle |V_3|^4 \rangle}} = \langle v_6 \cos[6(\Psi_3 - \Psi_6)] \rangle, \\
v_5\{\Psi_{23}\} &= \frac{\text{Re}\langle V_5 V_2^* V_3^* \rangle}{\sqrt{\langle |V_2|^2 |V_3|^2 \rangle}} = \langle v_5 \cos(5\Psi_5 - 2\Psi_2 - 3\Psi_3) \rangle, \\
v_7\{\Psi_{23}\} &= \frac{\text{Re}\langle V_7(V_2^*)^2 V_3^* \rangle}{\sqrt{\langle |V_2|^4 |V_3|^2 \rangle}} = \langle v_7 \cos(7\Psi_7 - 4\Psi_2 - 3\Psi_3) \rangle. \tag{26}
\end{aligned}$$

Above equations indicate that the measurements of higher order flow harmonics in the event plane of V_2 and/or V_3 are equivalent to the corresponding measurement of event plane correlations.

The nonlinear response coefficients are induced by assuming that higher order harmonics are the superposition of medium nonlinear and linear responses, as follows,

$$\begin{aligned}
V_4 &= V_{4L} + \chi_4 (V_2)^2, \\
V_5 &= V_{5L} + \chi_5 V_2 V_3, \\
V_6 &= V_{6L} + \chi_{62} (V_2)^3 + \chi_{63} (V_3)^2, \\
V_7 &= V_{7L} + \chi_7 (V_2)^2 V_3, \tag{27}
\end{aligned}$$

where components V_{4L} , V_{5L} , V_{6L} , V_{7L} are linearly proportional to ε_4 , ε_5 , ε_6 , ε_7 respectively, and the nonlinear terms relate to the lowest-order harmonics V_2 and V_3 . χ_n can be interpreted as ratios between nonlinear and linear flow response coefficients.

By using some general assumptions, the non-linear parts is isolated from the linear part as follows

$$\begin{aligned}
\chi_4 &= \frac{\langle V_4(V_2^*)^2 \rangle}{\langle |V_2|^4 \rangle}, \\
\chi_5 &= \frac{\langle V_5 V_2^* V_3^* \rangle}{\langle |V_2|^2 |V_3|^2 \rangle}, \\
\chi_{62} &= \frac{\langle V_6(V_2^*)^3 \rangle}{\langle |V_2|^6 \rangle}, \\
\chi_{63} &= \frac{\langle V_6(V_3^*)^2 \rangle}{\langle |V_3|^4 \rangle}, \\
\chi_7 &= \frac{\langle V_7(V_2^*)^2 V_3^* \rangle}{\langle |V_2|^4 |V_3|^2 \rangle}.
\end{aligned} \tag{28}$$

Substituting Eq.(24) into above nonlinear response coefficients Eq.(28), we obtained

$$\begin{aligned}
\chi_4 &= \frac{\langle v_4 v_2^2 e^{i(4[\Psi_4 - \Psi_2])} \rangle}{\langle v_2^4 \rangle} \\
&= \frac{\langle v_4 v_2^2 \cos(4[\Psi_4 - \Psi_2]) \rangle + i \langle v_4 v_2^2 \sin(4[\Psi_4 - \Psi_2]) \rangle}{\langle v_2^4 \rangle}, \\
\chi_5 &= \frac{\langle v_5 v_2 v_3 e^{i(5\Psi_5 - 2\Psi_2 - 3\Psi_3)} \rangle}{\langle v_2^2 v_3^2 \rangle} \\
&= \frac{\langle v_5 v_2 v_3 \cos(5\Psi_5 - 2\Psi_2 - 3\Psi_3) \rangle + i \langle v_5 v_2 v_3 \sin(5\Psi_5 - 2\Psi_2 - 3\Psi_3) \rangle}{\langle v_2^2 v_3^2 \rangle}, \\
\chi_{62} &= \frac{\langle v_6 v_2^3 e^{i(6[\Psi_6 - \Psi_2])} \rangle}{\langle v_2^6 \rangle} \\
&= \frac{\langle v_6 v_2^3 \cos(6[\Psi_6 - \Psi_2]) \rangle + i \langle v_6 v_2^3 \sin(6[\Psi_6 - \Psi_2]) \rangle}{\langle v_2^6 \rangle}, \\
\chi_{63} &= \frac{\langle v_6 v_3^2 e^{i(6[\Psi_6 - \Psi_3])} \rangle}{\langle v_3^4 \rangle} \\
&= \frac{\langle v_6 v_3^2 \cos(6[\Psi_6 - \Psi_3]) \rangle + i \langle v_6 v_3^2 \sin(6[\Psi_6 - \Psi_3]) \rangle}{\langle v_3^4 \rangle}, \\
\chi_7 &= \frac{\langle v_7 v_2^2 v_3 e^{i(7\Psi_7 - 4\Psi_2 - 3\Psi_3)} \rangle}{\langle v_2^4 v_3^2 \rangle} \\
&= \frac{\langle v_7 v_2^2 v_3 \cos(7\Psi_7 - 4\Psi_2 - 3\Psi_3) \rangle + i \langle v_7 v_2^2 v_3 \sin(7\Psi_7 - 4\Psi_2 - 3\Psi_3) \rangle}{\langle v_2^4 v_3^2 \rangle},
\end{aligned} \tag{29}$$

where $\langle \dots \rangle$ represents the average over all events, and the imaginary part infinitely close to zero for a large number of events.

Then substituting equations (26) into above equations of nonlinear response coefficients, we ob-

tained

$$\begin{aligned}
\chi_4 &= \frac{\langle v_4 \{ \Psi_2 \} \rangle}{\sqrt{\langle |V_2|^4 \rangle}}, \\
\chi_5 &= \frac{\langle v_6 \{ \Psi_2 \} \rangle}{\sqrt{\langle |V_2|^2 |V_3|^2 \rangle}}, \\
\chi_{62} &= \frac{\langle v_6 \{ \Psi_3 \} \rangle}{\sqrt{\langle |V_2|^6 \rangle}}, \\
\chi_{63} &= \frac{\langle v_5 \{ \Psi_{23} \} \rangle}{\sqrt{\langle |V_3|^4 \rangle}}, \\
\chi_7 &= \frac{\langle v_7 \{ \Psi_{23} \} \rangle}{\sqrt{\langle |V_2|^4 |V_3|^2 \rangle}}.
\end{aligned} \tag{30}$$

Therefore, the Eq.(29) can be calculated in hydrodynamics, and the Eq.(30) can be inferred from experimental data.

3.5 TWO-PARTICLE CORRELATIONS

In section 3.3, we learned the event plane method for flow analysis which relies on the azimuthal correlation between particle and the event plane, azimuthal correlation between two sub-events. From another perspective, we also can study flow by using two-particle correlation (WANG et al., 1991; VOLOSHIN; POSKANZER; SNELLINGS, 2010) which do not need to estimate reaction plane.

The correlation between particle and the reaction plane can introduce the correlation between particles. Supposing the azimuth angle difference between two correlated particles is $\Delta\phi$, and their corresponding Fourier expansion coefficients are v_n^T , v_n^A respectively. From the single-particle azimuthal distribution in Eq.(12), the particle-pair distribution can be derived as follows

$$\begin{aligned}
\frac{dN_{pair}}{d\Delta\phi} &\propto \frac{1}{2\pi} \int_0^{2\pi} \frac{dN}{d\phi}(\phi) \frac{dN}{d\phi}(\phi + \Delta\phi) d\phi \\
&= \frac{1}{2\pi} \int_0^{2\pi} \left[1 + \sum_{n=1}^{\infty} 2v_n^T \cos[n(\phi - \Psi_{RP})] \right] \left[1 + \sum_{n=1}^{\infty} 2v_n^A \cos[n(\phi + \Delta\phi - \Psi_{RP})] \right] d\phi \\
&= 1 + \frac{1}{2\pi} \int_0^{2\pi} \left[\sum_{n=1}^{\infty} 2v_n^T \cos[n(\phi - \Psi_{RP})] \cdot \sum_{n=1}^{\infty} 2v_n^A \cos[n(\phi + \Delta\phi - \Psi_{RP})] \right] d\phi,
\end{aligned} \tag{31}$$

by considering the orthogonality properties of trigonometric functions

$$\begin{aligned}
n \neq k, & \int_0^{2\pi} 2v_n^T \cos[n(\phi - \Psi_{RP})] \cdot 2v_k^A \cos[k(\phi + \Delta\phi - \Psi_{RP})] d\phi = 0, \\
n = k, & \int_0^{2\pi} 2v_n^T \cos[n(\phi - \Psi_{RP})] \cdot 2v_n^A \cos[n(\phi + \Delta\phi - \Psi_{RP})] d\phi = 4\pi v_n^T v_n^A \cos(n\Delta\phi).
\end{aligned} \tag{32}$$

Then the two-particle azimuthal distribution is obtained

$$\frac{dN_{pair}}{d\Delta\phi} \propto 1 + \sum_{n=1}^{\infty} 2v_n^T v_n^A \cos(n\Delta\phi). \quad (33)$$

It is easy to find that the angle of event plane is not used in the two-particle correlation distribution function. Moreover, a simpler technique have been proposed to extract flow harmonic v_n from two-particle correlations (SCHLAGHECK, 1999; PRENDERGAST et al., 2000; SINGH; JAIN, 1994). However, in addition to the contribution of the anisotropic flow, the two-particle correlation also has some non-flow contributions (DINH; BORGHINI; OLLITRAULT, 2000; BORGHINI; OLLITRAULT; DINH, 2000). To obtain the accurate and reliable results, we need to eliminate the effects of non-flow correlations, such as using the flow analysis from cumulant expansion of multiparticle azimuthal correlation (BORGHINI; DINH; OLLITRAULT, 2001).

In turn, we often understand the two-particle correlation in terms of flow harmonic v_n . Many methods (ULERY; WANG, 2009; SHARMA; PRUNEAU, 2009; ADAMS et al., 2005b; ADLER et al., 2006; MA et al., 2006; PUTSCHKE, 2007) have been proposed in both theoretical and experimental studies of two-particle correlation. To calculate the two-particle correlation, first, we pick a trigger particle whoes transverse momentum is p_T^T , azimuthal angle is ϕ^T . Then, the particles correlated with the trigger particle is picked out as associated particles whoes transverse momentum is p_T^A , azimuthal angle is ϕ^A . Generally speaking $p_T^T > p_T^A$, the distribution of the azimuthal angle difference $\Delta\phi = \phi^A - \phi^T$ gives the raw correlation function. By convention, what we are interested in is the correlations that the background has been subtracted,

$$J(\Delta\phi) = C(\Delta\phi) - B(\Delta\phi). \quad (34)$$

The background distribution B can be constructed by mixed pairs which is formed by using particles from different events, and C is evaluated by using the particle pairs from the same event. The correlation function is normalized by dividing the number of trigger particles.

Additionally, the two-particle correlations also can be calculated by using ZYAM method to subtract the effects of elliptic flow that from background. The ZYAM method (AJITANAND et al., 2005; ADLER et al., 2006) is based on the two source model which express the correlation function as a sum of harmonic correlations and di-jet correlations $J(\Delta\phi)$,

$$C(\Delta\phi) = \xi(1 + 2 \langle v_2^T v_2^A \rangle \cos 2\Delta\phi) + J(\Delta\phi), \quad (35)$$

where v_2^T and v_2^A are the elliptic flow coefficients of trigger and associated particle respectively. The di-jet function has a negligible intensity at the minimum $\Delta\phi_{min}$, which is the zero yield at minimum (ZYAM),

$$J(\Delta\phi_{min}) = 0, \quad (36)$$

then

$$C(\Delta\phi_{min}) = \xi(1 + 2 \langle v_2^T v_2^A \rangle \cos 2\Delta\phi_{min}), \quad (37)$$

where the elliptic flow can be calculated by using event-plane method, then we can fix the factor ξ at the minimum $\Delta\phi_{min}$, finally we can get the subtraction correlation $J(\Delta\phi)$.

In following chapter, we study the origin of these special two-particle correlation structure by using peripheral tube model.

4 ON THE PERIPHERAL TUBE DESCRIPTION OF THE TWO-PARTICLE CORRELATIONS IN NUCLEAR COLLISIONS

The two-particle correlation analysis was originally employed to extract the information on jet, by subtracting the background global features such as those generated by collective expansion. However, as it was applied to the study of jet (ADAMS et al., 2005b; ADLER et al., 2006; PUTSCHKE, 2007), an revolutionary cognition was proposed in the topology studies of hydrodynamics using two particle correlation analysis (TAKAHASHI et al., 2009). In that work, the near-side and away-side structures of two-particle correlation is reproduced through event-by-event hydrodynamic expansion of the IC hot spots, and without considering jet. That is to say, there are no jets in these events, two-particle correlation is attributed to the signals from specific physical mechanisms and the collective flow result from anisotropies of initial geometry. What's more, the fluctuating non-uniform initial condition plays a vital role in this process. To understand the specific physical mechanisms, a series of studies of two-particle correlation based on peripheral tube model have been done (HAMA et al., 2011; ANDRADE et al., 2011b; HAMA et al., 2013; QIAN et al., 2013).

The peripheral tube model (ANDRADE et al., 2010a; HAMA et al., 2009; ANDRADE et al., 2012; HAMA et al., 2013) provides a straightforward and reasonable picture for the two-particle correlations. It is an approach within the general event-by-event hydrodynamic scheme. The model views the fluctuations in the IC as consisting of independent high energy tubes close to the surface of the system, where the location of each tube is random. Thereby, each tube affects the hydrodynamical evolution of the system independently, and their contributions are summed up linearly to the resultant two-particle correlations. In this approach, one substitutes the complex bulk of the hot matter by an average distribution over many events from the same centrality class.

The above picture attempts to interpret the physical content of fluctuating IC regarding the granularity represented by peripheral high energy tubes. To be specific, if a tube located deep inside the hot matter, the effect of its hydrodynamic expansion would be quickly absorbed by its surroundings, causing relatively less inhomogeneity in the medium. On the contrary, a tube staying close to the surface leads to a significant disturbance to the one-particle distribution, resulting in an azimuthal two-particle correlation structure similar in shape and magnitude to the observed data.

By numerical simulations, as shown in Fig. 7, one finds that the fluid is deflected to both sides of the tube, causing two peaks separated by ~ 120 degrees in the one-particle azimuthal distribution. Subsequently, this leads to the desired two-particle distribution where a double peak is formed on the away side, whose height is approximately half of the single peak located on the near side. It is shown that the resultant correlation structure is robust against the variation of the model parameters (ANDRADE et al., 2010a; ANDRADE et al., 2012). Furthermore, simulations carried out with multiple peripheral tubes show very similar features in the corresponding two-particle correlations. Therefore, it is strongly indicated that the two-particle correlations can be seen as a superposition of those contributions due to individual peripheral tubes.

We note that it is meaningful to compare the present model to another approach frequently employed in the literature, where the one-particle distribution are decomposed into different flow har-

monics. Subsequently, the collective flow related to the harmonic coefficients are understood to be mostly independent and associated with the corresponding eccentricity components in the IC. In other words, v_2 is related to ε_2 , v_3 is related to ε_3 , v_2 and v_3 are independent. Generally, the hydrodynamic evolution linearly transforms the initial state geometric inhomogeneity into the final state anisotropy in momentum space. The difference in our present model is that the effect is considered as local, as a result of how the expansion is affected by a high energy tube close to the surface of the fluid. Therefore, it is irrelevant to the fluid dynamics of the rest of the system, but localized to a specific azimuthal angle ϕ_{tube} associated to the peripheral tube in question. As hydrodynamics is understood as an effective theory at the long wavelength limit, the peripheral tube interprets the two-particle correlation in terms of phenomena where the characteristic length is comparable to the system size. Concerning harmonic coefficients, the event planes of the elliptic and triangular flow coefficients which generated by the tube are therefore both correlated to the location of the tube ϕ_{tube} . However, as one carries out the event-by-event average, ϕ_{tube} is averaged out, and the resultant expression (for instance, see Eqs.(7) and (8) below) does not explicitly depend on it.

This chapter is organized as follows. In section 4.1, we briefly review the peripheral tube model and discuss its main results on the observed two-particle correlations. Subsequently, in section 4.2, we show that the experimental data can be reasonably reproduced by appropriately constructing the IC with the peripheral tube. Furthermore, in section 4.3, we extract the model parameters using event-by-event simulations with various devised IC reflecting the average background and event-by-event fluctuations. It is shown that those extracted values are indeed in accordance with the observed two-particle correlation data. The last section we discuss the case of multi-tube model.

4.1 THE ANALYTICAL PERIPHERAL TUBE MODEL FOR TWO-PARTICLE CORRELATIONS

The peripheral tube model is based on the assumption that the “ridge” and “shoulder” structures of two-particle correlations in nuclear collisions consist of two contributions. The first part is due to the average almond shape energy distribution of the IC, which generates the dominant part of the resultant collective flow. It is treated as the background flow in our approach. Owing to the multiplicity fluctuations, the contributions from the proper events does not cancel out with those from the mixed event, and the residual is proportional to the standard deviation of the multiplicities. The second contribution comes from that of a peripheral tube. In terms of the language of flow harmonic coefficients, it produces aligned elliptic and triangular flow. The above picture can be used to explain the event plane dependence as well as centrality dependence of the observed two-particle correlations (QIAN et al., 2013; CASTILHO et al., 2017). To be specific, we assume that the two-particle correlations is entirely determined by the one-particle distribution. Instead of writing the latter down directly in terms of Fourier expansion (BORGHINI; DINH; OLLITRAULT, 2001), we write down the one-particle distribution as a sum of two terms, namely, the distribution of the background and that of the tube.

$$\frac{dN}{d\phi}(\phi, \phi_{\text{tube}}) = \frac{dN_{\text{bgd}}}{d\phi}(\phi) + \frac{dN_{\text{tube}}}{d\phi}(\phi, \phi_{\text{tube}}), \quad (1)$$

where

$$\frac{dN_{\text{bgd}}}{d\phi}(\phi) = \frac{N_{\text{bgd}}}{2\pi}(1 + 2v_2^{\text{bgd}} \cos(2\phi)), \quad (2)$$

$$\frac{dN_{\text{tube}}}{d\phi}(\phi, \phi_{\text{tube}}) = \frac{N_{\text{tube}}}{2\pi} \sum_{n=2,3} 2v_n^{\text{tube}} \cos(n[\phi - \phi_{\text{tube}}]). \quad (3)$$

In Eq.(2) we consider the most simple case for the background flow, by parametrizing it with the elliptic flow parameter v_2^{bgd} and the overall multiplicity, denoted by N_{bgd} . The contributions from the tube are measured with respect to its angular position ϕ_{tube} , and a minimal number of Fourier components are introduced to reproduce the desired two-particle correlations (ANDRADE et al., 2012), that is to say, only v_2^{tube} and v_3^{tube} caused by the random distribution of the tubes are retained in Eq.(3). It is worth noting that although both the contributions from the background and the tube are written in Fourier expansion, they are intrinsically independent distributions. In particular, the triangular flow in our model is completely generated by the tube, and since its symmetry axis is correlated to the tube location ϕ_{tube} , the variation of the latter is related to the event-by-event fluctuations. We also assume that the flow components from the background are much more significant than those generated by the tube, Ψ_2 is mainly determined by the elliptic flow of the background v_2^{bgd} .

Following the methods used by the STAR experiment (FENG, 2008; AGAKISHIEV et al., 2010), the subtracted di-hadron correlation is given by

$$\left\langle \frac{dN_{\text{pair}}}{d\Delta\phi}(\phi_s) \right\rangle = \left\langle \frac{dN_{\text{pair}}}{d\Delta\phi}(\phi_s) \right\rangle^{\text{prop}} - \left\langle \frac{dN_{\text{pair}}}{d\Delta\phi}(\phi_s) \right\rangle^{\text{mix}}, \quad (4)$$

where $\phi_s = |\phi_{\text{trigger}} - \Psi_{EP}|$ is the trigger angle ($\phi_s = 0$ for in-plane and $\phi_s = \pi/2$ for out-of-plane trigger), and superscripts “*prop*” and “*mix*” respectively indicate that the particle-pair is constructed by using particles from same event and different events. By using Eq.(3), one finds the proper two-particle correlations

$$\left\langle \frac{dN_{\text{pair}}}{d\Delta\phi} \right\rangle^{\text{prop}} = \int f(\phi_{\text{tube}}) \frac{dN^T}{d\phi}(\phi_s, \phi_{\text{tube}}) \frac{dN^A}{d\phi}(\phi_s + \Delta\phi, \phi_{\text{tube}}) \frac{d\phi_s}{2\pi} \frac{d\phi_{\text{tube}}}{2\pi}, \quad (5)$$

where $f(\phi_{\text{tube}})$ is the distribution function of the tube, and superscripts “*T*” and “*A*” indicate “trigger” and “associated” particles respectively (c.f. subscripts “*T*” are shorthands for “transverse”). For simplicity, we take $f(\phi_{\text{tube}}) = 1$.

The combinatorial background $\langle dN_{\text{pair}}/d\Delta\phi \rangle^{\text{mix}}$ can be calculated by using either cumulant or ZYAM method (AJITANAND et al., 2005). Though both methods yield very similar results in our model, it is more illustrative to evaluate the cumulant. Following similar arguments presented in

Ref. (QIAN et al., 2013),

$$\begin{aligned} \left\langle \frac{dN_{\text{pair}}}{d\Delta\phi} \right\rangle^{\text{mixed(cmlt)}} &= \int f(\phi_{\text{tube}}) \int f(\phi'_{\text{tube}}) \frac{dN^T}{d\phi}(\phi_s, \phi_{\text{tube}}) \frac{dN^A}{d\phi}(\phi_s + \Delta\phi, \phi'_{\text{tube}}) \\ &\times \frac{d\phi'_{\text{tube}}}{2\pi} \frac{d\phi_s}{2\pi} \frac{d\phi_{\text{tube}}}{2\pi}, \end{aligned} \quad (6)$$

it is straightforward to show that the resultant correlation reads

$$\begin{aligned} \left\langle \frac{dN_{\text{pair}}}{d\Delta\phi}(\phi_s) \right\rangle^{\text{(cmlt)}} &= \frac{\langle N_{\text{bgd}}^T N_{\text{bgd}}^A \rangle - \langle N_{\text{bgd}}^T \rangle \langle N_{\text{bgd}}^A \rangle}{(2\pi)^2} \\ &\times (1 + 2v_2^{\text{bgd},T} \cos(2\phi_s))(1 + 2v_2^{\text{bgd},A} \cos(2(\Delta\phi + \phi_s))) \\ &+ \frac{\langle N_{\text{tube}}^T N_{\text{tube}}^A \rangle}{(2\pi)^2} \sum_{n=2,3} 2v_n^{\text{tube},T} v_n^{\text{tube},A} \cos(n\Delta\phi). \end{aligned} \quad (7)$$

where the event average is carried out by integration in ϕ_{tube} . The above expression explicitly depends on ϕ_s , which can be used to study the event plane dependence of the correlation. In particular, the trigonometric dependence of the background contribution on ϕ_s indicates that its contribution to the out-of-plane triggers is opposite to that for the in-plane ones. As a result, for the out-of-plane correlation, it leads to an overall suppression in the amplitude, as well as forms a double peak structure on the away side. Indeed, experimental data (FENG, 2008; AGAKISHIEV et al., 2010) shows that the overall correlation decreases while the away-side correlation evolves from a single peak to a double peak as ϕ_s increases. Since these observed features are in agreement with the analytically derived results, the peripheral model is shown to be meaningful despite its simplicity.

By further averaging out ϕ_s , one obtains

$$\begin{aligned} \left\langle \frac{dN_{\text{pair}}}{d\Delta\phi} \right\rangle^{\text{(cmlt)}} &= \frac{1}{2\pi} \int_0^{2\pi} \left\langle \frac{dN_{\text{pair}}}{d\Delta\phi}(\phi_s) \right\rangle^{\text{(cmlt)}} d\phi_s \\ &= \frac{\langle N_{\text{bgd}}^T N_{\text{bgd}}^A \rangle - \langle N_{\text{bgd}}^T \rangle \langle N_{\text{bgd}}^A \rangle}{(2\pi)^2} (1 + 2v_2^{\text{bgd},T} v_2^{\text{bgd},A} \cos(2\Delta\phi)) \\ &+ \frac{\langle N_{\text{tube}}^T N_{\text{tube}}^A \rangle}{(2\pi)^2} \sum_{n=2,3} 2v_n^{\text{tube},T} v_n^{\text{tube},A} \cos(n\Delta\phi). \end{aligned} \quad (8)$$

If the model is indeed realistic, one should be able to obtain the parameters in Eq.(8) according to their respective physical content, while the resulting correlations should be still quantitatively in agreement with the data. This is the principal object of the present work. In what follows, by carrying out numerical simulations, we first show that an appropriately constructed IC can reasonably reproduce the observed data. Furthermore, we attempt to calculate the model parameters according to their definitions. This is done by using various IC tailored to match the respective physical properties of IC in question. In particular, we study the multiplicity fluctuations as well as the flow harmonics of different IC associated with the background as well as the peripheral tube. The two-particle correlations are then evaluated by using the obtained values.

4.2 PARAMETERS AND HYDRODYNAMIC SIMULATION RESULTS OF ONE-TUBE MODEL

In this section, we will employ the one-tube model to do simulations, we focus on mid-central 200 AGeV Au+Au collisions. At first, we devise the IC according to the peripheral tube model. Then, by means of SPheRIO code to observe the temporal evolution of IC, to learn about how the tube leads to the ridge structures in a visible way. After that, we evaluate the two-particle correlations and compare with experimental data, to analyze the rationality of hydrodynamic results in this IC.

To determine the background energy distribution, we average over the 343 events generated by a microscopic event generator, NeXuS (DRESCHER et al., 2001), for the centrality window 20%-40% as shown in Fig. 6. Then we parametrize the obtained almond shaped energy distribution in the $x - y$ plane, which can be fitted by the following parametrization

$$\epsilon_{bgd0} = (9.33 + 7r^2 + 2r^4)e^{-r^{1.8}}, \quad (9)$$

with

$$r = \sqrt{0.41x^2 + 0.186y^2}.$$

Considering the multiplicity fluctuations, we let background energy density distribution fluctuates as follow

$$\epsilon_{bgd} = \epsilon_{bgd0} + \epsilon_{bgd0} * G, \quad (10)$$

where G is a Gaussian distribution function. The influence of multiplicity fluctuations on two-particle correlations can be find in Fig. 8.

The profile of the high energy tube which will be embedded into the background obtained above is parameterized as follows

$$\epsilon_{tube} = 12e^{-(x-x_{tube})^2 - (y-y_{tube})^2}, \quad (11)$$

where the tube is located at a given value of energy density close to the surface, determined by a free parameter r_{tube} , so that its coordinates on the transverse plane read

$$\begin{aligned} x_{tube} &= \frac{r_{tube} \cos \theta}{\sqrt{0.41 \cos^2 \theta + 0.186 \sin^2 \theta}} \\ y_{tube} &= \frac{r_{tube} \sin \theta}{\sqrt{0.41 \cos^2 \theta + 0.186 \sin^2 \theta}}. \end{aligned} \quad (12)$$

Here r_{tube} is used as a free parameter whose value is chosen to be 2.3 in following calculations, and the azimuthal angle of the tube θ is randomized among different events.

By combining the two pieces together, the IC for the present model read

$$\epsilon = \epsilon_{bgd} + \epsilon_{tube}, \quad (13)$$

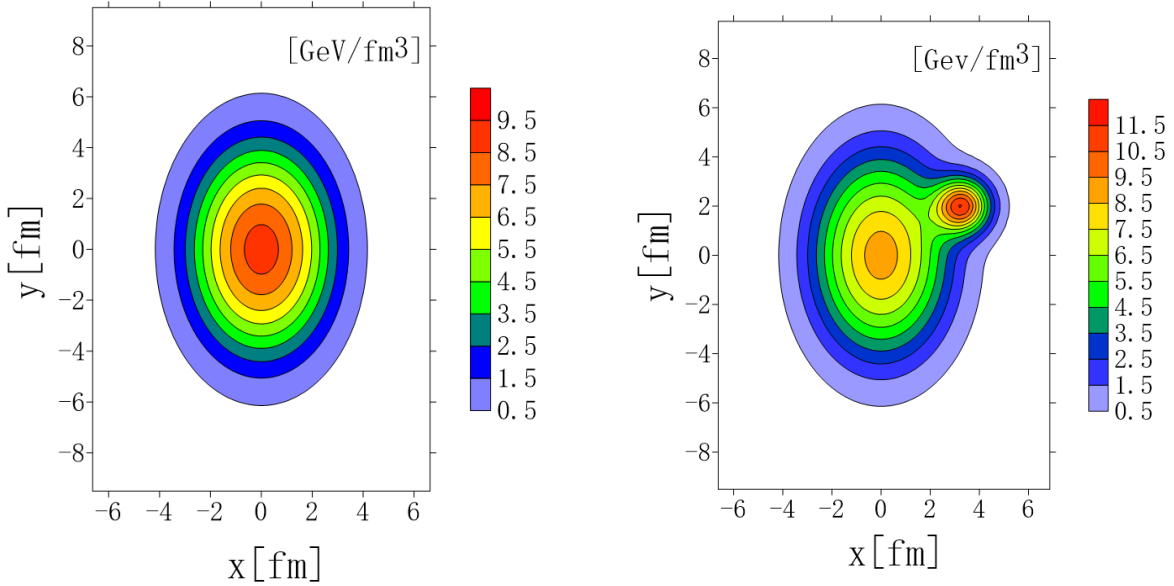


Fig. 6 – (Color online) Left: the background energy distribution obtained by averaging over many NeXuS events. Right: one random event with a high energy peripheral tube sits on top of the background. The parametrization of the IC is discussed in the text.

and the sample graph of IC with one tube is shown in Fig. 6.

Subsequently, we carry out hydrodynamical simulations by using the SPheRIO code. We generate a total of 2000 events by using the IC profile discussed above, in which the location of tube varies from event to event. It is considered to be the fluctuations of IC in event-by-event basis, and the hydrodynamical simulation is carried out for each event. At the end of hydrodynamical evolution, a Monte-Carlo generator is evoked 200 times for hadronization in order to further increase the statistics.

The temporal evolution of IC with one tube on the transverse plane is shown in Fig. 7. From which, one finds that the fluid is deflected to both sides of the tube, causing two peaks separated by ~ 120 in the one-particle azimuthal distribution. As a result, the desired two-particle distribution with a double-peak on the away side will be formed.

In Fig. 8, we studied the effects of multiplicity fluctuation on two-particle correlations, it shows that the multiplicity fluctuation has a significant impact on the integral of two particle correlation distribution. The following results all take into account the multiplicity fluctuation. The resultant two-particle correlations, evaluated by cumulant method and ZYAM method, are shown in Fig. 9, in comparison with the PHENIX data (ADARE et al., 2008). As the hydrodynamic simulations are two-dimension, the obtained correlations are multiplied by a factor related to the longitudinal scaling of the system. From Fig. 9, we find that there are indeed two symmetrical peaks in the resultant flow, and the single peak located on the near side is higher than the height of double-peak. What's more, the results are consistent with PHENIX data, no matter in cumulant method or ZYAM method. It shows that the interpretation of one-tube model and the resultant two-particle correlations are self-consistent.

At the same time, we present the overall elliptic flow, v_2^{all} in Table 1, which is also evaluated from hydrodynamical simulations considered event-by-event fluctuating IC consisting of the background and tube. By comparing the value against the data of 20%-60% Au+Au collisions obtained by PHENIX (AFANASIEV et al., 2009), as in APPENDIX C Table 8, we can find the simulation result

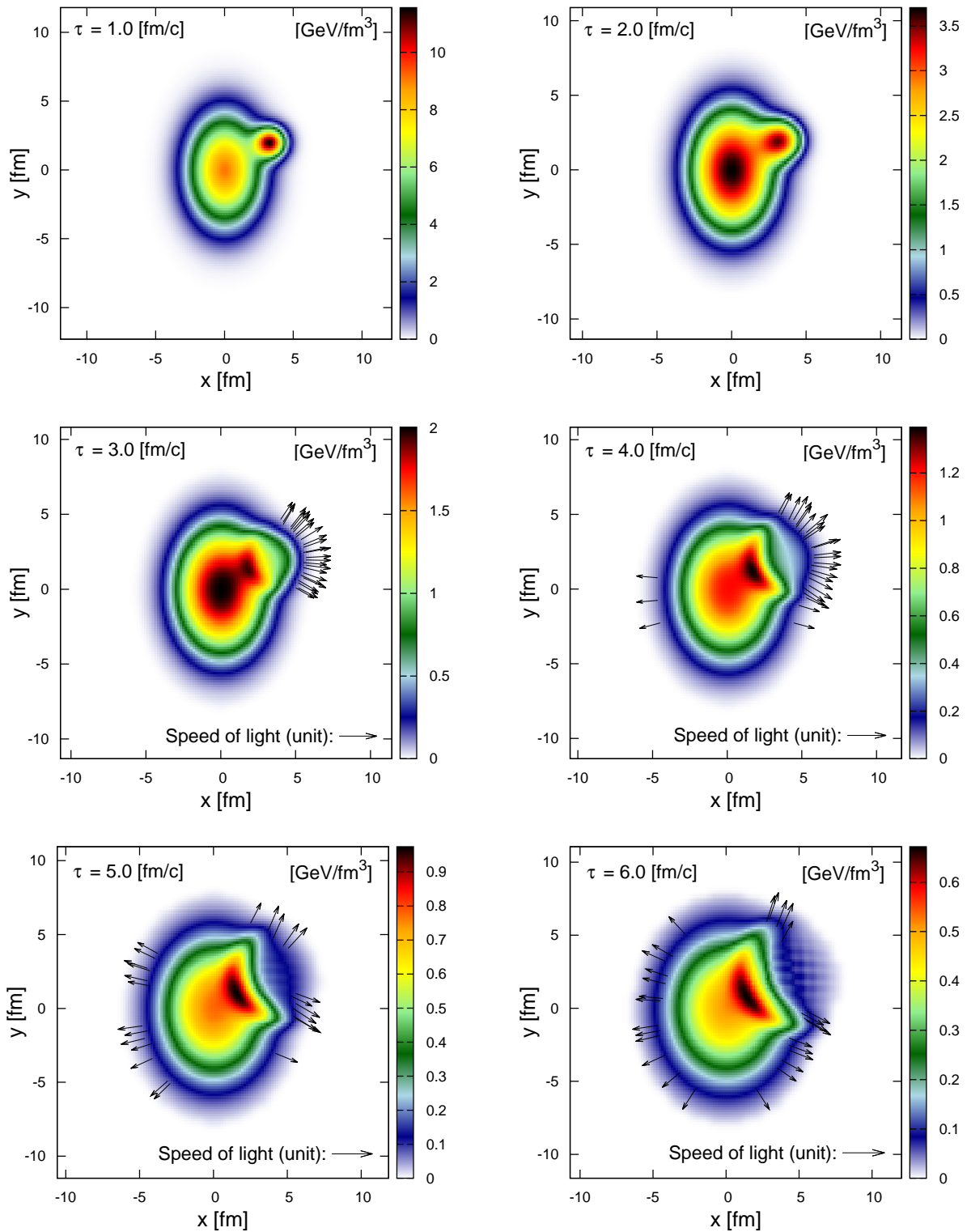


Fig. 7 – (Color online) The temporal evolution of the IC consisting of one peripheral tube placed on top of an elliptic smoothed background energy distribution. The parameters for the IC used in calculation are discussed in section III.

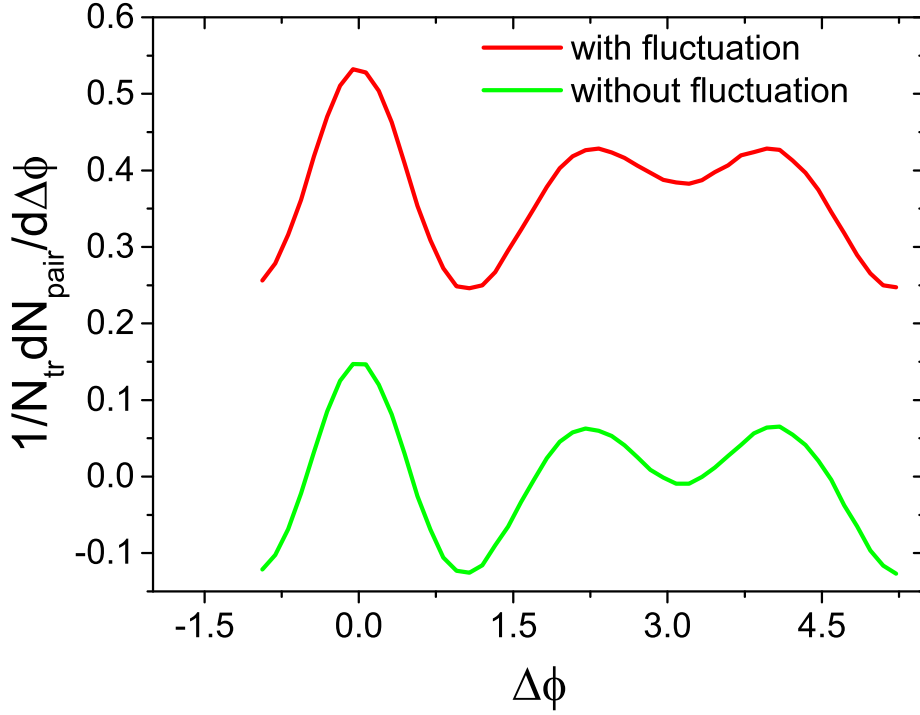


Fig. 8 – (Color online) The influence of fluctuation of multiplicity on two-particle correlations in one tube model. The results are calculated by using cumulant method. Where the red line is for background Eq.(10) with fluctuation which controlled by a Gaussian function G centered at 0 and standard deviation $\sigma = 0.18$, the green line is for background Eq.(9) without fluctuation. The momentum intervals are $0.4 < p_T^A < 1$ Gev and $2 < p_T^T < 3$ Gev.

is consistent with the collisions of the same centrality window.

Table 1 – The calculated background as well as overall elliptic flow coefficients for corresponding transverse momentum intervals of trigger and associated particles. The calculations are carried out by using IC as described in the text.

	$0.4 < p_T < 1$	$1 < p_T < 2$	$2 < p_T < 3$
v_2^{bgd}	0.11	0.21	0.36
v_2^{all}	0.09	0.17	0.26

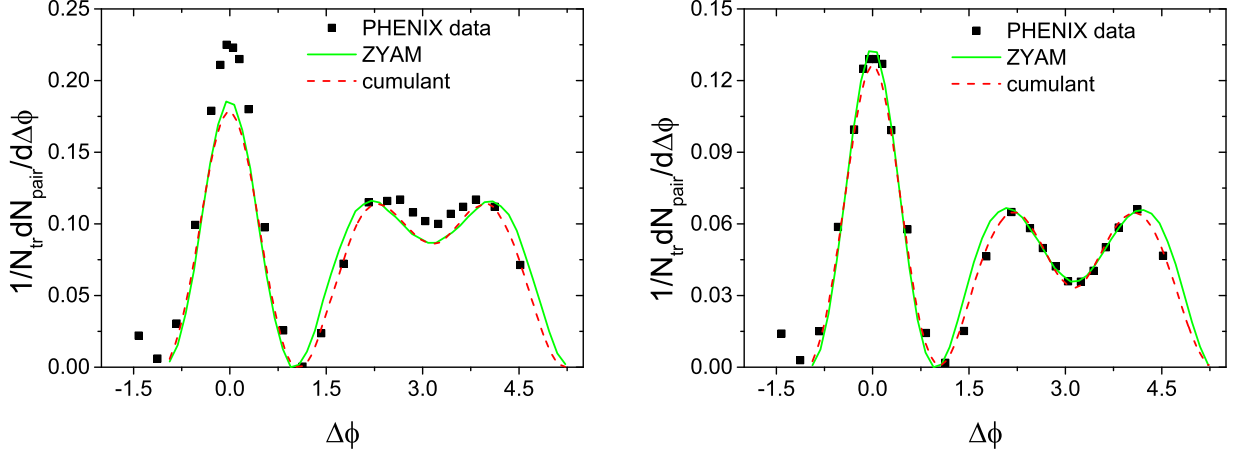


Fig. 9 – (Color online) The di-hadron correlations obtained in SPheRIO simulations, comparing with PHENIX data. Where the red line is calculated by using cumulant method and green line is calculated by using ZYAM method. Left: di-hadron correlations for the momentum intervals $0.4 < p_T^A < 1$ Gev and $2 < p_T^T < 3$ Gev; Right: di-hadron correlations for the momentum intervals $1 < p_T^A < 2$ Gev and $2 < p_T^T < 3$ Gev.

4.3 PARAMETERS EXTRACTED FROM SIMULATION RESULTS

Now, it is interesting to verify that the parameters given in Eq.(8) are indeed quantitatively meaningful. To achieve this, we extract the model parameters in Eq.(8) using mostly the same arguments leading to very expression. On the one hand, the background flow coefficients v_2^{bgd} can be obtained directly by investigating the hydrodynamic evolution of IC solely determined by ϵ_{bgd} . A total of 2000 events with 200 Monte Carlo each are considered in the evaluation, the obtained values are summarized in Table 1.

On the other hand, however, some of the parameters can also be inferred straightforwardly from the experimental data or SPheRIO results. Here, we estimate those from SPheRIO simulation results. To estimate the multiplicity fluctuations of the background, $\langle N_{\text{bgd}}^T N_{\text{bgd}}^A \rangle - \langle N_{\text{bgd}}^T \rangle \langle N_{\text{bgd}}^A \rangle$, we count, on an event-by-event basis, the number of particles of corresponding momentum intervals. The events in question are those generated by NeXuS of 20% - 40% centrality window, and we made use of a total of 1000 events. By using Fourier expansion of the two particle correlation, and extracting the second and third order coefficients,

$$a_2 = \frac{\langle N_{\text{bgd}}^T N_{\text{bgd}}^A \rangle - \langle N_{\text{bgd}}^T \rangle \langle N_{\text{bgd}}^A \rangle}{(2\pi)^2} 2v_2^{\text{bgd},T} v_2^{\text{bgd},A} + \frac{\langle N_{\text{tube}}^T N_{\text{tube}}^A \rangle}{(2\pi)^2} 2v_2^{\text{tube},T} v_2^{\text{tube},A}, \quad (14)$$

$$a_3 = \frac{\langle N_{\text{tube}}^T N_{\text{tube}}^A \rangle}{(2\pi)^2} 2v_3^{\text{tube},T} v_3^{\text{tube},A}, \quad (15)$$

where $v_2^{\text{bgd},T}$ and $v_2^{\text{bgd},A}$ is calculated from the elliptic background in tube model (as Table 1), then we obtained the multiplicity fluctuations estimated from simulations, and the parameters related to $v_2^{\text{tube},T}$, $v_2^{\text{tube},A}$, $v_3^{\text{tube},T}$, and $v_3^{\text{tube},A}$, as follows,

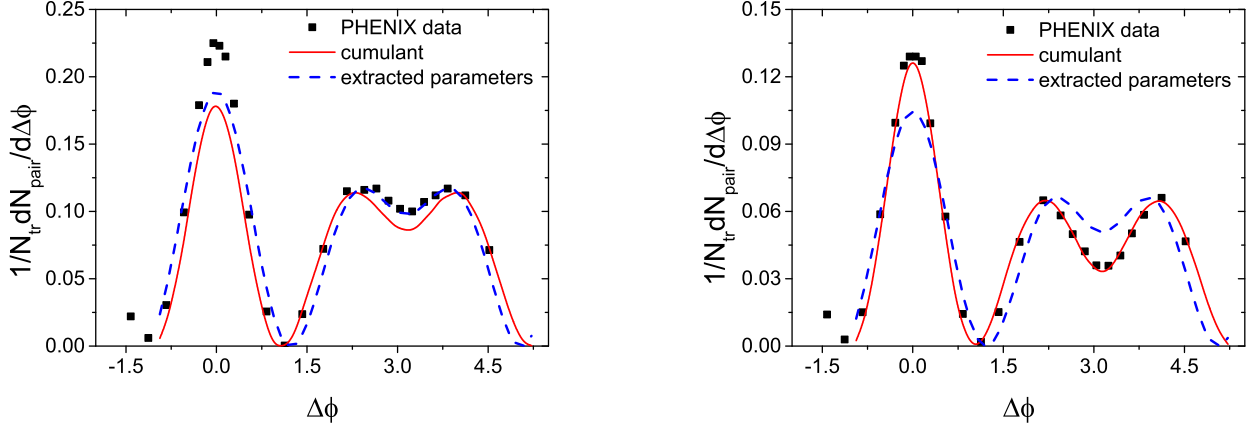


Fig. 10 – (Color online) The calculated two-particle correlations by using one-tube IC for 20% – 40% centrality window in comparison with the corresponding data by PHENIX Collaboration (ADARE et al., 2008), and those obtained by using the extracted parameters in Table 1 and Eqs.(16) and (17). The SPheRIO results from using cumulant method are shown in red solid curves, the data are shown in solid squares, and those obtained by the estimated parameters are shown by the blue dashed curves. Left: the results for the momentum intervals $0.4 < p_T^A < 1$ GeV and $2 < p_T^T < 3$ GeV. Right: those for the momentum intervals $1 < p_T^A < 2$ GeV and $2 < p_T^T < 3$ GeV.

$$\begin{aligned}
 \langle N_{\text{bgd}}^T N_{\text{bgd}}^A \rangle - \langle N_{\text{bgd}}^T \rangle \langle N_{\text{bgd}}^A \rangle &= 14.67, \\
 \langle N_{\text{tube}}^T N_{\text{tube}}^A \rangle v_2^{\text{tube},T} v_2^{\text{tube},A} &= 1.62, \\
 \langle N_{\text{tube}}^T N_{\text{tube}}^A \rangle v_3^{\text{tube},T} v_3^{\text{tube},A} &= 1.63,
 \end{aligned} \tag{16}$$

for $0.4 < p_T^A < 1$, $2 < p_T^T < 3$, and

$$\begin{aligned}
 \langle N_{\text{bgd}}^T N_{\text{bgd}}^A \rangle - \langle N_{\text{bgd}}^T \rangle \langle N_{\text{bgd}}^A \rangle &= 5.07, \\
 \langle N_{\text{tube}}^T N_{\text{tube}}^A \rangle v_2^{\text{tube},T} v_2^{\text{tube},A} &= 1.36, \\
 \langle N_{\text{tube}}^T N_{\text{tube}}^A \rangle v_3^{\text{tube},T} v_3^{\text{tube},A} &= 1.48,
 \end{aligned} \tag{17}$$

for $1 < p_T^A < 2$, $2 < p_T^T < 3$ respectively.

Finally, by substituting the above parameters back into Eq.(8), one obtains the two-particle correlations as also shown in Fig. 10. It is found that the two approaches are in good agreement with each other.

4.4 DISCUSSION ON MULTI-TUBE MODEL

In order to understand the physical mechanism behind the ridge effect of hydrodynamic model in a simple way, in the above, we studied a simple model with only one high energy peripheral tube in anisotropic background, verified the consistency of analytic peripheral tube model. But in realistic situations, it is impossible for the IC to contain only one tube. Therefore, in this section, we will

discuss the IC with several high energy tubes whose location and energy may also fluctuate.

Based on the one-tube model discussed above, we add more tubes on the background, the maximum energy density and size of additional tubes are identical, but the azimuthal angles are random. The corresponding two-particle correlations for IC with 2, 3, 4 tubes are presented in Fig. 11. Since the correlation distribution curves are evaluated from only a few hundred events, they are not very smooth, but enough to observe the impact of number of tubes. As the number of tubes increases, only the peak heights change less, the two-particle correlations maintain the overall shapes with the characteristic triple-ridge structures, which is consistent with the results in Ref.(HAMA et al., 2013). That is to say, simulations carried out with multiple peripheral tubes still show such robust feature of the two-particle correlation structure, which strongly suggests that the emergence of the special structures of two-particle correlations can be naturally interpreted as a superposition of those of independent peripheral tubes.

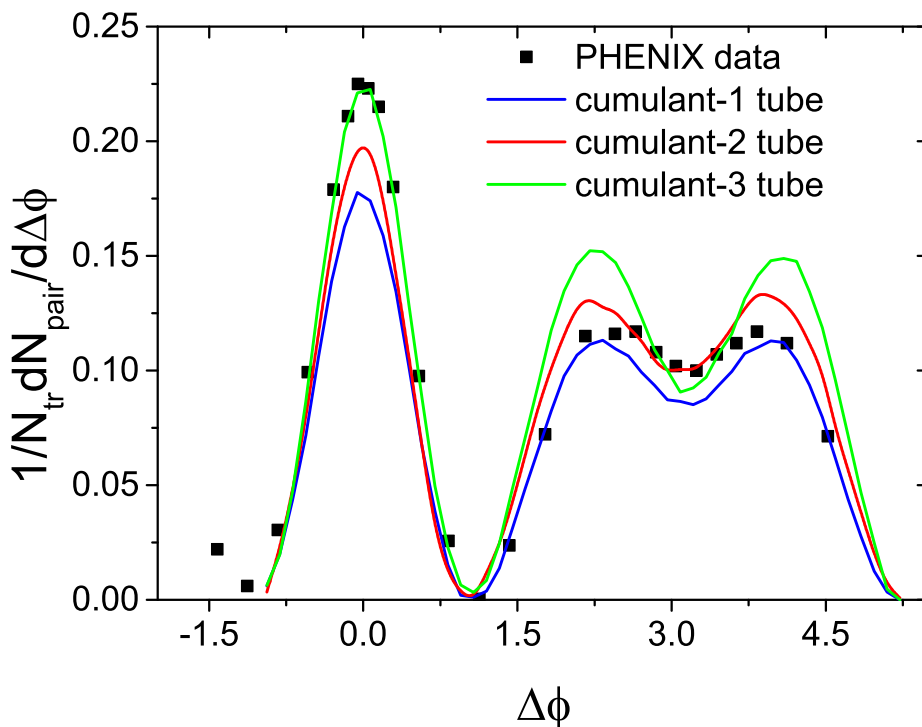


Fig. 11 – (Color online) Two-particle correlations for IC with different number of tubes. The results are calculated by using cumulant method in the momentum intervals $0.4 < p_T^A < 1$ Gev and $2 < p_T^T < 3$ Gev.

The fluctuations in the initial state are explored by studying the v_n , as well as the correlations between event planes of different order. We further investigate the correlation between the event planes of v_2 and v_3 , the distinct feature can serve to discriminate the present model and other approaches. Roughly speaking, from the standard viewpoint, the event planes of different harmonics are mostly uncorrelated, since the fluctuations in eccentricity ε_n are small and random. It is mostly confirmed by the recent measures carried out by ATLAS Collaboration (AAD et al., 2014). In the reference (AAD et al., 2014), for 20%-30% centrality collisions, the distribution of $(\Psi_2 - \Psi_3)$ deviates only

about 0.5% from a completely uncorrelated one. And the centrality dependence of the correlator is evaluated, and it is observed that it further approaches a completely uncorrelated distribution as one goes to most central collisions. At a first glimpse, this is exactly on the contrary of what is proposed in our model. The elliptic and triangular flows from the tube are originated from the same cause, a peripheral high energy tube, and therefore their event planes are correlated. However, there is one subtlety. If one adds two tubes onto anisotropic background and assumes that the resultant distribution is just the superposition of those individual contributions, one observes that the resultant event planes might not behave linearly. This can be seen by assuming that the azimuthal angles of the two tubes are 0 and ϕ_t , the harmonic coefficients are v_n^i with $i = 1, 2$. It is straightforward to find that

$$\Psi_2 = \frac{1}{2} \arctan \frac{v_2^2 \sin 2\phi_t}{v_2^1 + v_2^2 \cos 2\phi_t} \quad (18)$$

$$\Psi_3 = \frac{1}{3} \arctan \frac{v_3^2 \sin 3\phi_t}{v_3^1 + v_3^2 \cos 3\phi_t}. \quad (19)$$

Thus in general $\Psi_2 \neq \Psi_3$ if the harmonic coefficients of the two tubes are not exactly identical.

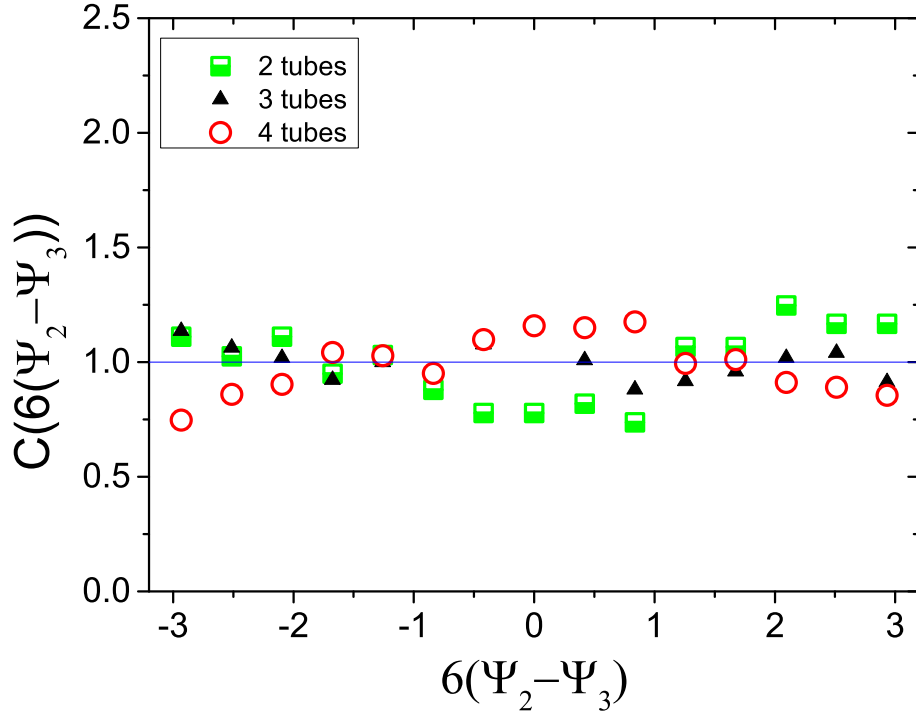


Fig. 12 – (Color online) The relative angle distributions calculated by using IC with different number of tubes, where each curve is obtained by using 3000 events.

It is worthwhile to verify whether the IC with multiple numbers of tubes will lead to the overall event planes Ψ_2 and Ψ_3 correlations in the simulation. Following the definition of correlation function in (AAD et al., 2014), we can evaluate the two-plane relative angle distributions by dividing the

foreground by the background, as follows,

$$C(k(\Psi_n - \Psi_m)) = \frac{S(k(\Psi_n - \Psi_m))}{B(k(\Psi_n - \Psi_m))}. \quad (20)$$

where the background distributions B is calculated by combining event plane angles from different events, while the foreground distributions S is calculated by combining event plane angles from the same events, and both of the distributions are normalized to one. Then, we obtain the results in Fig. 12 and Fig. 13, they are in accordance with that in Ref.(AAD et al., 2014). As shown in Fig. 13, the relative angle distribution approaches to that of random distribution as the number of events increases. The results for ICs with two, three and four high-energy tubes shows that event planes are uncorrelated. It is consistent with previous findings in Ref. (HAMA et al., 2013), where the background is assumed to be isotropic, and the tubes are identical. This indicates that the tube model is consistent with the observed event plane correlation.

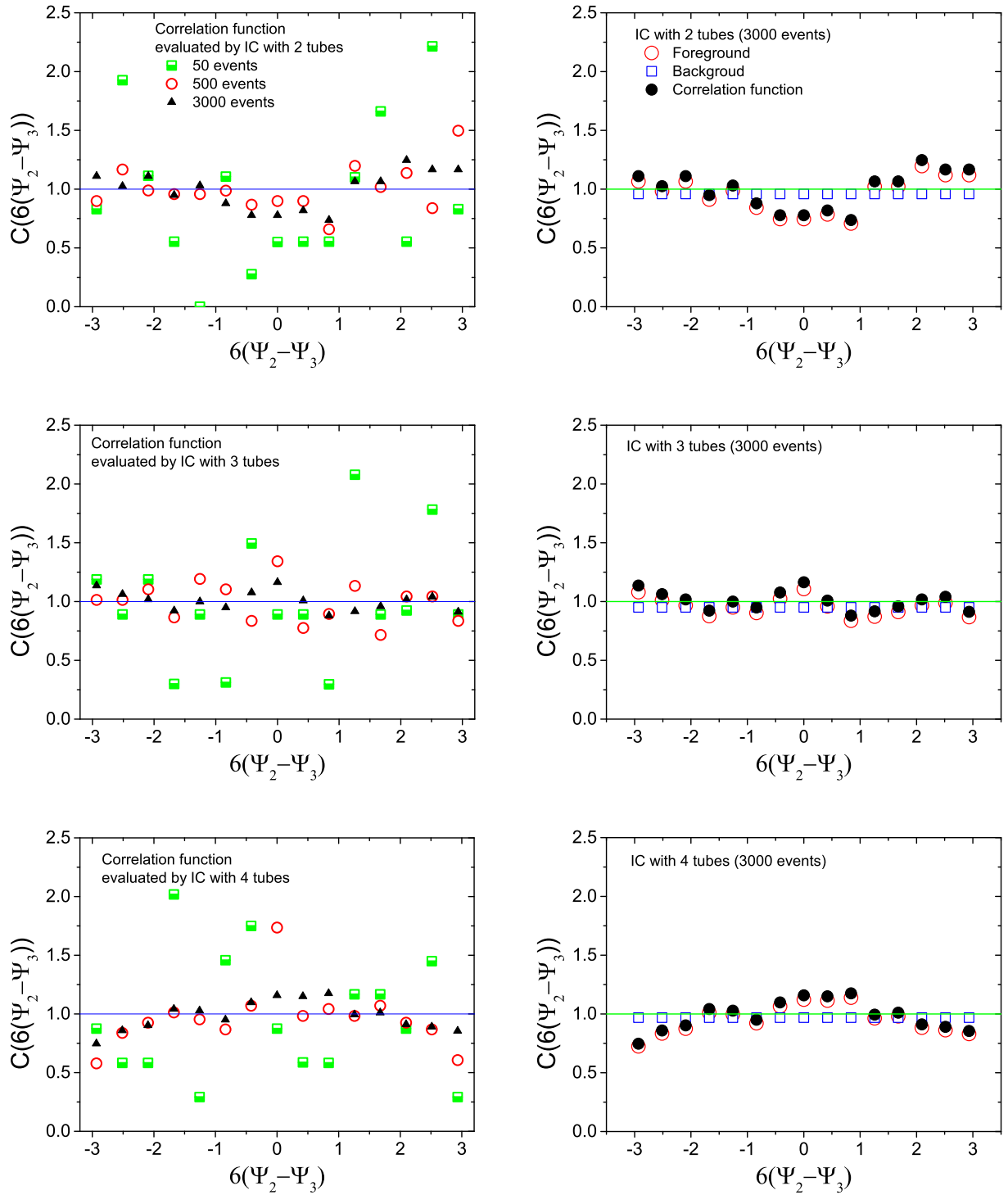


Fig. 13 – (Color online) The relative angle distributions between Ψ_2 and Ψ_3 in tube model. Left column: the results evaluated by using different numbers of IC with three high energy tubes; Right column: the relative angle distribution (filled black circles) evaluated by the ratio of foreground (red empty circles) to the background (blue empty squares) signals.

5 ANISOTROPIC GAUSSIAN MODEL AND PERIPHERAL TUBE MODEL

The methods for decomposition of the IC and flow harmonics have been extensively employed to explore relevant information regarding the collectivity of the system. However, due to the nonlinearity of hydrodynamics, to what degree the mapping between IC and flow harmonics can be established quantitatively and therefore captured by the proposed methods is still not entirely settled. Also, from the AdS/CFT viewpoint, hydrodynamics stands on the other side where the system is strongly interacting with intricate correlations, while according to the duality, the linear response theory is valid only for its dual gravity theory. That is because the dual gravity theory is a weak coupling theory, and the linear response theory is a perturbation theory under weak coupling. In this context, it is meaningful also to investigate some alternative approaches regarding the description of IC and its subsequent effect on collective phenomena, such as the Bessel-Fourier expansion.

The peripheral tube model (ANDRADE et al., 2010a; HAMA et al., 2009) discussed above provides an intuitive explanation for the generation of the triangular flow and two-particle correlations. The model can also be viewed as an alternative approach in the context of event-by-event hydrodynamics. The IC is divided into background and fluctuations. The former is obtained by averaging the distribution over many events from the same centrality class. While for the latter, the IC fluctuations are understood as consisting of independent high energy spot located close to the surface of the system, referred to as peripheral tubes due to its longitudinal extension. The resultant higher-order harmonics are attributed to how a peripheral tube affects the hydrodynamical evolution of the system locally. The overall contributions are obtained by the superposition of those of individual tubes.

The essential feature of our model is that the above picture attempts to interpret the IC fluctuations in terms of the localized ones, instead of the global sinusoidal expansion regarding moments. To be specific, if a tube is located deep inside the hot matter, which might, however, contribute significantly to the moment expansion, is less relevant in our approach. To the best of our knowledge, the effect of its hydrodynamic expansion would be mostly suppressed by its surroundings, causing less significant consequence in the medium. This is contrary to a tube staying close to the surface, which might cause significant disturbance to the one-particle azimuthal distribution, as well as the related two-particle correlations. The model has been employed to study various features of the observed two-particle correlations in comparison with data (ANDRADE et al., 2010a; HAMA et al., 2009; ANDRADE et al., 2012; HAMA et al., 2013; WEN et al., 2019).

In this context, the present study is motivated to carry out a closer comparison between the IC of the peripheral tube model and those related to moment decomposition. The primary strategy is to prepare two sets of event-by-event fluctuating IC with mostly identical eccentricity distributions and then investigate the subsequent linear as well as nonlinear hydrodynamic response and the resultant flow harmonics. Although similar in terms of its Fourier components, the IC in question are visually distinct by construction. By employed most of the methods of IC and flow analysis mentioned above, we evaluated various relevant observables. Substantial differences between the two models are presented and discussed. Furthermore, the implications of the present findings are addressed.

This chapter is organized as follows. In the next section, we briefly review the peripheral tube model and devise an anisotropic Gaussian model which primarily consists of moments of Fourier decompositions. The latter is mostly Gaussian in the radial direction, and in the azimuthal direction, it is parameterized to contain different harmonic orders. Subsequently, in section 5.2, we explain how the parameter of the anisotropic Gaussian IC are adjusted so that it gives largely identical eccentricity distributions to those of the peripheral tube model. Both models are then fed to the hydrodynamic code SPheRIO. The calculations are carried out for flow harmonics and their probability distributions, symmetric cumulant, mixed harmonics, as well as nonlinear response coefficients.

5.1 BRIEF DESCRIPTION OF MODELS

In this section, I will first give a brief description of the peripheral tube model and anisotropic Gaussian model. In the peripheral tube model, event-by-event fluctuating ICs are generated by placing three random tubes on the background. For the anisotropic Gaussian model, the event-by-event fluctuations can be implemented by adjusting the model parameters C_n and θ_n to take random values. In essence, these two models provide very different initial conditions.

Then we discuss the effects of anisotropic Gaussian model parameters through the simulations of Au+Au collision at 200Gev. That is, by adjusting the parameters of the anisotropic Gaussian model, we obtain a $\varepsilon_n - v_n$ distribution similar to the tube model, as well as a similar two-particle correlation distribution curve. It implies that, even though the IC are quite distinct, if one appropriately choose the model parameters, the scatter plots as well as two-particle correlations from the two models may look similar. But the probability density distributions of the event-by-event ε_n and v_n in anisotropic Gaussian model is different from the peripheral tube model one.

5.1.1 Peripheral tube model

In previous work (WEN et al., 2019), we studied the two-particle correlations in Au+Au collision at 200Gev by using peripheral tube model. As mentioned above, the IC of the peripheral tube model consist of a smoothed background and a few high energy tubes close to the surface of the system. The background give rise to the averaged bulk properties of the system, while the tubes characterize the event-by-event fluctuations. Subsequently, the energy density profile of the model is given by

$$\epsilon = \epsilon_{\text{bgd}} + \epsilon_{\text{tube}}. \quad (1)$$

Here, the averaged background distribution reads

$$\epsilon_{\text{bgd}} = (K + Lr^2 + Mr^4)e^{-r^{2c}}, \quad (2)$$

with

$$r = \sqrt{ax^2 + by^2}, \quad (3)$$

where the parameters K , L , M , a , b , c are determined by a numerical fit to the averaged IC generated by NeXuS or EPOS (DRESCHER et al., 2002b; DRESCHER et al., 2001; WERNER; LIU; PIEROG, 2006; WERNER; KARPENKO; PIEROG, 2011; WERNER et al., 2014). The profile of a high energy tube is given by

$$\epsilon_{\text{tube}} = A_{\text{tube}} \exp \left[-\frac{(x - x_{\text{tube}})^2 - (y - y_{\text{tube}})^2}{R_{\text{tube}}} \right], \quad (4)$$

with

$$\begin{aligned} r_{\text{tube}} &= \frac{r_0}{\sqrt{a \cos^2 \theta + b \sin^2 \theta}} \\ x_{\text{tube}} &= r_{\text{tube}} \cos(\theta) \\ y_{\text{tube}} &= r_{\text{tube}} \sin(\theta) \end{aligned} \quad (5)$$

where A_{tube} and R_{tube} are the maximum energy and radius of the tube, while r_{tube} give the radial location of the tube, subsequently determined by r_0 , a , b , and θ . The azimuth angle θ is randomly chosen for individual tube.

We found that the peripheral tube model can reproduce the two-particle correlations well for Au+Au collision at 200Gev. We understand it as that due to the local non-uniformity in the initial energy density distribution, that is, the high energy tubes affects the direction of the flow in the hydrodynamic evolution, resulting in two peaks in the azimuth distribution of the single particle, thus forming a special structure of the ridge. In order to study the effects of non-uniformity of the local energy density in peripheral tube model, Prof. Kodama proposed the anisotropic Gaussian model with a local energy density that is very different from that of the tube model.

5.1.2 Anisotropic Gaussian model

The initial energy density distribution in anisotropic Gaussian model is given by

$$\epsilon(r, \theta) = Z e^{-\frac{r^2}{R^2(\theta)}}, \quad (6)$$

$$R(\theta) = R_0 \left[1 + \sum_{n=2} C_n \cos(n(\theta - \theta_n)) \right]^{1/2}, \quad (7)$$

and the total energy can be integrated out by

$$\begin{aligned}
E_T &= \int_0^{2\pi} \int_0^\infty r\epsilon(r, \theta) dr d\theta = \int_0^{2\pi} \int_0^\infty r Z e^{-\frac{r^2}{R^2(\theta)}} dr d\theta \\
&= \frac{Z}{2} \int_0^{2\pi} \int_0^\infty R^2(\theta) e^{-\frac{r^2}{R^2(\theta)}} d\left(\frac{r^2}{R^2(\theta)}\right) d\theta \\
&= \frac{Z}{2} \int_0^{2\pi} R^2(\theta) \int_0^\infty e^{-x^2} dx^2 d\theta, \quad \text{where } x = \frac{r}{R(\theta)} \\
&= \frac{Z}{2} \int_0^{2\pi} R^2(\theta) d\theta \\
&= \frac{Z R_0^2}{2} \int_0^{2\pi} \left[1 + \sum_{n=2} C_n \cos(n(\theta - \theta_n)) \right] d\theta \\
&= Z \pi R_0^2
\end{aligned} \tag{8}$$

Here, for a given azimuthal direction, the radial distribution is essentially Gaussian. The azimuthal dependence of the radius is contained within the specific form of $R(\theta)$. The latter draws a closed curve as one varies the azimuthal angle θ from 0 to 2π . The value of the parameters R_0 and Z are chosen to reproduce the same size and average total energy of the given IC. Also, C_n and θ_n are randomized to reproduce the same eccentricity distribution of the tube model, as will be further discussed below.

According to the definition of eccentricity

$$\epsilon_n = \frac{\sqrt{\langle r^n \cos(n\theta) \rangle^2 + \langle r^n \sin(n\theta) \rangle^2}}{\langle r^n \rangle}, \tag{9}$$

we have following derivations

$$\begin{aligned}
\langle r^m \rangle &= \frac{\int_0^{2\pi} \int_0^\infty r^m r \epsilon(r, \theta) dr d\theta}{\int_0^{2\pi} \int_0^\infty r \epsilon(r, \theta) dr d\theta} = \frac{\int_0^{2\pi} \int_0^\infty r^m r Z e^{-\frac{r^2}{R^2(\theta)}} dr d\theta}{E_T} \\
&= \frac{\int_0^{2\pi} \int_0^\infty r^m \frac{Z R^2(\theta)}{2} e^{-\frac{r^2}{R^2(\theta)}} d\left(\frac{r^2}{R^2(\theta)}\right) d\theta}{E_T} \\
&= \frac{Z}{2 E_T} \int_0^{2\pi} R^{m+2}(\theta) \int_0^\infty x^{m/2} e^{-x} dx d\theta, \quad \text{where } x = \frac{r^2}{R^2(\theta)} \\
&= \frac{Z}{2 E_T} \int_0^{2\pi} R^{m+2}(\theta) \Gamma\left(\frac{m}{2} + 1\right) d\theta \\
&= \frac{R_0^m}{2\pi} \Gamma\left(\frac{m}{2} + 1\right) I_m
\end{aligned} \tag{10}$$

with

$$I_m = \int_0^{2\pi} \left[1 + \sum_{n=2} C_n \cos(n(\theta - \theta_n)) \right]^{\frac{m}{2} + 1} d\theta. \tag{11}$$

$$\begin{aligned}
\langle r^m \cos(m\theta) \rangle &= \frac{\int_0^{2\pi} \int_0^\infty r^m \cos(m\theta) r \epsilon(r, \theta) dr d\theta}{\int_0^{2\pi} \int_0^\infty r \epsilon(r, \theta) dr d\theta} \\
&= \frac{\int_0^{2\pi} \int_0^\infty r^m \cos(m\theta) r Z e^{-\frac{r^2}{R^2(\theta)}} dr d\theta}{E_T} \\
&= \frac{\int_0^{2\pi} \int_0^\infty r^m \cos(m\theta) \frac{ZR^2(\theta)}{2} e^{-\frac{r^2}{R^2(\theta)}} d\left(\frac{r^2}{R^2(\theta)}\right) d\theta}{E_T} \\
&= \frac{Z}{2E_T} \int_0^{2\pi} R^{m+2}(\theta) \cos(m\theta) \int_0^\infty x^{m/2} e^{-x} dx d\theta, \quad \text{where } x = \frac{r^2}{R^2(\theta)} \\
&= \frac{Z}{2E_T} \int_0^{2\pi} R^{m+2}(\theta) \cos(m\theta) \Gamma\left(\frac{m}{2} + 1\right) d\theta \\
&= \frac{R_0^m}{2\pi} \Gamma\left(\frac{m}{2} + 1\right) I_m^C
\end{aligned} \tag{12}$$

with

$$I_m^C = \int_0^{2\pi} \cos(m\theta) \left[1 + \sum_{n=2} C_n \cos(n(\theta - \theta_n)) \right]^{\frac{m}{2}+1} d\theta. \tag{13}$$

$$\begin{aligned}
\langle r^m \sin(m\theta) \rangle &= \frac{\int_0^{2\pi} \int_0^\infty r^m \sin(m\theta) r \epsilon(r, \theta) dr d\theta}{\int_0^{2\pi} \int_0^\infty r \epsilon(r, \theta) dr d\theta} \\
&= \frac{\int_0^{2\pi} \int_0^\infty r^m \sin(m\theta) r Z e^{-\frac{r^2}{R^2(\theta)}} dr d\theta}{E_T} \\
&= \frac{\int_0^{2\pi} \int_0^\infty r^m \sin(m\theta) \frac{ZR^2(\theta)}{2} e^{-\frac{r^2}{R^2(\theta)}} d\left(\frac{r^2}{R^2(\theta)}\right) d\theta}{E_T} \\
&= \frac{Z}{2E_T} \int_0^{2\pi} R^{m+2}(\theta) \sin(m\theta) \int_0^\infty x^{m/2} e^{-x} dx d\theta, \quad \text{where } x = \frac{r^2}{R^2(\theta)} \\
&= \frac{Z}{2E_T} \int_0^{2\pi} R^{m+2}(\theta) \sin(m\theta) \Gamma\left(\frac{m}{2} + 1\right) d\theta \\
&= \frac{R_0^m}{2\pi} \Gamma\left(\frac{m}{2} + 1\right) I_m^S
\end{aligned} \tag{14}$$

with

$$I_m^S = \int_0^{2\pi} \sin(m\theta) \left[1 + \sum_{n=2} C_n \cos(n(\theta - \theta_n)) \right]^{\frac{m}{2}+1} d\theta. \tag{15}$$

Then, the eccentricity can be derived from above equations

$$\varepsilon_n = \frac{\sqrt{(I_m^C)^2 + (I_m^S)^2}}{I_m}, \tag{16}$$

For small angular inhomogeneities, namely, $C_n \ll 1$, one finds the following simplified expressions for the eccentricities

$$\varepsilon_n \sim \frac{n+2}{4} C_n, \quad (17)$$

as shown in Fig. 14 and eccentricity planes

$$\Phi_n \sim \frac{1}{n} \arctan 2 \frac{I_n^S}{I_n^C} + \frac{\pi}{n}. \quad (18)$$

In practice, we adopt Simpson method to numerical integrate the eccentricity in SPheRIO simulation. Fig. 14 shows the eccentricity calculated by using Eqs.(16) and (17).

To learn about the effects of the model parameters, here we study five different sets of choices for the parameters C_n and θ_n . The IC of the anisotropic Gaussian model is specified as follows. According to the range of initial energy density distribution and initial total energy in peripheral tube model whose parameters are given in Chapter4, we can determine the anisotropic Gaussian model parameters $Z = 11.7$, $R_0 = 3$. The parameter C_n of a given event, when it is not vanishing, is chosen according to the positive part of a Gaussian distribution. Here are the parameterization of the Gaussian distribution for the five sets of parameters.

(1) For the set 1

- C_2 is Gaussian distribution centered at 0 with $\sigma = 0.3$,
- C_3 is Gaussian distribution centered at 0 with $\sigma = 0.22$,
- $C_n = 0$, ($n \neq 2, 3$).
- θ_2 uniform distributed in $-\frac{\pi}{2} < \theta_2 < \frac{\pi}{2}$,
- θ_3 uniform distributed in $-\frac{\pi}{3} < \theta_3 < \frac{\pi}{3}$.

For the sets 2, 3, 4, and 5

- C_2 is Gaussian distribution centered at 0 with $\sigma = 0.3$,
- C_3 is Gaussian distribution centered at 0 with $\sigma = 0.22$,
- C_4 is Gaussian distribution centered at 0 with $\sigma = 0.2$,
- C_5 is Gaussian distribution centered at 0 with $\sigma = 0.15$.
- $C_n = 0$, ($n \neq 2, 3, 4, 5$).

And the interval of θ_n are following

(2) For the set 2

$$\theta_2 = 0, \theta_3 = 0, \theta_4 = 0, \theta_5 = 0.$$

(3) For the set 3

- θ_2 uniform distributed in $-\frac{\pi}{4} < \theta_2 < \frac{\pi}{4}$,
- θ_3 uniform distributed in $-\frac{\pi}{6} < \theta_3 < \frac{\pi}{6}$,
- θ_4 uniform distributed in $-\frac{\pi}{8} < \theta_4 < \frac{\pi}{8}$,

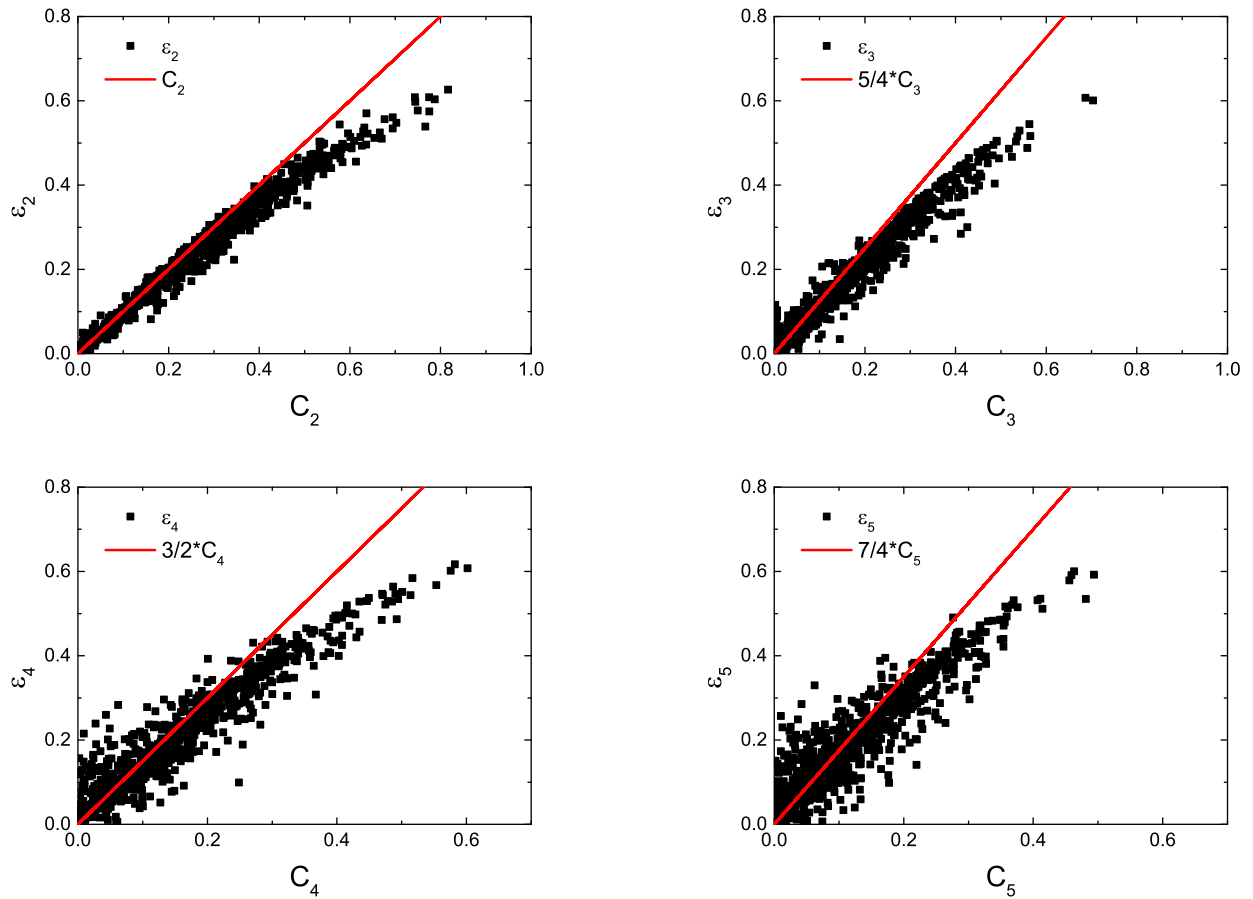


Fig. 14 – (Color online) The relation between model parameters C_n and eccentricity ε_n . Scatters are the results of Eq.(16), determined by a series of random values of C_2 , C_3 , C_4 , C_5 in set 4, and θ_n uniform distributed in $-\frac{\pi}{n} < \theta_n < \frac{\pi}{n}$ for $(n = 2, 3, 4, 5)$. Solid lines are the results of Eq.(17).

θ_5 uniform distributed in $-\frac{\pi}{10} < \theta_5 < \frac{\pi}{10}$.

(4) For the set 4

θ_2 uniform distributed in $-\frac{\pi}{2} < \theta_2 < \frac{\pi}{2}$,

θ_3 uniform distributed in $-\frac{\pi}{3} < \theta_3 < \frac{\pi}{3}$,

θ_4 uniform distributed in $-\frac{\pi}{4} < \theta_4 < \frac{\pi}{4}$,

θ_5 uniform distributed in $-\frac{\pi}{5} < \theta_5 < \frac{\pi}{5}$.

(5) For the set 5

θ_2 uniform distributed in $-2\pi < \theta_2 < 2\pi$,

θ_3 uniform distributed in $-2\pi < \theta_3 < 2\pi$,

θ_4 uniform distributed in $-2\pi < \theta_4 < 2\pi$,

θ_5 uniform distributed in $-2\pi < \theta_5 < 2\pi$.

The parameters C_n are taken to be vanishing or varying according to a Gaussian distribution. For the set 1, we take nonvanishing C_n for $n = 2, 3$, while the corresponding event planes θ_2 and θ_3 are randomly chosen. We found that the obtained scatter plots of ε_n - v_n for $n = 4, 5$ are quite

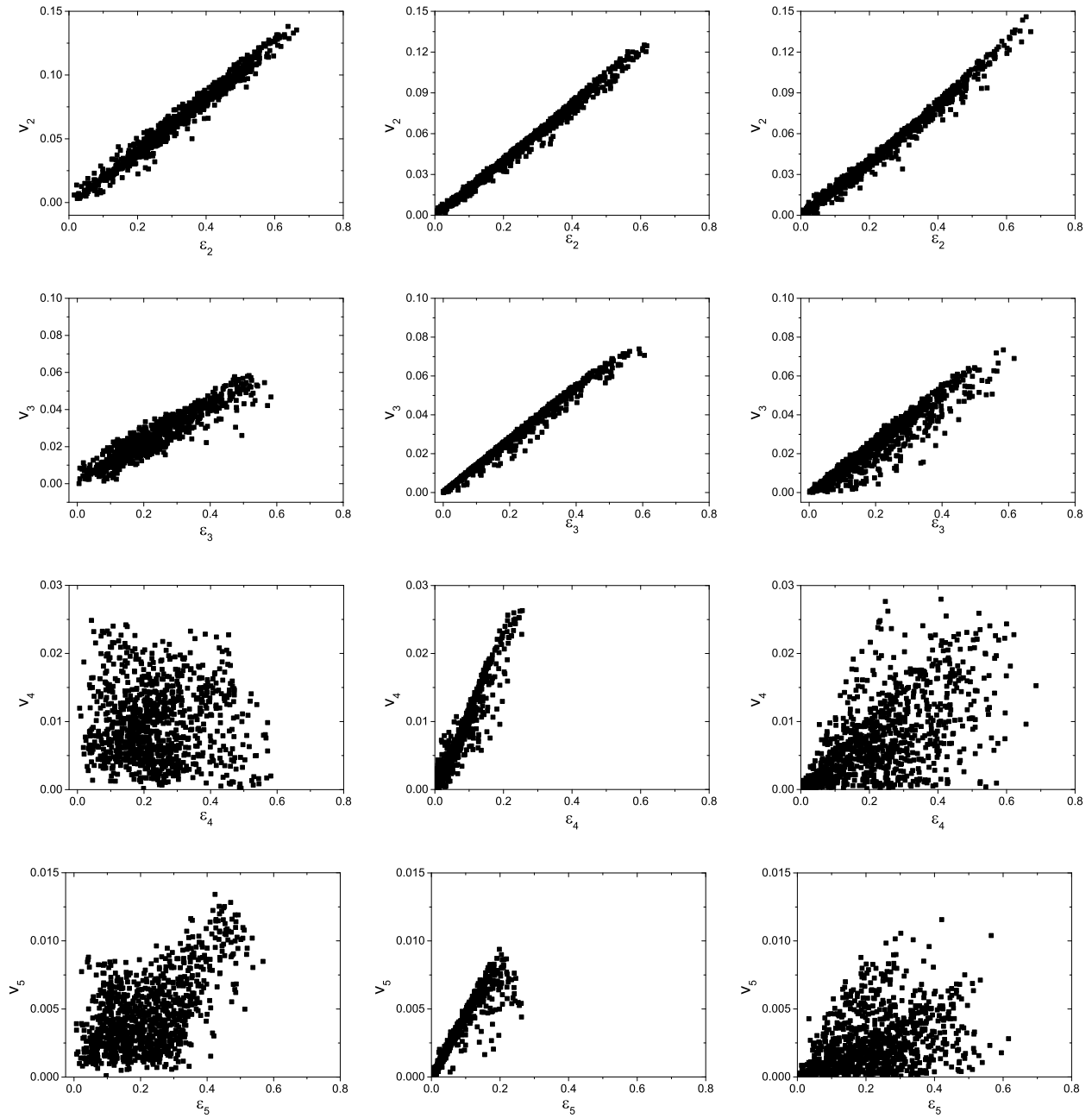


Fig. 15 – Left column: the scatter plots of flow harmonics v_n vs. eccentricities ε_n for the peripheral tube model; Middle column: the scatter plots of flow harmonics v_n vs. eccentricities ε_n for the anisotropic Gaussian model with parameter set 1; Right column: the scatter plots of flow harmonics v_n vs. eccentricities ε_n for the anisotropic Gaussian model with parameter set 2.

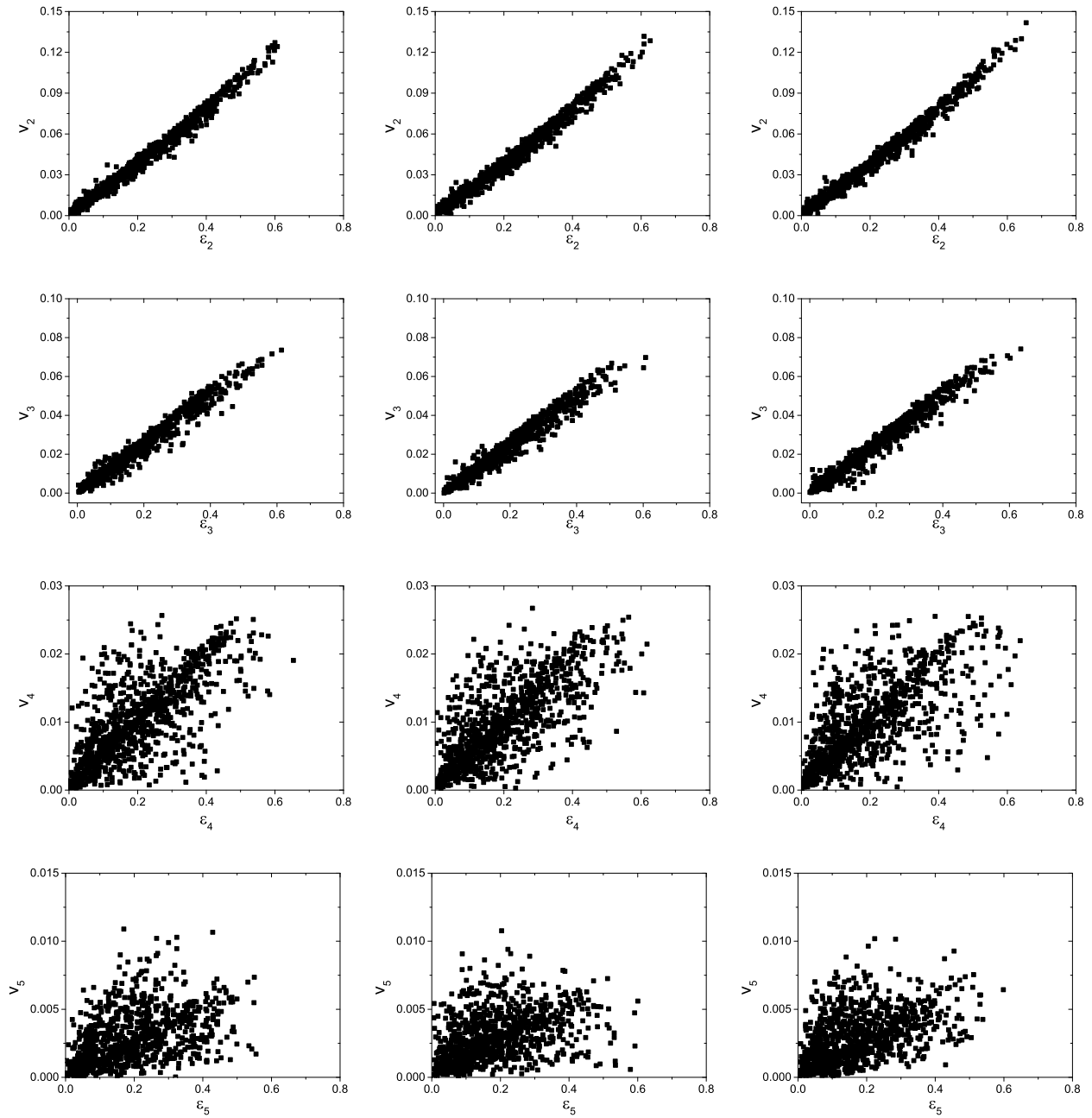


Fig. 16 – Left column: the scatter plots of flow harmonics v_n vs. eccentricities ε_n for the anisotropic Gaussian model with parameter set 3; Middle column: the scatter plots of flow harmonics v_n vs. eccentricities ε_n for the anisotropic Gaussian model with parameter set 4; Right column: the scatter plots of flow harmonics v_n vs. eccentricities ε_n for the anisotropic Gaussian model with parameter set 5.

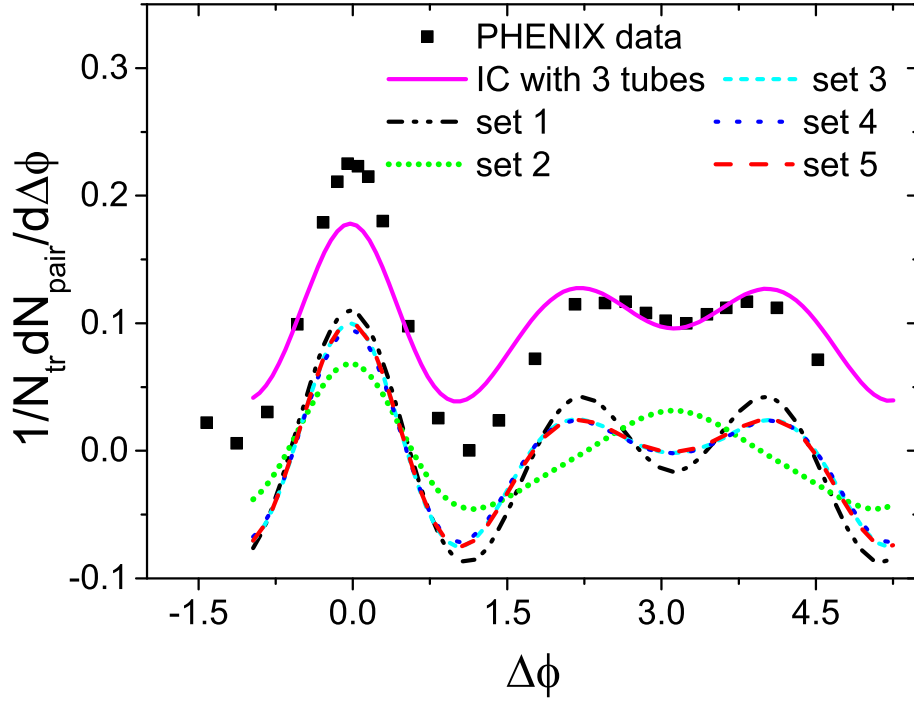


Fig. 17 – (Color online) A comparison of the calculated di-hadron correlations for $0.4 < p_{associated} < 1$ and $2 < p_{trigger} < 3$ for different IC: the peripheral tube model and the anisotropic Gaussian model with parameter sets 1, 2, 3, 4, 5, comparing with PHENIX data.

different from those of the peripheral tube model, as shown in Fig. 15. The resulting two-particle correlations shows a slightly higher “shoulder” as shown in Fig. 17. For the sets 2, 3, 4, and 5, we take nonvanishing C_n only for the corresponding n , and set all other $C_m = 0$ for any $m \neq n$. Moreover, for the set 2, we take $\theta_n = 0$. For the sets 3, 4, and 5, θ_n is drawn randomly. The obtained scatter plots $\varepsilon_n - v_n$ are found to be similar to those of the peripheral tube model, as shown in Fig. 15 and Fig. 16. For the set 2, the resulting two-particle correlations are quite different from those of the peripheral tube model. On the other hand, for the sets 3, 4, and 5, the two-particle correlations possess similar shapes to those those found in the peripheral tube model as shown in Fig. 17. In a word, by adjusting the anisotropic Gaussian model parameters C_n and θ_n , we can obtain the $\varepsilon_n - v_n$ relations and two-particle correlations similar to that one in tube model.

However, in Fig. 18, we find the probability density distributions of the event-by-event ε_n and v_n for set 4 in anisotropic Gaussian model is different from tube model, although the $\varepsilon_n - v_n$ relations and two-particle correlations for set 4 in anisotropic Gaussian model looks similar with tube model. In addition, it is difficult to see from the results of the two-particle correlation whether the high-order flow coefficients under the two models are consistent. Therefore, in order to further compare the high-order flow coefficients in this two models with the experimental data of the Pb+Pb collision at 2.76 TeV, we will simulate the Pb+Pb collision by using the tube model and the anisotropic Gaussian model in next section.

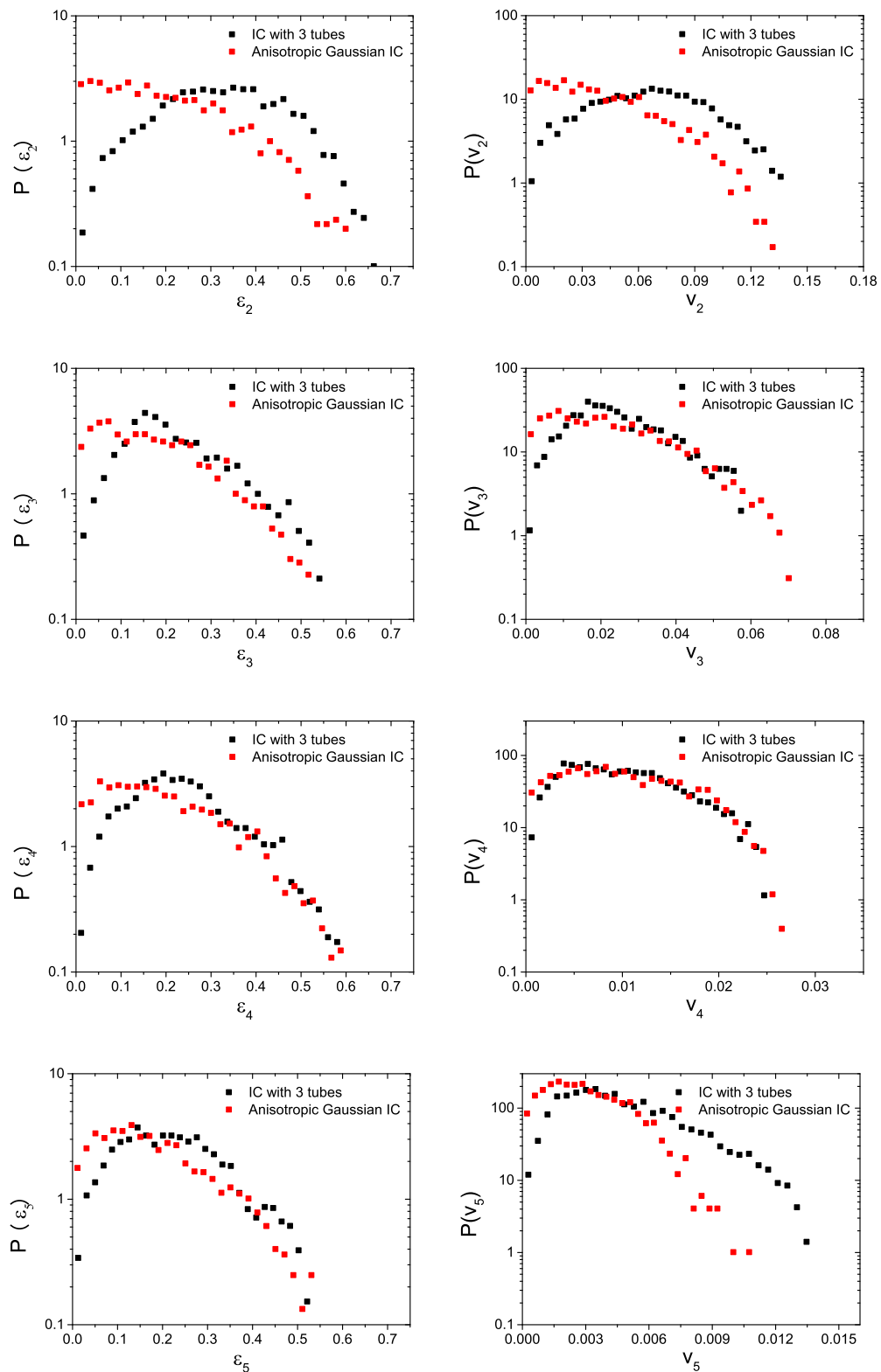


Fig. 18 – (Color online) Left column: the probability density distributions of the EbyE ε_n in anisotropic Gaussian model and peripheral tube model; Right column: the probability density distributions of the EbyE v_n in anisotropic Gaussian model and peripheral tube model

5.2 SIMULATIONS FOR 2.76 TEV PB+PB COLLISIONS AT 20% – 25% CENTRALITY BY USING PERIPHERAL TUBE MODEL AND ANISOTROPIC GAUSSIAN MODEL

In last section, we learned that we always can obtain the similar two-particle correlations by choosing property parameters in these two different models. For a further study, in this section, we will concentrate on the nature of high-order flows. To compare with experimental data, we will do simulations of 2.76 TeV Pb+Pb collisions at 20% – 25% centrality by using anisotropic Gaussian model and peripheral Tube Model.

We first parameterize the average EPOS initial conditions obtained from many events. Then placing three high-energy tubes on this average IC background, and by adjusting the radius, energy and position of the tubes, we obtained the two-particle correlation close to the EPOS+SPheRIO simulation. Subsequently, under the precondition that the total energy is similar and the probability density distribution of ε_n is similar, we use the tube model and the anisotropic Gaussian model to do the simulation of Pb+Pb collisions. At last, we compare these two models in various aspects, including temporal evolution, ε_n - v_n relations, probability density distribution of the event-by-event v_n , di-hadron correlations, nonlinear response coefficients, symmetric cumulants and mixed-harmonics.

5.2.1 Parameterization of models

In order to design initial conditions of peripheral tube model, we first employ EPOS to generate the initial conditions for $\sqrt{s_{NN}} = 2.76$ TeV Pb+Pb collisions at 20% – 25% centrality. And we average out the ICs of 2800 events, the averaged IC is shown in Fig. 19.

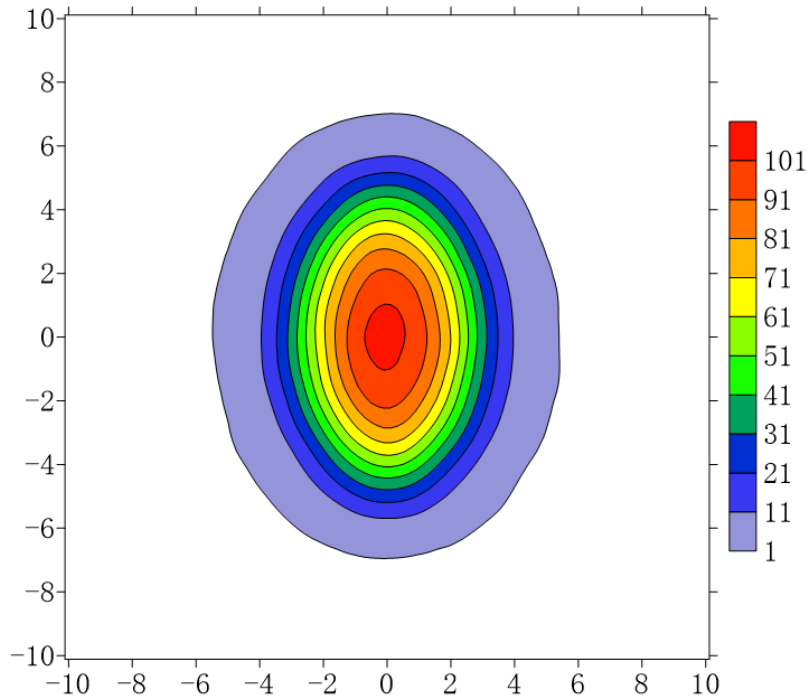


Fig. 19 – (Color online) The averaged EPOS IC for $\sqrt{s_{NN}} = 2.76$ TeV Pb+Pb collisions at 20%–25% centrality.

Then, we parameterize the averaged IC of Pb+Pb collisions for the 20% – 25% centrality class

at 2.76 TeV in the $x - y$ plane by using Eq.(2), and take it as background, hence the parameters K , L , M , a , b , c are determined as in Table.2. Subsequently, we put three tubes given by Eq.(4) on the background. The maximum energy A_{tube} and the location r_0 of tubes are determined based on the results of the two-particle correlation, we take different value to carry out the two-particle correlations, see in Fig. 20.

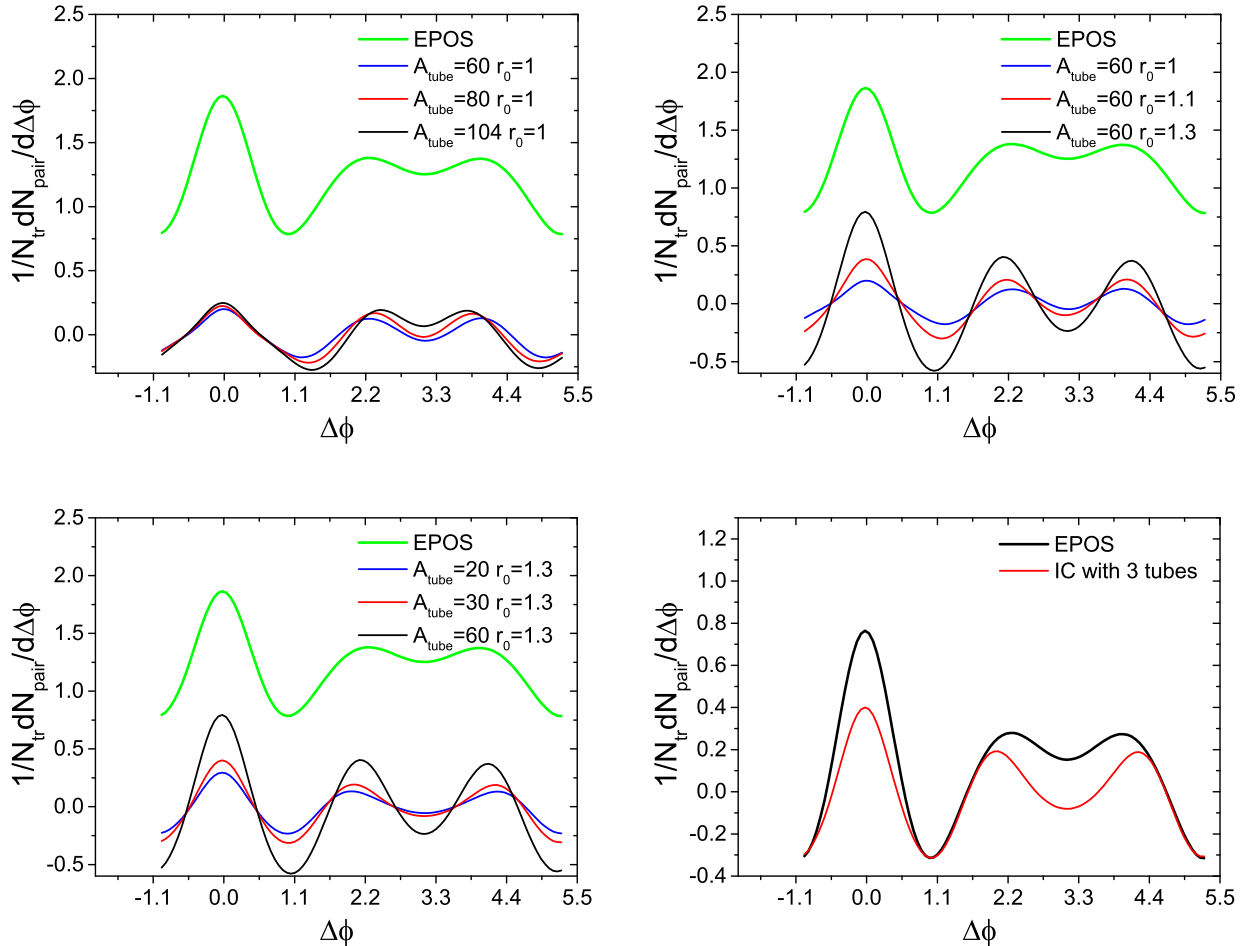


Fig. 20 – (Color online) The di-hadron correlations for different value of peripheral tube model parameters, and $0.4 < p_{\text{associated}} < 1$ and $2 < p_{\text{trigger}} < 3$. Left column are results for different maximum energy of tubes at a given radial position, at the top of the right column are results for different radial positions of tubes at a given maximum energy, at the bottom of the right column is the results for $A_{\text{tube}} = 30$ and $r_0 = 1.3$ comparing with EPOS+SPHeRIO results which has been translated.

Finally, when we take $A_{\text{tube}} = 30$ and $r_0 = 1.3$, it can reproduce the two-particle correlation closer to the results of EPOS+SPHeRIO simulations. Therefore, the parameters used in the present study are summarized in Table 2.

As a comparison, we introduce the anisotropic Gaussian model discussed in last section. It satisfies the precondition that the anisotropic Gaussian model and the peripheral tube model have the similar initial total energy and similar probability density distributions of eccentricity ε_n . The parameters employed for the anisotropic Gaussian model are summarized in the Table 3. The parameters

Table 2 – The model parameters of the peripheral tube model in the present study

K	L	M
103.9	-89	28.5
a	b	c
0.077	0.033	2
A_{tube}	r_0	R_{tube}
30	1.3	1.1

C_n are randomly chosen to satisfy a normal distribution centered at M_n with standard deviation σ_n . This is carried out numerically using the Box-Muller method as follows. One first picks out U_1 and U_2 , two independent, uniformly distributed random numbers in the interval $[0, 1]$. Then, C_n can be evaluated accordingly to the following expressions

$$G = \sqrt{-2 \ln U_1} \cos(2\pi U_2), \quad (19)$$

$$C_n = G \cdot \sigma_n + M_n. \quad (20)$$

If one obtains a negative C_n , it is simply being cast out.

Table 3 – The model parameters of the anisotropic Gaussian model in the present study

R_0	3.1	
Z	133	
n	σ_n	M_n
2	0.075	0.39
3	0.095	0.045
4	0.145	0.073
5	0.128	0.063

5.2.2 Numerical results

As discussed above, the parameterization of the peripheral tube model is adjusted to mimic event-by-event fluctuating initial conditions generated by EPOS. On the other hand, those of the anisotropic Gaussian model is tailored accordingly to produce mostly identical eccentricity distribution. However, both the IC and the subsequent temporal evolutions are quite different visually, as clearly demonstrated in Fig. 21. In the case of the tube model, evolution is evidently dominated by the deflection of the flow by the high energy tubes. To be specific, the resultant peaks of particle emission are clearly associated with the locations of the three tubes, as discussed in Refs. (ANDRADE et al., 2010a; WEN et al., 2019). On the other hand, in the case of anisotropic Gaussian model, the overall energy distribution is smoother. It is rather difficult to predict the resultant evolution. Although, on an event-by-event average, the apparent mapping between IC eccentricities and flow harmonics can be established, as discussed below.

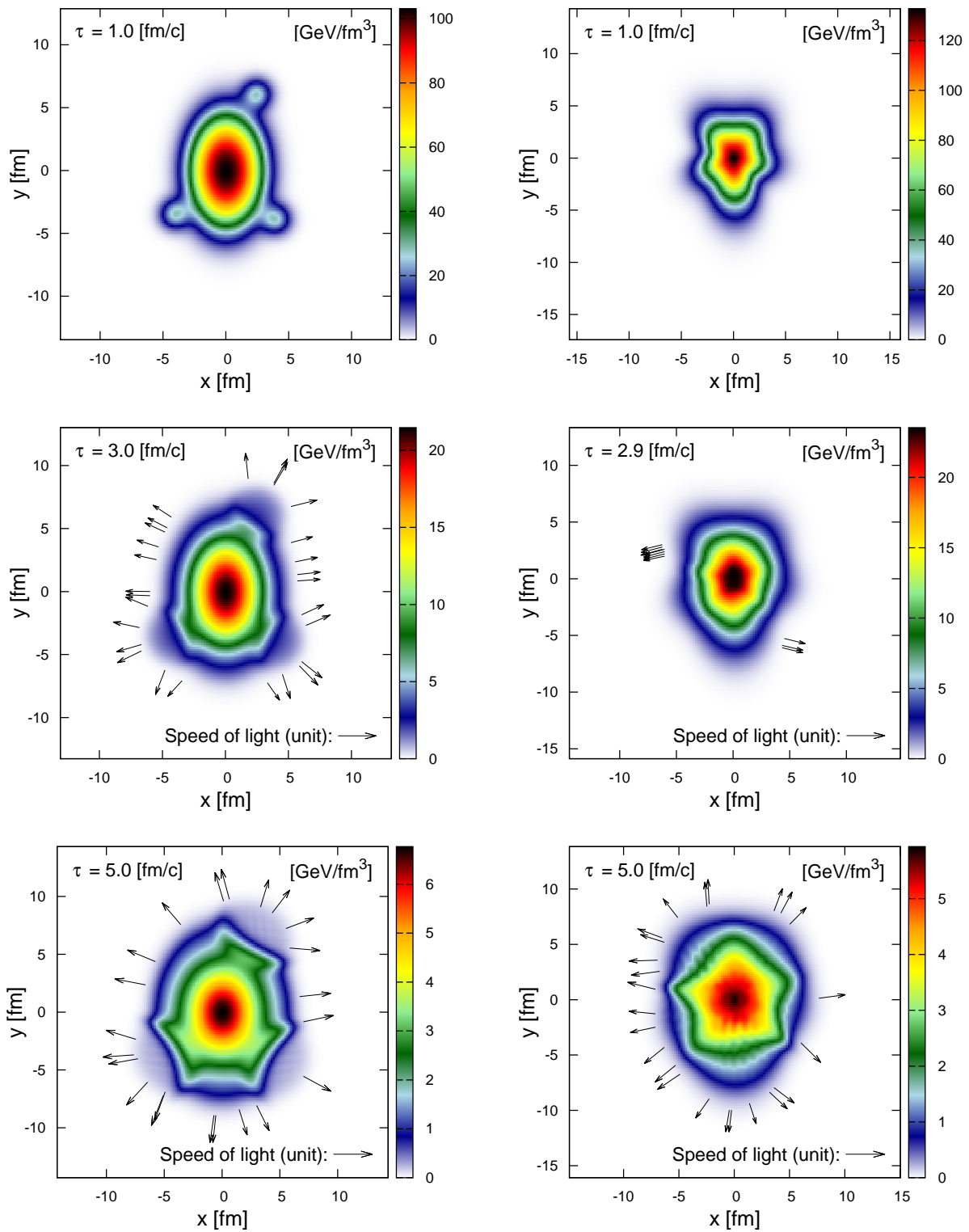


Fig. 21 – (Color online) The calculated temporal evolution of two random events of the peripheral tube model with three tubes (left column) and of anisotropic Gaussian model (right column).

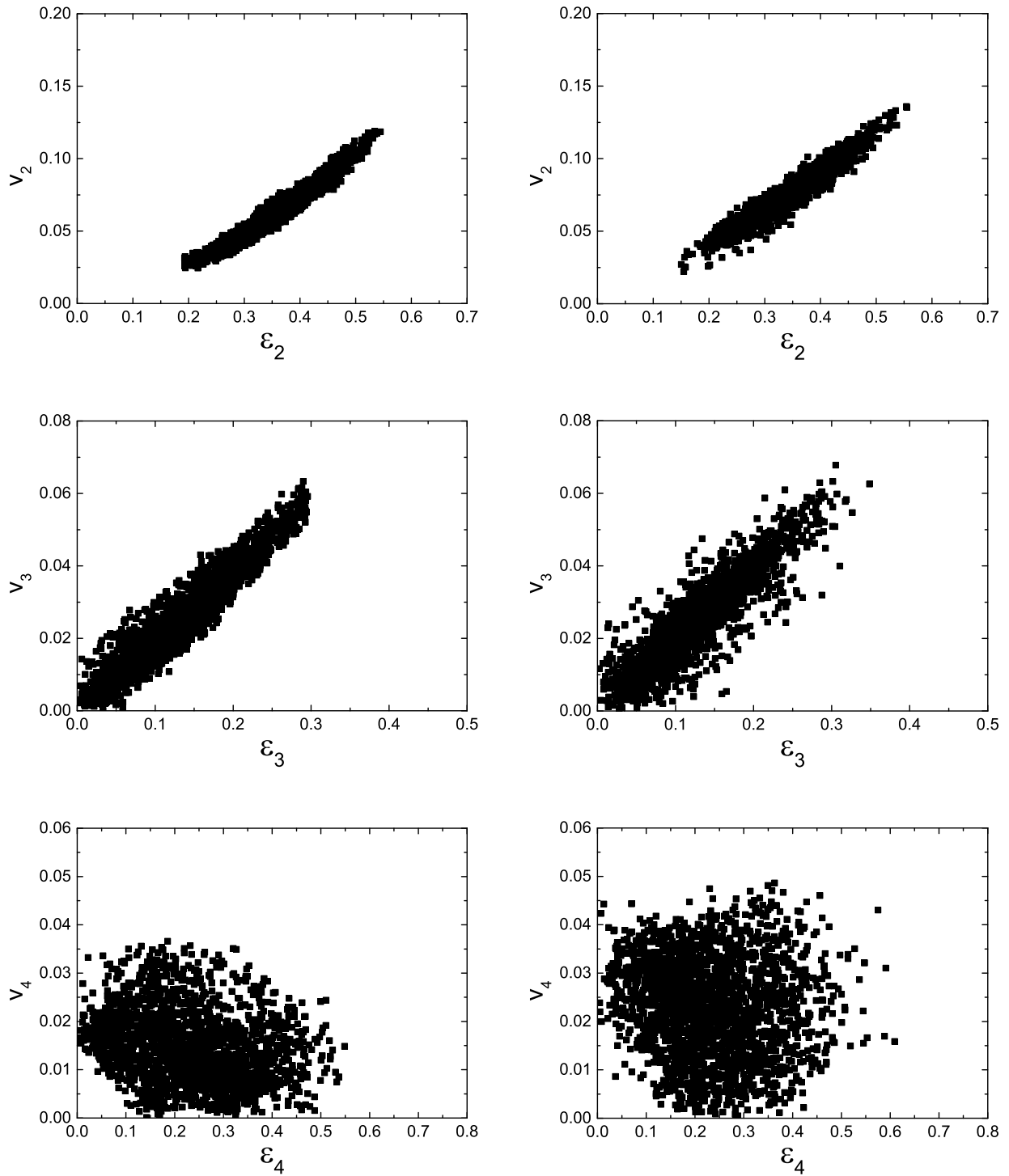


Fig. 22 – (Color online) The calculated scatter plots of flow harmonics v_n vs. eccentricities ϵ_n obtained by the peripheral tube model (left column) and anisotropic Gaussian model (right column). In both cases, a total of 2000 events have been used to draw the plot.

We have investigate the relationship between eccentricities and flow harmonics for both models. The resulting scatter plots of flow harmonics v_n vs. eccetricities ϵ_n are shown in Fig. 22. It indicates a significant positive linear correlation between ϵ_2 and v_2 . However, as observed in preivous studies (NIEMI et al., 2012; FU, 2015), the above correlations decrease as n increases. A comparison between the tube model and the anisotropic Gaussian model shows that the linearities presented in the two models are quite similar, although the former seems slightly stronger.

To present the results from a different aspect, we show the probability density distributions of event-by-event eccentricities ϵ_n , as well as those of flow harmonics v_n , in Fig. 23. Here the calculated probability distributions from the two models are compared against each other. The plots in the left column of Fig. 23 give the probability density distributions of initial eccentricities. This mostly serves to ensure quantitatively that the tuned models do possess “similar” IC in terms of eccentricity components. The right column, on the other hand, presents the resulting event-by-event distributions of flow harmonics. Here, a sizable difference is observed in the case of the elliptic and quadrangular flow coefficients. We note that this observation does not contradict to the linearity that one may draw from Fig. 22. In fact, this is consistent with the fact, for instance, the slope of the top-right plot of Fig. 22 is slightly larger than that of the top-left plot.

Table 4 – The calculated average v_n for 2.76 Tev Pb+Pb collisions at 20% – 25% centrality

	v_2	v_3	v_4	v_5
Peripheral tube model	0.064	0.026	0.0146	0.0049
Anisotropic Gaussian model	0.078	0.025	0.0228	0.008

At the same time, we find that the average value of v_n calculated in this two models are not completely consistent as shown in Table (4). Besides, we have calculated the p_T dependence of v_3 by using event plane method in Fig. 24. It shows that although the probability density distribution and average value of v_3 are approximately equal, the p_T dependence of v_3 in this two model is different.

To further investigate the linearity, we rescale the above results and present the normalized probability distributions in Fig. 25. However, for the present purpose, we show in the same plot, the normalized distribution of ϵ_n against that of v_n . We note that, in comparison with other existing results (GALE et al., 2013a; FU, 2015; BOZEK; BRONIOWSKI, 2013; GALE et al., 2013b), the peripheral tube model does present somewhat distinct features that the distribution of v_2 does not follow the distribution of ϵ_2 . However, since eccentricity cannot be measured experimentally, the present findings do not contradict with any existing theory straightforwardly. On the other hand, this result can be intuitively understood in terms of the peripheral tube model. When a tube is located deep inside the system, the effect of its hydrodynamic expansion is mostly absorbed by the surrounding medium. As a result, although it contributes significantly to the eccentricity, due to the smallness of its radial coordinate, it causes relatively insignificant impact to the flow harmonics. On the contrary, a tube sitting close to the surface possesses the precisely opposite characteristic. It leads to a significant disturbance to the one-particle distribution, resulting in sizable inhomogeneity in the media, while contributes little to the initial eccentricity. As the IC configuration exaggerate the above feature, to some extent, its subsequent manifestation observed in Fig. 25 is expected.

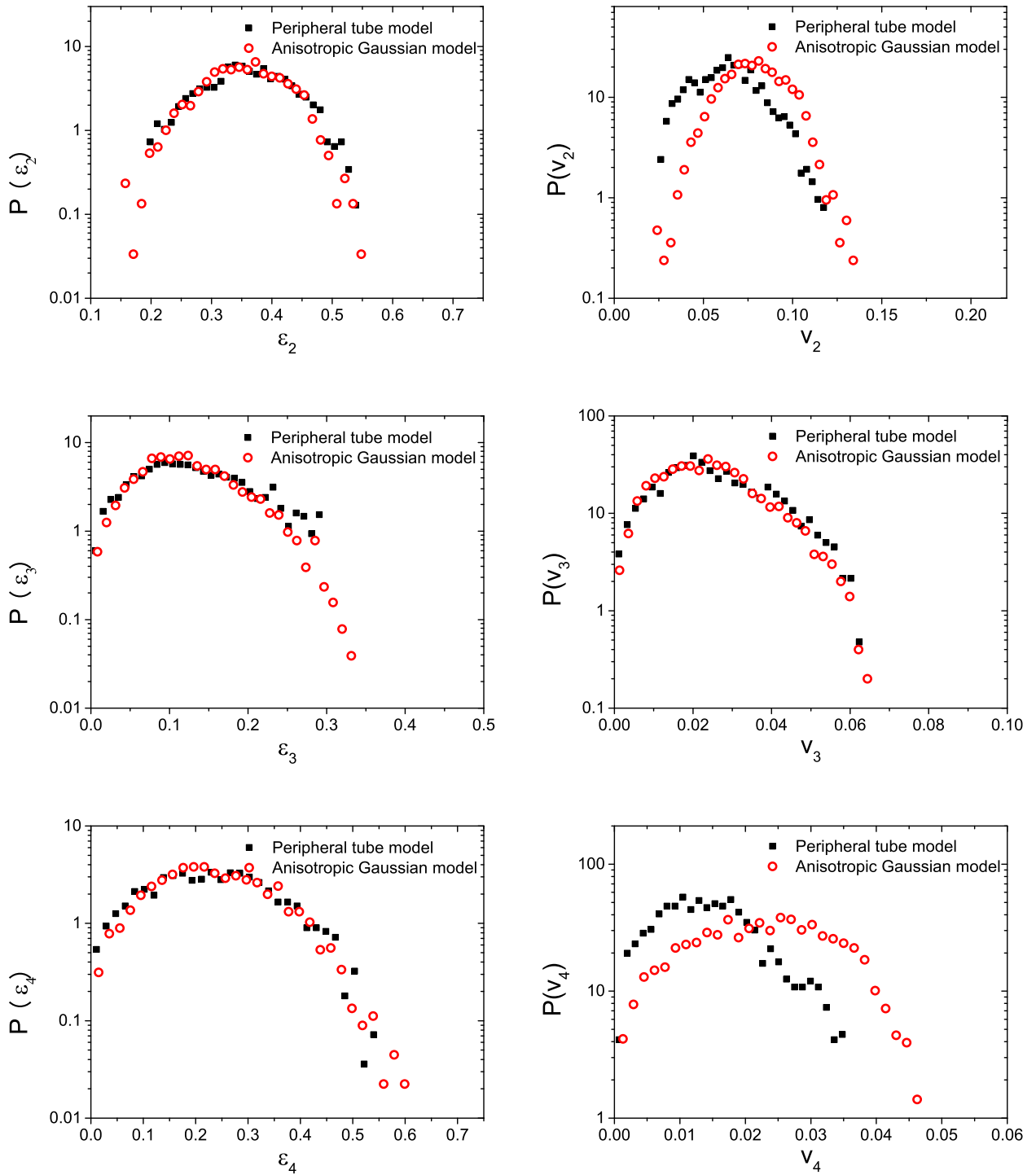


Fig. 23 – (Color online) Left: the probability density distribution of the event-by-event ε_n in the peripheral tube model and anisotropic Gaussian model; Right: The probability density distributions of the resultant flow harmonics v_n in the two models.

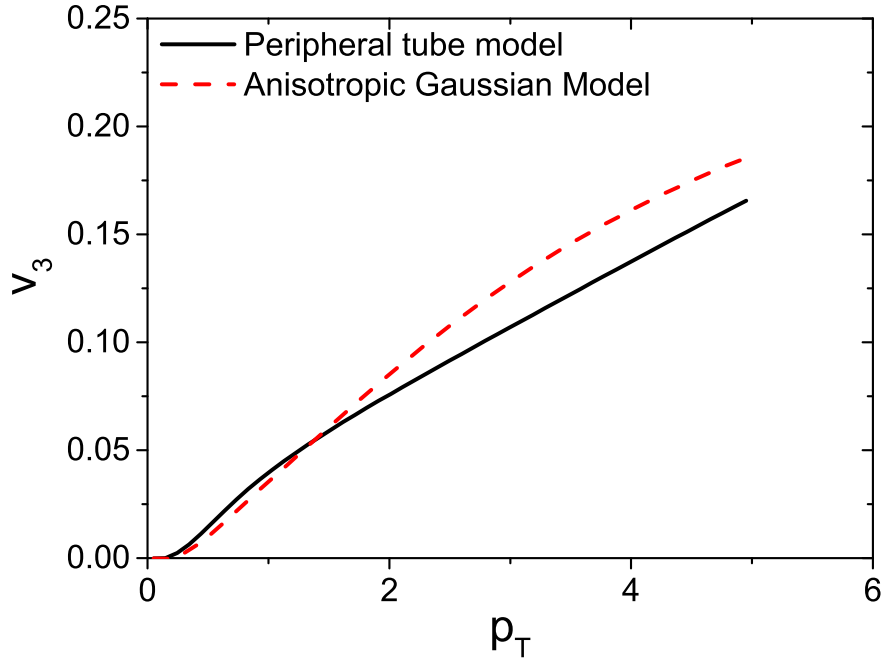


Fig. 24 – p_T dependence of v_3 in anisotropic Gaussian model and peripheral tube model.

In Fig. 26, we evaluate the di-hadron correlations for the peripheral tube model and the anisotropic Gaussian model. We note that the resulting correlations shown in Fig. 26 do not attain zero at the minimum. This is simply because the IC prepared in the present study does not contain any fluctuation in total entropy, and therefore, the resultant multiplicity fluctuations are minimized. In fact, one can numerically check that the correlations presented in Fig. 26 integrate to zero over a period $0 < \Delta\phi \leq 2\pi$. As shown in our previous studies, the main features of the obtained di-hadron correlations are very similar for the two models.

Now, we move to the study of linear and nonlinear response coefficients and other observables related to higher moments. By making use of the complex anisotropic flow coefficient (BHALERAO; OLLITRAULT; PAL, 2015)

$$P(\phi) = \frac{1}{2\pi} \sum_{n=-\infty}^{+\infty} V_n e^{-in\phi} \quad (21)$$

where $V_n = v_n \exp(in\Psi_n)$, and $v_n = |V_n|$. Subsequently, one may study the nonlinear response

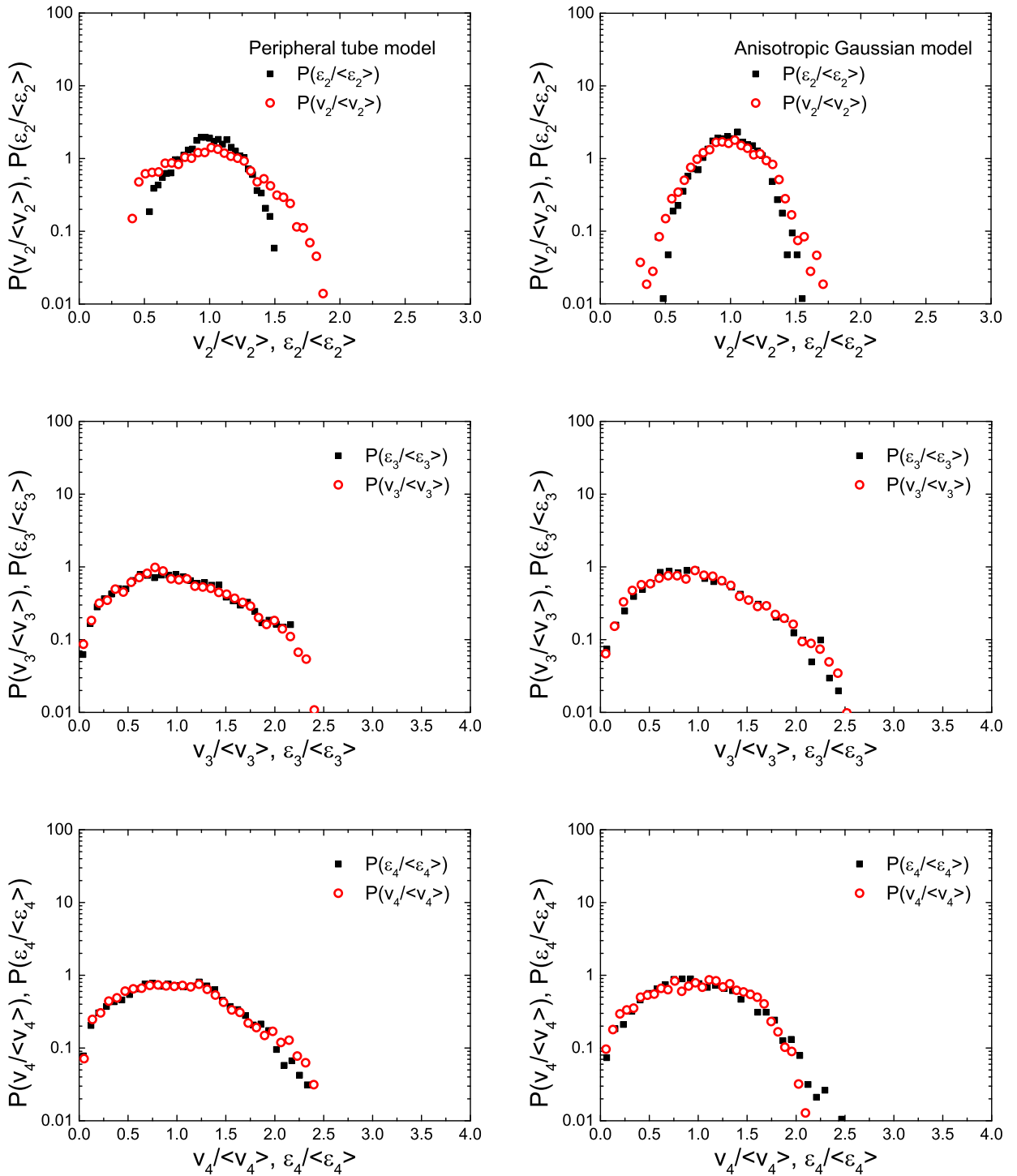


Fig. 25 – (Color online) The normalized probability density distribution of the event-by-event ε_n and v_n in the peripheral tube model (left column) and anisotropic Gaussian model (right column).

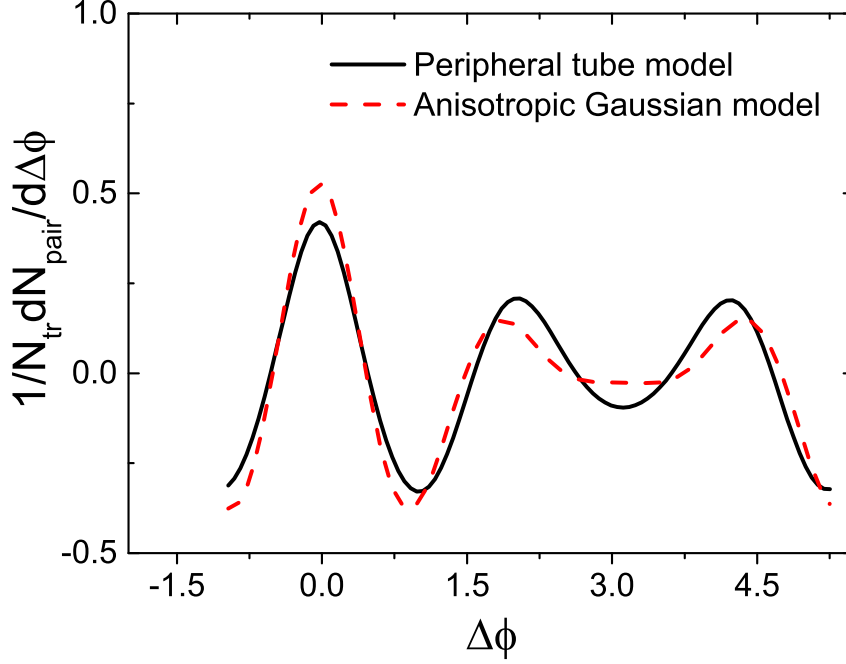


Fig. 26 – (Color online) A comparison of the di-hadron correlations for $0.4 < p_{\text{associated}} < 1$ and $2 < p_{\text{trigger}} < 3$ for anisotropic Gaussian model and peripheral tube model.

coefficients given by (BHALERAO; OLLITRAULT; PAL, 2015; YAN; OLLITRAULT, 2015)

$$\chi_4 = \frac{\langle V_4(V_2^*)^2 \rangle}{\langle |V_2|^4 \rangle} = \frac{\langle v_4 v_2^2 \cos(4[\Psi_4 - \Psi_2]) \rangle}{\langle v_2^4 \rangle}, \quad (22)$$

$$\chi_5 = \frac{\langle V_5 V_2^* V_3^* \rangle}{\langle |V_2|^2 |V_3|^2 \rangle} = \frac{\langle v_5 v_2 v_3 \cos(5\Psi_5 - 2\Psi_2 - 3\Psi_3) \rangle}{\langle v_2^2 v_3^2 \rangle}, \quad (23)$$

$$\chi_{62} = \frac{\langle V_6(V_2^*)^3 \rangle}{\langle |V_2|^6 \rangle} = \frac{\langle v_6 v_2^3 \cos(6[\Psi_6 - \Psi_2]) \rangle}{\langle v_2^6 \rangle}, \quad (24)$$

$$\chi_{63} = \frac{\langle V_6(V_3^*)^2 \rangle}{\langle |V_3|^4 \rangle} = \frac{\langle v_6 v_3^2 \cos(6[\Psi_6 - \Psi_3]) \rangle}{\langle v_3^4 \rangle}, \quad (25)$$

where, for instance, the imaginary part of the first expression $\langle v_4 v_2^2 \sin(4[\Psi_4 - \Psi_2]) \rangle = 0$ for a large number of events. In Table 5, we present the calculated nonlinear response coefficients evaluated for the two models in comparison to the EPOS+SPhERIO simulations and experimental data from CMS and ATLAS (YAN; PAL; OLLITRAULT, 2016; CHATRCHYAN et al., 2014; AAD et al., 2014). We find that the simulation results are systematically higher than experimental data, especially for peripheral tube model and anisotropic Gaussian model. Though not shown explicitly here, when included the statistical uncertainties, the EPOS+SPhERIO results are primarily consistent with the experimental data with error bars taken into consideration. The results between the peripheral model and anisotropic Gaussian model are, mostly, of similar magnitude, but the difference is substantial. In fact, the difference between the two models regarding nonlinear response coefficients is more substantial than that of linear ones, discussed above.

Table 5 – The calculated nonlinear response coefficients for 2.76 TeV Pb+Pb collisions for the 20%-25% centrality class.

	Number of events	χ_4	χ_5	χ_{62}	χ_{63}
CMS and ATLAS data		0.818	1.878	0.715	0.878
EPOS+SPhRIO	(1800 events)	1.13	2.44	1.08	1.11
Peripheral tube model	(2000 events)	1.50	2.44	3.46	2.33
Anisotropic Gaussian model	(2200 events)	1.69	2.794	2.97	1.12

In Table 6, we present the results of symmetric cumulants as well as normalized symmetric cumulants (ADAM et al., 2016), calculated by using the following definitions.

$$SC(m, n) = \langle v_n^2 v_m^2 \rangle - \langle v_n^2 \rangle \langle v_m^2 \rangle, \quad (26)$$

$$NSC(m, n) = \frac{\langle v_n^2 v_m^2 \rangle - \langle v_n^2 \rangle \langle v_m^2 \rangle}{\langle v_n^2 \rangle \langle v_m^2 \rangle}. \quad (27)$$

Again, the calculated results are compared with those from EPOS+SPhRIO simulations for 2.76 TeV Pb+Pb collisions in 20% – 25% centrality class. Lastly, we show in Table 7 the calculated mixed cumulants, also compared with the EPOS+SPhRIO results. The normalized symmetric cumulant is understood as a measure for the correlation of the magnitude of flow fluctuations. The mixed harmonics, on the other hand, are related to the ratios between flow harmonics evaluated by different event planes. It is found that the difference between the two models is significant. Especially for $SC(4, 2)$ and $NSC(4, 2)$, the signs of the correlations are opposite for the two models. The observed difference residing in higher harmonics and nonlinear response coefficients reflects the distinction between these two models.

Table 6 – The calculated symmetric cumulants for 2.76 TeV Pb+Pb collisions in 20% – 25% centrality class.

	$SC(4, 2)$	$SC(3, 2)$	$NSC(4, 2)$	$NSC(3, 2)$
EPOS	0.383×10^{-6}	-0.116×10^{-6}	0.177	-0.02
Peripheral tube model	0.043×10^{-6}	0.134×10^{-6}	0.035	0.035
Anisotropic Gaussian model	-0.252×10^{-6}	0.0552×10^{-6}	-0.063	0.011

Table 7 – The mixed harmonics for 2.76 TeV Pb+Pb collisions in 20% – 25% centrality class.

	EPOS	Peripheral tube model	Anisotropic Gaussian model
$\langle v_4 v_2^2 \cos(4[\Psi_4 - \Psi_2]) \rangle$	7.72×10^{-5}	4.09×10^{-5}	8.39×10^{-5}
$\langle v_5 v_2 v_3 \cos(5\Psi_5 - 2\Psi_2 - 3\Psi_3) \rangle$	1.38×10^{-5}	0.954×10^{-5}	1.38×10^{-5}
$\langle v_6 v_2^3 \cos(6[\Psi_6 - \Psi_2]) \rangle$	0.0874×10^{-5}	0.0721×10^{-5}	0.129×10^{-5}
$\langle v_6 v_3^2 \cos(6[\Psi_6 - \Psi_3]) \rangle$	0.157×10^{-5}	0.301×10^{-5}	0.119×10^{-5}

6 CONCLUSION

To summarize, in this thesis, we have explored several aspects regarding the collectivity in hydrodynamics and its connection with initial state fluctuations. To this end, we investigated eccentricities, and observables such as two-particle correlation, flow harmonics, linear and nonlinear response coefficients, among others. These studies have been mostly carried out by employing a peripheral tube model. The latter was proposed to provide an intuitive explanation on many features of the observed data, such as elliptic flow, the ridge structures of two-particle correlation, event plane correlations, and the centrality dependence of di-hadron correlations in previous work. In particular, we show that the two-particle correlations obtained by event-by-event hydrodynamical simulations using appropriately devised IC of the peripheral tube model are consistent with experimental data. The latter is further shown to be in qualitative agreement with those by using the analytic result of a simplified model with the parameters extracted from flow coefficients and multiplicity fluctuations. This indicates that the peripheral tube model is a reasonable approach for the interpretation of the observed features of the two-particle correlations in nuclear collisions.

The hydrodynamical approach is shown to be a success for the description of many experimental data of relativistic heavy ion collisions. In particular, it provides a reasonable description for the observed two-particle correlations. One distinct feature of the observables in question, as we understand, is that they usually involve an event-average procedure, and thus may not necessarily carry all the information on genuine nonlinear nature of hydrodynamics. In other words, although the event averaged harmonic coefficients display a strong linear relation to those averaged initial state eccentricities (NIEMI et al., 2012), some essential characteristics associated with the nonlinearity may still be hidden and failed to be captured through averaged values. Subsequently, the distinction between different approaches may become less visible. It is also interesting to note that the transport models such as AMPT or PHSD have shown to have similar properties as viscous hydrodynamic calculations (MA; WANG, 2011; XU; KO, 2011; SOUZA; KOIDE; KODAMA, 2016). However, when one looks closely on an event-by-event basis, a state close to the local thermal equilibrium only corresponds to a tiny space-time domain during the entire dynamical evolution as in Ref. (SOUZA; KOIDE; KODAMA, 2016; XU et al., 2017). To clarify up to what extent the genuine event-by-event hydrodynamics is valid, it may require a set of observables which are sensitive to the non-linear evolution of the system. Then, it motivates our current work.

Moreover, we devised an anisotropic Gaussian model to match the eccentricity probability distribution of the peripheral tube model. By doing this, we carried out a back-to-back comparison between the two models regarding the mapping between the event-by-event IC fluctuations and flow harmonics. In particular, we studied the linear as well as the nonlinear response of the system in terms of flow harmonic coefficients, di-hadron correlations, symmetric cumulants, mixed harmonics, among others. Although the di-hadron correlations seem similar in their shapes, the distinction between the two models can be revealed by more detailed observables. In particular, the discrepancies in the normalized probability distributions of ϵ_2 and v_2 can be readily understood in terms of the physical

nature of the peripheral tube model. Furthermore, the calculated symmetric cumulant and normalized symmetric cumulant, the so-called Pearson correlation coefficient regarding higher-order harmonics also demonstrated a substantial difference between the two models. In this context, it might be interesting to follow this train of thought by proposing observables, which may quantify the nonlinearity to a greater extent. Further studies concerning this topic, such as principal component analysis are in progress.

BIBLIOGRAPHY

- AAD, G. et al. Measurement of the azimuthal anisotropy for charged particle production in 2.76 TeV lead-lead collisions with the ATLAS detector. **Physical Review C**, APS, v. 86, n. 1, p. 014907, 2012.
- AAD, G. et al. Measurement of the distributions of event-by-event flow harmonics in lead-lead collisions at $\sqrt{s_{NN}} = 2.76$ TeV with the ATLAS detector at the LHC. **JHEP**, v. 11, p. 183, 2013.
- AAD, G. et al. Measurement of event-plane correlations in $\sqrt{s_{NN}} = 2.76$ TeV lead-lead collisions with the ATLAS detector. **Phys. Rev.**, C90, n. 2, p. 024905, 2014.
- AAMODT, K. et al. Higher harmonic anisotropic flow measurements of charged particles in Pb-Pb collisions at $\sqrt{s_{NN}} = 2.76$ TeV. **Phys. Rev. Lett.**, v. 107, p. 032301, 2011.
- AAMODT, K. et al. Harmonic decomposition of two-particle angular correlations in Pb-Pb collisions at $\sqrt{s_{NN}} = 2.76$ TeV. **Phys. Lett.**, B708, p. 249–264, 2012.
- ABELEV, B. et al. Partonic flow and ϕ -meson production in Au+ Au collisions at 200 GeV. **Physical review letters**, APS, v. 99, n. 11, p. 112301, 2007.
- ABELEV, B. et al. Centrality dependence of charged hadron and strange hadron elliptic flow from Au+ Au collisions at 200 GeV. **Physical Review C**, APS, v. 77, n. 5, p. 054901, 2008.
- ACKERMANN, K. et al. Elliptic flow in Au+ Au collisions at 130 GeV. **Physical Review Letters**, APS, v. 86, n. 3, p. 402, 2001.
- ADAM, J. et al. Correlated event-by-event fluctuations of flow harmonics in Pb-Pb collisions at $\sqrt{s_{NN}} = 2.76$ TeV. **Phys. Rev. Lett.**, v. 117, p. 182301, 2016.
- ADAMS, J. et al. Evidence from Au+ Au measurements for final-state suppression of high- p_T hadrons in Au+ Au collisions at RHIC. **Physical Review Letters**, APS, v. 91, n. 7, p. 072304, 2003.
- ADAMS, J. et al. Experimental and theoretical challenges in the search for the quark–gluon plasma: The STAR collaboration’s critical assessment of the evidence from RHIC collisions. **Nuclear Physics A**, Elsevier, v. 757, n. 1-2, p. 102–183, 2005.
- ADAMS, J. et al. Distributions of charged hadrons associated with high transverse momentum particles in pp and Au + Au collisions at $\sqrt{s_{NN}} = 200$ GeV. **Phys.Rev.Lett.**, v. 95, p. 152301, 2005.
- ADARE, A. et al. Measurements of higher order flow harmonics in Au+ Au collisions at 200 GeV. **Physical review letters**, APS, v. 107, n. 25, p. 252301, 2011.
- ADARE, A. et al. Dihadron azimuthal correlations in Au+Au collisions at $\sqrt{s_{NN}} = 200$ GeV. **Phys.Rev.**, C78, p. 014901, 2008.
- ADARE, A. et al. Measurements of Higher-Order Flow Harmonics in Au+Au Collisions at $\sqrt{s_{NN}} = 200$ GeV. **Phys.Rev.Lett.**, v. 107, p. 252301, 2011.
- ADCOX, K. et al. Formation of dense partonic matter in relativistic nucleus–nucleus collisions at RHIC: experimental evaluation by the PHENIX collaboration. **Nuclear Physics A**, Elsevier, v. 757, n. 1-2, p. 184–283, 2005.
- ADLER, C. et al. Elliptic flow from two- and four-particle correlations in Au+ Au collisions at $\sqrt{s_{NN}} = 130$ GeV. **Physical Review C**, APS, v. 66, n. 3, p. 034904, 2002.

- ADLER, S. et al. Dense-Medium Modifications to Jet-Induced Hadron Pair Distributions in Au+Au Collisions at $\sqrt{s(NN)} = 200$ -GeV. **Phys.Rev.Lett.**, v. 97, p. 052301, 2006.
- AFANASIEV, S. et al. Systematic Studies of Elliptic Flow Measurements in Au+Au Collisions at $\sqrt{s} = 200$ -GeV. **Phys. Rev.**, C80, p. 024909, 2009.
- AGAKISHIEV, G. et al. Strangeness enhancement in cu-cu and au-au collisions at 200 gev. **Physical review letters**, APS, v. 108, n. 7, p. 072301, 2012.
- AGAKISHIEV, H. et al. Measurements of Dihadron Correlations Relative to the Event Plane in Au+Au Collisions at $\sqrt{s_{NN}} = 200$ GeV. 2010.
- AGGARWAL, M. et al. Azimuthal anisotropy in s+ au reactions at 200 a gev. **Physics Letters B**, Elsevier, v. 403, n. 3-4, p. 390–396, 1997.
- AGUIAR, C. et al. Smoothed particle hydrodynamics for relativistic heavy ion collisions. **J.Phys.G**, G27, p. 75–94, 2001.
- AGUIAR, C. E. et al. Event-by-event fluctuations in hydrodynamical description of heavy-ion collisions. **Nuclear Physics A**, v. 698, n. 1, p. 639–642, 2002.
- AJITANAND, N. et al. Decomposition of harmonic and jet contributions to particle-pair correlations at ultra-relativistic energies. **Phys.Rev.**, C72, p. 011902, 2005.
- ALAM, J.-e.; RAHA, S.; SINHA, B. Electromagnetic probes of quark gluon plasma. **Physics Reports**, Elsevier, v. 273, n. 5-6, p. 243–362, 1996.
- ALT, C. et al. Directed and elliptic flow of charged pions and protons in pb+ pb collisions at 4.0 and 1.58 a gev. **Physical Review C**, APS, v. 68, n. 3, p. 034903, 2003.
- ALVER, B. et al. System size, energy, pseudorapidity, and centrality dependence of elliptic flow. **Physical review letters**, APS, v. 98, n. 24, p. 242302, 2007.
- ALVER, B.; ROLAND, G. Collision geometry fluctuations and triangular flow in heavy-ion collisions. **Phys.Rev.**, C81, p. 054905, 2010.
- ALVER, B. H. et al. Triangular flow in hydrodynamics and transport theory. **Phys. Rev.**, C82, p. 034913, 2010.
- ANDRADE, R. et al. On the necessity to include event-by-event fluctuations in experimental evaluation of elliptical flow. **Phys.Rev.Lett.**, v. 97, p. 202302, 2006.
- ANDRADE, R. et al. A Closer look at the influence of tubular initial conditions on two-particle correlations. **J.Phys.G**, G37, p. 094043, 2010.
- ANDRADE, R. et al. Boost-invariant one-tube model for two-particle correlation. 2010.
- ANDRADE, R. et al. Hydrodynamics: Fluctuating Initial Conditions and Two-particle Correlations. **Nucl.Phys.**, A854, p. 81–88, 2011.
- ANDRADE, R. et al. The ridge as a shadowing effect in hydrodynamics. **Phys.Part.Nucl.Lett.**, v. 8, p. 947–950, 2011.
- ANDRADE, R. P. G. et al. Temporal evolution of tubular initial conditions and their influence on two-particle correlations in relativistic nuclear collisions. **Phys.Lett.**, B712, p. 226–230, 2012.

- BACK, B. et al. Centrality and pseudorapidity dependence of elliptic flow for charged hadrons in au+ au collisions at $\sqrt{s_{nn}} = 200$ gev. **Physical Review C**, APS, v. 72, n. 5, p. 051901, 2005.
- BACK, B. et al. The phobos perspective on discoveries at rhic. **Nuclear Physics A**, Elsevier, v. 757, n. 1-2, p. 28–101, 2005.
- BACK, B. et al. Pseudorapidity and centrality dependence of the collective flow of charged particles in a u+ a u collisions at $\sqrt{s_{nn}} = 130$ g e v. **Physical review letters**, APS, v. 89, n. 22, p. 222301, 2002.
- BACK, B. et al. Significance of the fragmentation region in ultrarelativistic heavy-ion collisions. **Physical Review Letters**, APS, v. 91, n. 5, p. 052303, 2003.
- BACK, B. et al. Charged hadron transverse momentum distributions in au+ au collisions at 200 gev. **Physics Letters B**, Elsevier, v. 578, n. 3-4, p. 297–303, 2004.
- BARRETTE, J. et al. Observation of anisotropic event shapes and transverse flow in ultrarelativistic au+ au collisions. **Physical review letters**, APS, v. 73, n. 19, p. 2532, 1994.
- BARRETTE, J. et al. Energy and charged particle flow in 10.8 a gev/c au+ au collisions. **Physical Review C**, APS, v. 55, n. 3, p. 1420, 1997.
- BHALERAO, R.; BORGHINI, N.; OLLITRAULT, J.-Y. Analysis of anisotropic flow with lee–yang zeroes. **Nuclear Physics A**, Elsevier, v. 727, n. 3-4, p. 373–426, 2003.
- BHALERAO, R. S.; LUZUM, M.; OLLITRAULT, J.-Y. Determining initial-state fluctuations from flow measurements in heavy-ion collisions. **Phys. Rev.**, C84, p. 034910, 2011.
- BHALERAO, R. S.; OLLITRAULT, J.-Y.; PAL, S. Event-plane correlators. **Phys. Rev.**, C88, p. 024909, 2013.
- BHALERAO, R. S.; OLLITRAULT, J.-Y.; PAL, S. Characterizing flow fluctuations with moments. **Phys. Lett.**, B742, p. 94–98, 2015.
- BILANDZIC, A. et al. Generic framework for anisotropic flow analyses with multiparticle azimuthal correlations. **Phys. Rev.**, C89, n. 6, p. 064904, 2014.
- BILANDZIC, A.; SNELLINGS, R.; VOLOSHIN, S. Flow analysis with cumulants: Direct calculations. **Phys. Rev.**, C83, p. 044913, 2011.
- BJORKEN, J. D. Highly relativistic nucleus-nucleus collisions: The central rapidity region. **Physical review D**, APS, v. 27, n. 1, p. 140, 1983.
- BORGHINI, N.; DINH, P. M.; OLLITRAULT, J.-Y. Flow analysis from multiparticle azimuthal correlations. **Phys. Rev.**, C64, p. 054901, 2001.
- BORGHINI, N.; OLLITRAULT, J. Y.; DINH, M. Are flow measurements at sps reliable? **Phys. Rev. C**, v. 62, n. arXiv: 0004026, p. 034902, 2000.
- BOZEK, P.; BRONIOWSKI, W. Collective dynamics in high-energy proton-nucleus collisions. **Phys. Rev.**, C88, n. 1, p. 014903, 2013.
- CASTILHO, W. M. et al. Hydrodynamic approach to the centrality dependence of di-hadron correlations. **Phys.Rev.**, C95, p. 064908, 2017.
- CASTILHO, W. M. et al. Event-plane dependent di-hadron correlations with harmonic v_n subtraction in a hydrodynamic model. **Phys. Lett.**, B777, p. 369–373, 2018.

- CHATRCHYAN, S. et al. Measurement of higher-order harmonic azimuthal anisotropy in PbPb collisions at $\sqrt{s_{NN}} = 2.76$ TeV. **Phys. Rev.**, C89, n. 4, p. 044906, 2014.
- CHEN, J. et al. System size and energy dependence of ϕ meson production at rhic. **Journal of Physics G: Nuclear and Particle Physics**, IOP Publishing, v. 35, n. 10, p. 104053, 2008.
- CHEUK-YIN, W. **Introduction to high-energy heavy-ion collisions**. [S.l.]: World scientific, 1994.
- CHIU, C. B.; SUDARSHAN, E.; WANG, K.-H. Hydrodynamical expansion with frame-independence symmetry in high-energy multiparticle production. **Physical Review D**, APS, v. 12, n. 3, p. 902, 1975.
- CHIU, C. B.; WANG, K.-H. Hydrodynamical model with massless constituents. **Physical Review D**, APS, v. 12, n. 1, p. 272, 1975.
- COLLABORATION), C. Principal-component analysis of two-particle azimuthal correlations in pbbp and p pb collisions at cms. **Phys.rev.c**, v. 956, p. 308–311, 2016.
- CSÖRGŐ, T. et al. Simple solutions of relativistic hydrodynamics for systems with ellipsoidal symmetry. **Acta Physica Hungarica Series A, Heavy Ion Physics**, Springer, v. 21, n. 1, p. 73–84, 2004.
- CSÖRGŐ, T. et al. Simple solutions of relativistic hydrodynamics for longitudinally and cylindrically expanding systems. **Physics Letters B**, Elsevier, v. 565, p. 107–115, 2003.
- DANIELEWICZ, P.; ODYNYEC, G. Transverse momentum analysis of collective motion in relativistic nuclear collisions. **Physics Letters B**, Elsevier, v. 157, n. 2-3, p. 146–150, 1985.
- DANIELEWICZ, P. et al. Collective motion in nucleus-nucleus collisions at 800 mev/nucleon. **Physical Review C**, APS, v. 38, n. 1, p. 120, 1988.
- DINH, P. M.; BORGHINI, N.; OLLITRAULT, J.-Y. Effects of hbt correlations on flow measurements. **Physics Letters B**, Elsevier, v. 477, n. 1-3, p. 51–58, 2000.
- DRESCHER, H. et al. Parton based Gribov-Regge theory. **Phys.Rept.**, v. 350, p. 93–289, 2001.
- DRESCHER, H. et al. Initial condition for quark-gluon plasma evolution. **Physical Review C**, APS, v. 65, n. 5, p. 054902, 2002.
- DRESCHER, H. et al. Initial condition for QGP evolution from NEXUS. **Phys.Rev.**, C65, p. 054902, 2002.
- DUDEK, D. M. et al. Effects of equation of state on hydrodynamic expansion, spectra, flow harmonics and two-pion interferometry. 2014.
- FENG, A. Reaction Plane Dependent Away-side Modification and Near-side Ridge in Au+Au Collisions. **J.Phys.G**, G35, p. 104082, 2008.
- FU, J. Centrality dependence of mapping the hydrodynamic response to the initial geometry in heavy-ion collisions. **Phys. Rev.**, C92, n. 2, p. 024904, 2015.
- GALE, C.; JEON, S.; SCHENKE, B. Hydrodynamic Modeling of Heavy-Ion Collisions. **Int.J.Mod.Phys.**, A28, p. 1340011, 2013.
- GALE, C. et al. Event-by-event anisotropic flow in heavy-ion collisions from combined Yang-Mills and viscous fluid dynamics. **Phys.Rev.Lett.**, v. 110, p. 012302, 2013.

- GALE, C. et al. Initial state fluctuations and higher harmonic flow in heavy-ion collisions. **Nucl. Phys.**, A904-905, p. 409c–412c, 2013.
- GARDIM, F. G. et al. Mapping the hydrodynamic response to the initial geometry in heavy-ion collisions. **Phys.Rev.**, C85, p. 024908, 2012.
- GARDIM, F. G. et al. Effects of viscosity on the mapping of initial to final state in heavy ion collisions. **Phys. Rev.**, C91, n. 3, p. 034902, 2015.
- GINGOLD, R. A.; MONAGHAN, J. J. Smoothed particle hydrodynamics: theory and application to non-spherical stars. **Monthly notices of the royal astronomical society**, Oxford University Press Oxford, UK, v. 181, n. 3, p. 375–389, 1977.
- GYULASSY, M.; RISCHKE, D. H.; ZHANG, B. Hot spots and turbulent initial conditions of quark-gluon plasmas in nuclear collisions. **Nuclear Physics A**, Elsevier, v. 613, n. 4, p. 397–434, 1997.
- HAMA, Y. et al. Further results on peripheral-tube model for ridge correlation. **Acta Phys.Polon.Supp.**, v. 6, p. 513–518, 2013.
- HAMA, Y. et al. Trying to understand the ridge effect in hydrodynamic model. **Non-lin.Phenom.Complex Syst.**, v. 12, p. 466–470, 2009.
- HAMA, Y. et al. Fluctuating initial conditions in hydrodynamics for two-particle correlations. 2010.
- HAMA, Y. et al. Trying to understand the in-plane/out-of-plane effect in long-range correlations. **PoS**, WPCF2011, p. 048, 2011.
- HAMA, Y.; KODAMA, T.; JR., O. S. Topics on hydrodynamic model of nucleus-nucleus collisions. **Braz.J.Phys.**, v. 35, p. 24–51, 2005.
- HAMA, Y.; KODAMA, T.; SOCOLOWSKI JR., O. Topics on hydrodynamic model of nucleus-nucleus collisions. **Braz. J. Phys.**, v. 35, p. 24–51, 2005.
- HIRANO, T.; TSUDA, K. Collective flow and two pion correlations from a relativistic hydrodynamic model with early chemical freezeout. **Phys. Rev.**, C66, p. 054905, 2002.
- HOBSON, M. P.; EFSTATHIOU, G. P.; LASENBY, A. N. **General relativity: an introduction for physicists**. [S.l.]: Cambridge University Press, 2006.
- HUOVINEN, P. Hydrodynamical description of collective flow. Chapter 1. p. 600–633, 2003.
- HWA, R. C. Statistical description of hadron constituents as a basis for the fluid model of high-energy collisions. **Physical Review D**, APS, v. 10, n. 7, p. 2260, 1974.
- JIA, J. Measurement of the distributions of event-by-event flow harmonics in Pb-Pb Collisions at $\sqrt{s_{NN}} = 2.76$ TeV with the ATLAS detector. **Nucl. Phys.**, A904-905, p. 421c–424c, 2013. [Nucl. Phys.A904,421(2013)].
- JIA, J.; COLLABORATION, A. Measurement of event plane correlations in pb-pb collisions at $\sqrt{s_{NN}}=2.76$ tev with the atlas detector. **Nuclear Physics**, v. 910-911, p. 276–280, 2013.
- JR., O. S. et al. Fluctuations of the initial conditions and the continuous emission in hydro description of two-pion interferometry. **Phys.Rev.Lett.**, v. 93, p. 182301, 2004.
- KAKADE, U.; PATRA, B. K.; THAKUR, L. Bottomonium suppression: A probe to the pre-equilibrium era of quark matter. **arXiv preprint arXiv:1404.6152**, 2014.

KHALATNIKOV, I. Nekotorye voprosy relyativistskoi gidrodinamiki. **ZHURNAL EKSPERIMENTALNOI I TEORETICHESKOI FIZIKI, MEZHDUNARODNAYA KNIGA 39 DIMITROVA UL.**, 113095 MOSCOW, RUSSIA, v. 27, n. 5, p. 529–541, 1954.

KOCH, P.; MÜLLER, B.; RAFELSKI, J. Strangeness in relativistic heavy ion collisions. **Physics Reports**, Elsevier, v. 142, n. 4, p. 167–262, 1986.

KOLB, P. F.; HEINZ, U. W. Hydrodynamic description of ultrarelativistic heavy ion collisions. p. 634–714, 2003.

LIU, M.; LIU, G. Smoothed particle hydrodynamics (sph): an overview and recent developments. **Archives of computational methods in engineering**, Springer, v. 17, n. 1, p. 25–76, 2010.

LUCY, L. B. A numerical approach to the testing of the fission hypothesis. **The astronomical journal**, v. 82, p. 1013–1024, 1977.

MA, G. et al. Di-hadron azimuthal correlation and mach-like cone structure in parton/hadron transport model. **Phys.Lett.**, B641, p. 362–367, 2006.

MA, G.-L.; WANG, X.-N. Jets, Mach cone, hot spots, ridges, harmonic flow, dihadron and γ -hadron correlation in high-energy heavy-ion collisions. **Phys.Rev.Lett.**, v. 106, p. 162301, 2011.

MARTIN, B. R.; SHAW, G. **Particle physics**. [S.l.]: John Wiley & Sons, 2017.

MATSUI, T.; SATZ, H. J/ψ suppression by quark-gluon plasma formation. **Physics Letters B**, Elsevier, v. 178, n. 4, p. 416–422, 1986.

MCDONALD, S. et al. A detailed study and synthesis of flow observables in the ip-glasma+music+urqmd framework. **Nuclear Physics A**, v. 967, p. 393–396, 2017.

MCLERRAN, L. From AGS-SPS and Onwards to the LHC. **J. Phys.**, G35, p. 104001, 2008.

MOHAPATRA, S. Measurement of the distribution of event-by-event harmonic flow in Pb-Pb collisions at $\sqrt{s_{NN}} = 2.76$ TeV with the ATLAS detector. **J. Phys. Conf. Ser.**, v. 446, p. 012024, 2013.

Monaghan, J. Smoothed particle hydrodynamics. **Annu. Rev. Astron. and Astroph.**, v. 30, p. 543–574, 1992.

MOTA, P.; CHEN, W.; QIAN, W.-L. A derivation of the entropy-based relativistic smoothed particle hydrodynamics by variational principle. 2017.

NACHMAN, B.; MANGANO, M. L. Observables for possible qgp signatures in central pp collisions. **European Physical Journal C**, v. 78, n. 4, p. 343, 2018.

NIEMI, H. et al. Event-by-event distributions of azimuthal asymmetries in ultrarelativistic heavy-ion collisions. **Phys.Rev.**, C87, p. 054901, 2012.

NONAKA, C.; HONDA, E.; MUROYA, S. (3+ 1)-dimensional relativistic hydrodynamical expansion of hot and dense matter in ultra-relativistic nuclear collision. **The European Physical Journal C-Particles and Fields**, Springer, v. 17, n. 4, p. 663–673, 2000.

OLLITRAULT, J.-Y. Flow systematics from SIS to SPS energies. **Nucl. Phys.**, A638, p. 195–206, 1998.

PETERSEN, H. et al. Triangular flow in event-by-event ideal hydrodynamics in Au+Au collisions at $\sqrt{s_{NN}} = 200A$ GeV. **Phys. Rev.**, C82, p. 041901, 2010.

- POSKANZER, A. M.; VOLOSHIN, S. A. Methods for analyzing anisotropic flow in relativistic nuclear collisions. **Physical Review C**, APS, v. 58, n. 3, p. 1671, 1998.
- PRENDERGAST, E. et al. Flow and multifragmentation of $24mg + 27al$ at intermediate energies. **Physical Review C**, APS, v. 61, n. 2, p. 024611, 2000.
- PUTSCHKE, J. Near-side Delta eta correlations of high p(T) hadrons from STAR. **Nucl.Phys.**, A783, p. 507–510, 2007.
- QIAN, W.-L. et al. On the origin of trigger-angle dependence of di-hadron correlations. **Phys.Rev.**, C87, p. 014904, 2013.
- QIAN, W.-L. et al. Effect of chemical freeze out on identified particle spectra at 200-A-GeV Au-Au Collisions at RHIC using SPheRIO. **Int.J.Mod.Phys.**, E16, p. 1877–1882, 2007.
- QIAN, W.-L. et al. p(T) distribution of hyperons in 200-A-GeV Au-Au in smoothed particle hydrodynamics. **Braz.J.Phys.**, v. 37, p. 767–769, 2007.
- QIAN, W.-L. et al. Decomposition of fluctuating initial conditions and flow harmonics. **J.Phys.G**, G41, p. 015103, 2014.
- QIN, G.-Y. et al. Translation of collision geometry fluctuations into momentum anisotropies in relativistic heavy-ion collisions. **Phys. Rev.**, C82, p. 064903, 2010.
- RANIWALA, R.; RANIWALA, S.; VIYOGI, Y. P. Determination of azimuthal anisotropy of neutral pions from the measured anisotropy of photons in ultra-relativistic nuclear collisions. **Physics Letters B**, Elsevier, v. 489, n. 1-2, p. 9–14, 2000.
- SCHLAGHECK, H. Directed and elliptic flow in 158 GeV Pb + Pb collisions. **Nucl. Phys.**, A661, p. 337–340, 1999.
- SCHLEI, B.; STROTTMAN, D. Predictions for $s = 200$ a gev $u + u$ collisions from relativistic hydrodynamics. **Physical Review C**, APS, v. 59, n. 1, p. R9, 1999.
- SHARMA, M.; PRUNEAU, C. A. Methods for the Study of Transverse Momentum Differential Correlations. **Phys. Rev.**, C79, p. 024905, 2009.
- SINGH, G.; JAIN, P. Collective flow by the azimuthal correlation of projectile fragments in relativistic heavy-ion collisions. **Physical Review C**, APS, v. 49, n. 6, p. 3320, 1994.
- SINGH, S.; BANG, B. **The Origin of the Universe**. [S.l.]: Harper Perennial, 2005.
- SORENSEN, P. Higher Flow Harmonics in Heavy Ion Collisions from STAR. **J. Phys.**, G38, p. 124029, 2011.
- SORGE, H. Highly sensitive centrality dependence of elliptic flow: A novel signature of the phase transition in qcd. **Physical Review Letters**, APS, v. 82, n. 10, p. 2048, 1999.
- SOUZA, R. Derradi de; KOIDE, T.; KODAMA, T. Hydrodynamic Approaches in Relativistic Heavy Ion Reactions. **Prog. Part. Nucl. Phys.**, v. 86, p. 35–85, 2016.
- TAKAHASHI, J. et al. Topology studies of hydrodynamics using two particle correlation analysis. **Phys.Rev.Lett.**, v. 103, p. 242301, 2009.
- TEANEY, D.; YAN, L. Triangularity and Dipole Asymmetry in Heavy Ion Collisions. **Phys.Rev.**, C83, p. 064904, 2011.

- TEANEY, D.; YAN, L. Non linearities in the harmonic spectrum of heavy ion collisions with ideal and viscous hydrodynamics. **Phys.Rev.**, C86, p. 044908, 2012.
- TEANEY, D.; YAN, L. Event-plane correlations and hydrodynamic simulations of heavy ion collisions. **Phys. Rev.**, C90, n. 2, p. 024902, 2014.
- TRZUPEK, A. Measurement of elliptic flow and higher-order flow harmonics from the event plane and two particle correlation methods in $\sqrt{s_{NN}} = 2.76$ tev pb+pb collisions with the atlas detector at the lhc. **Journal of Physics G Nuclear and Particle Physics**, v. 38, n. 38, p. 124163, 2011.
- ULERY, J. G.; WANG, F. Cumulant versus jet-like three-particle correlations. **Phys. Rev.**, C79, p. 024904, 2009.
- VOLOSHIN, S.; ZHANG, Y. Flow study in relativistic nuclear collisions by Fourier expansion of Azimuthal particle distributions. **Z. Phys.**, C70, p. 665–672, 1996.
- VOLOSHIN, S. A. Toward the energy and the system size dependence of elliptic flow: working on flow fluctuations. **arXiv preprint nucl-th/0606022**, 2006.
- VOLOSHIN, S. A.; POSKANZER, A. M.; SNELLINGS, R. Collective phenomena in non-central nuclear collisions. In: **Relativistic Heavy Ion Physics**. [S.l.]: Springer, 2010. p. 293–333.
- WANG, S. et al. Measurement of collective flow in heavy ion collisions using particle pair correlations. **Phys. Rev.**, C44, p. 1091–1095, 1991.
- WANG, X.-N.; GYULASSY, M. Gluon shadowing and jet quenching in a+a collisions at $s = 200$ a gev. **Physical Review Letters**, APS, v. 68, n. 10, p. 1480, 1992.
- WEINBERG, S. The first three minutes. a modern view of the origin of the universe. 1977.
- WELKE, G. et al. Azimuthal distributions in heavy ion collisions and the nuclear equation of state. **Physical Review C**, APS, v. 38, n. 5, p. 2101, 1988.
- WEN, D. et al. On the peripheral-tube description of the two-particle correlations in nuclear collisions. **J. Phys.**, G46, n. 3, p. 035103, 2019.
- WERNER, K. et al. Evidence for Flow from Hydrodynamic Simulations of p -Pb Collisions at 5.02 TeV from ν_2 Mass Splitting. **Phys. Rev. Lett.**, v. 112, n. 23, p. 232301, 2014.
- WERNER, K.; KARPENKO, I.; PIEROG, T. The 'Ridge' in Proton-Proton Scattering at 7 TeV. **Phys.Rev.Lett.**, v. 106, p. 122004, 2011.
- WERNER, K.; LIU, F.-M.; PIEROG, T. Parton ladder splitting and the rapidity dependence of transverse momentum spectra in deuteron-gold collisions at RHIC. **Phys.Rev.**, C74, p. 044902, 2006.
- XU, J.; KO, C. M. Triangular flow in heavy ion collisions in a multiphase transport model. **Phys.Rev.**, C84, p. 014903, 2011.
- XU, Y. et al. Traces of nonequilibrium dynamics in relativistic heavy-ion collisions. **Phys. Rev.**, C96, n. 2, p. 024902, 2017.
- YAN, L.; OLLITRAULT, J.-Y. $\nu_4, \nu_5, \nu_6, \nu_7$: nonlinear hydrodynamic response versus LHC data. **Phys. Lett.**, B744, p. 82–87, 2015.
- YAN, L.; PAL, S.; OLLITRAULT, J.-Y. Nonlinear hydrodynamic response confronts LHC data. **Nucl. Phys.**, A956, p. 340–343, 2016.

APPENDIX A – BOXMULLER METHOD

Supposing two independent standard normal distributions $x \sim (0, 1)$ and $y \sim (0, 1)$, the joint probability density function is

$$\begin{aligned} p(x, y) = p(x) \cdot p(y) &= \frac{1}{\sqrt{2\pi}} e^{-\frac{x^2}{2}} \cdot \frac{1}{\sqrt{2\pi}} e^{-\frac{y^2}{2}} \\ &= \frac{1}{2\pi} e^{-\frac{x^2+y^2}{2}} \end{aligned} \quad (1)$$

Taking the polar coordinate transformation

$$x = R \cos \theta, \quad (2)$$

$$y = R \sin \theta, \quad (3)$$

then

$$\frac{1}{2\pi} e^{-\frac{x^2+y^2}{2}} = \frac{1}{2\pi} e^{-\frac{R^2}{2}}, \quad (4)$$

we can understand Eq.(4) as the product of the two probability distribution density functions

$$\theta \sim (0, 2\pi) = 2\pi U_2, U_2 = (0, 1), \quad (5)$$

and

$$P(R) = e^{-\frac{R^2}{2}}. \quad (6)$$

The corresponding cumulative distribution function (CDF) and the CDF's inverse function are as follows,

$$\begin{aligned} P(R \leq r) &= \int_0^r e^{-\frac{\rho^2}{2}} \rho d\rho = -e^{-\frac{\rho^2}{2}} \Big|_0^r = -e^{-\frac{r^2}{2}} + 1 \\ F^{-1}(u) &= \sqrt{-2 \log(1-u)} \end{aligned} \quad (7)$$

Since u is uniformly distributed, therefore $1-u$ is uniformly distributed.

Therefore, the Box-Muller method for generating random numbers conforming to Gaussian distribution can be realized as follows.

First, Generating two random numbers $U_1, U_2 \sim (0, 1)$. Then, we take advantage of them to create the radius $R = \sqrt{-2 \log U_1}$ and the angle $\theta = 2\pi U_2$. Last, Converting (R, θ) from polar to Cartesian coordinates $(R \cos \theta, R \sin \theta)$.

$$Z = R \cos \theta = \sqrt{-2 \log U_1} \cos(2\pi U_2). \quad (8)$$

The Z can generate a Gaussian distribution.

APPENDIX B – SIMPSON'S RULE

Simpson's rule is a numerical integration method that approaches the original function with a quadratic curve to obtain a numerical approximate solution of the definite integral. The integral of a function $f(x)$ between a and b is approximated as follows,

$$\int_a^b f(x)dx \approx \frac{b-a}{6} \left[f(a) + 4f\left(\frac{a+b}{2}\right) + f(b) \right]. \quad (1)$$

If the interval of integration $[x_1, x_3]$ is small, by using three points (x_1, y_1) , (x_2, y_2) , (x_3, y_3) , where $x_2 = \frac{x_1+x_3}{2}$, we obtained

$$\int_{x_1}^{x_3} f(x)dx \approx \frac{x_3 - x_1}{6} (y_1 + 4y_2 + y_3), \quad (2)$$

it will be adequate approximate to the exact integral.

For a large interval of integration $[L, R]$, we divide interval $[L, R]$ into n subintervals, then

$$2\frac{R-L}{n} = x_2 - x_0 = (x_4 - x_2) = (x_n - x_{n-2}), \quad (3)$$

where $x_0 = L$, $x_n = R$. Then Simpson's rules are applied to each subinterval, and the results are added to obtain an integral approximation for the entire interval.

$$\begin{aligned} \int_L^R f(x)dx &= \int_{x_0}^{x_n} f(x)dx = \int_{x_0}^{x_2} f(x)dx + \int_{x_2}^{x_4} f(x)dx + \cdots + \int_{x_{n-2}}^{x_n} f(x)dx \\ &\approx \frac{x_2 - x_0}{6} (y_0 + 4y_1 + y_2) + \frac{x_4 - x_2}{6} (y_2 + 4y_3 + y_4) + \frac{x_6 - x_4}{6} (y_4 + 4y_5 + y_6) + \cdots \\ &= \frac{R-L}{3n} [y_0 + y_n + 2(y_2 + y_4 + \cdots + y_{n-2}) + 4(y_1 + y_3 + \cdots + y_{n-1})] \end{aligned} \quad (4)$$

APPENDIX C – THE PHENIX DATA

Table 8 – The PHENIX data (AFANASIEV et al., 2009), $v_2\{2\}$ as a function of p_T in centrality 20%–60%.

p_t	0.251	0.349	0.448	0.548	0.648	0.748	0.848	0.948
v_2	0.00778	0.03793	0.05476	0.06374	0.07303	0.08283	0.09301	0.10247
p_t	1.091	1.290	1.489	1.689	1.890	2.198	2.700	3.348
v_2	0.11444	0.13201	0.14884	0.16226	0.17456	0.19027	0.20415	0.21363

LIST OF PUBLICATION AND MANUSCRIPT

1. Dan Wen, Wagner Maciel Castilho, Kai Lin, Wei-Liang Qian, Yojiro Hama, Takeshi Kodama,
On the peripheral tube description of the two-particle correlations in nuclear collisions,
Journal of Physics G: Nuclear and Particle Physics 46 (2019) 035103
2. Dan Wen, Kai Lin, Wei-Liang Qian,
Quasinormal Modes of the Planar Black Holes of a Particular Lovelock Theory,
Communications In Theoretical Physics 70 (2018) 689-694
3. Dan Wen, Kai Lin, Wei-Liang Qian, Bin Wang, Yojiro Hama, Takeshi Kodama,
On nonlinearity in hydrodynamic response to the initial geometry in relativistic heavy-ion collisions,
Manuscript in preparation
4. Hong-Hao Ma, Dan Wen, Kai Lin, Wei-Liang Qian, Bin Wang, Yojiro Hama, Takeshi Kodama,
Hydrodynamic results on multiplicity fluctuations in heavy-ion collisions,
Manuscript in preparation